Experimental Strategies for Frost Analysis

A THESIS
SUBMITTED TO THE FACULTY OF THE GRADUATE SCHOOL
OF THE UNIVERSITY OF MINNESOTA
BY

Daniel D. Janssen

IN PARTIAL FUFILLMENT OF THE REQUIREMENTS
FOR THE DEGREE OF
MASTER OF SCIENCE

Francis A. Kulacki
Department of Mechanical Engineering
University of Minnesota

September 2013

Acknowledgements

The author thanks all those without whom this thesis could not have taken shape. Professor Francis Kulacki, through his support and guidance, has both motivated and inspired me to seek out new ideas through which physical concepts can be analyzed and to apply those ideas via research. His feedback has been invaluable in the writing of this thesis and has given me the opportunity to improve my work.

I owe the subject matter and field of study to Bill Mohs, whose work set the stage for my own. The effort of Bill has made the entire project a reality, which I had the good fortune to be a part of before its conclusion. His knowledge and expertise of the field helped me to develop ideas more thoroughly and correctly. As a friend and co-worker, I could not have asked for a better person.

The re-assurance and support of Kimberly Sleider gave me strength to make it through when the task seemed insurmountable. Her creative suggestions and helpful conversation gave me a chance to see things from another point of view, which has been of great benefit to both my thinking and writing.

My mother and father have provided me support every step of the way, and have given me the inspiration to make the most of life. Their love and encouragement have allowed me to accomplish this thesis and motivated me to continue my work. I would never have reached this point without their help.

It would have been impossible to complete the project without the funding granted by Thermo King and Ingersoll Rand Corporation. Their assistance to both Bill and me allowed us to acquire the equipment of high accuracy needed to experiment with new measurement methods and set the basis for our research.

To my parents.

To Kimberly and the Sleider family.

To the future.

Abstract

An area of increasing importance in the field of refrigeration is the study of frosting and defrosting. Frosting poses a concern to many refrigeration systems, as frost growth both obstructs airflow through low temperature heat exchangers and increases heat transfer resistance. Drastic decreases in system efficiency result from the compounding of these problems, and because it is difficult to prevent the frosting process, refrigeration systems must be defrosted periodically to restore optimal operating conditions. A deeper understanding of the complex physical processes of frosting and defrosting will lead to more efficient refrigeration system designs; an idea which has driven a rise in frost growth research over recent decades.

Although research has shown great progress, there remain significant challenges associated with predicting the frosting and defrosting processes accurately under wide ranges of conditions. The equations governing such behavior still remain insoluble by exact analytical methods. Numerical approaches have shown the most promising results, but are yet in an early stage of development.

Most research has instead been concerned with developing correlations for frost properties and growth, though few are applicable to varying conditions. The most commonly used correlations are shown to have widely different results, perhaps owing to different experimental methods used to acquire data and a lack of deeper level analysis. A new thickness correlation is proposed which attempts to reconcile to some degree the gap between theory and application. Broader ranges of data are used for fitment which enables the application of the correlation to a wider range of conditions.

To improve the consistency of results in frost research, it is suggested that new forms of data acquisition be explored. Proposed alternative methods utilize high magnification imaging equipment in combination with computer based measurements, which are shown to be capable of improving accuracy by an order of magnitude in some areas (specifically frost thickness measurement) when calibrated appropriately. In addition to improving measurement accuracy such methods make possible the rapid calculation of droplet geometry during defrosting, an area which has seen little research until recently.

The influence of the experimental apparatus on results is also investigated, and a variety of different setups used in past and recent research are categorized according to capability and functionality. Pros and cons of related parameters are discussed with an emphasis on goals.

Opportunities for future work include the further development of computer based measurement methods, the acquisition of data over wider ranges of conditions and improvements on the experimental apparatus required to achieve those conditions reliably.

It is clear from this research that frost growth is a developing field where much progress is yet to be made. Experimental setups of types ranging from small enclosed tests to wind tunnels on industrial evaporators have provided a clearer understanding of the phenomenon in many aspects. Research presented in this thesis shows that small scale experiments are preferable at this point in time to reach deeper understanding of the frost growth process. It is shown here that many current methods of measurement for important frost growth parameters can be greatly improved upon by the use of computer based algorithms. Faster and more accurate measurement opportunities mean that larger data sets spread across wider ranges of testing conditions can be obtained, setting the stage for more advanced correlation development. Currently, most correlations are only applicable to specific conditions and are still not highly accurate. An attempt is made to show that larger collections of reliable data can be used to develop more robust correlations. To do so a new correlation is proposed which fits a wide range of conditions well. Finally it is shown that the defrosting process may be understood more fully by the use of digital analysis of visual data during defrosting.

Contents

List of Tables vii
List of Figures viii
Nomenclature x

1 Introduction 1

2 Literature Review 3
2.1 Modern Research 3
2.2 Traditional experimental measurement techniques 9
2.2.1 Experimental Design 11
2.2.2 Test Surface Design 14
2.2.3 Cooling Method 16
2.2.4 Heat Flux 17
2.2.5 Air-frost interface/frost interface temperature 18
2.2.6 Ambient conditions 19
2.2.7 Frost mass 20
2.2.8 Frost thickness 22
2.2.9 Image acquisition and structure analysis 24
2.2.10 Tabulated Comparison 27
2.3 Classification of correlations from literature 28
2.3.1 Frost thickness 28
2.3.2 Frost thermal conductivity 31

3 Experimental Setup 36
3.1 General details 36
3.2 Experimental setup 36
3.2.1 Test chamber 38
3.2.2 Test surface and assembly 38
3.2.3 Testing conditions 40
3.2.4 Image and data acquisition 40
3.3 Experimental strategies 41
3.3.1 Experimental process 41
3.3.2 Measurement of interior data 42
3.3.3 Measurement of frost properties 46
3.4 Comparison of experimental methods 60
3.5 Error of measured quantities 62
3.5.1 Uncertainty associated with primary parameters 62

4 Comparative models for frosting and defrosting Analytical Solutions 79
4.1 Background 79
4.2 Test surface model for heating and cooling 79
4.3 One-dimensional transient models: Exact solutions 80
4.3.1 Exact solution: One dimensional conduction 81
4.4 One-dimensional transient models: Lumped 84
4.4.1 Constant applied heat flux case 85
4.4.2 Time varying heat flux 86
4.4.3 Summary of lumped capacitance approach 87
4.5 Comparison of analytical models 88
4.6 Validation of one dimensional inhomogeneous model 88
4.7 Validation of lumped capacitance model 92

4.8 Experimental validation of heat transfer models. 93
4.8.1 Results of heating and cooling tests 94

5 Frost growth modeling 98
5.1 Frost thickness 98
5.1.1 Comparison to correlations 98
5.1.2 New correlation development 102
5.2 Porosity Measurement 112
5.3 Droplet size analysis 115
5.4 Analysis of image acquisition methods 116

6 Conclusion 117
6.1 Concluding Remarks 117
6.2 Summary of Results 118
6.3 Future work 119

7 References 120

Appendix A ..... Error! Bookmark not defined.
A.1 Derivation of Eq. (3.49) 122
A.2 Derivation of Eqs. (4.3) to (4.5) 123
A.3 Derivation of Eqs. (4.7) to (4.9) 127
A.4 Derivation of Eq. (4.16) 128
A.5 Derivation of Eqs. (4.18) and (4.19) 130
A.6 Derivation of Eq. (4.21) 132

Appendix B 135

Appendix C 138
C.1 Thickness Measurement 138
C.2 Frost Porosity 140
C.3 Droplet Geometry (Single) 141
C.4 Droplet Geometry (Looped) 143

Appendix D ..... Error! Bookmark not defined.
D.1 Thermal conductivity correlation for air 145
D.2 Heat flux losses from chamber 146
D.3 Root mean square deviation 146

3 List of Tables

Table **Page**

1. Experimental setups used in recent frost research. 25
2. Comparison of test surfaces used for frost growth in recent experimentation. 25
3. Outline of experimental conditions used to obtain results in recent frost research. 26
4. Modern experimental techniques used in frost related research, part 1. 26
5. Modern experimental techniques used in frost related research, part 2. 27
6. Applicable frost thickness correlations and their development conditions. 29
7. External conditions for empirical thermal conductivity correlations. 31
8. Comparison of experimental setup to those of similar studies. 61
9. Measurement error of experimental quantities. 62
10. Summary of uncertainty of experimental parameters 78
11. One dimensional simulation system properties. 89
12. Experimental results relating to frost thickness 101
13. Coefficients for 8th degree polynomials representing A and B. 108

4 List of Figures

Figure **Page**

1. Surface wetting with interior contact angle 4
2. Frost growth occurring from 0 to -5 °C 6
3. Frost growth occurring from -10 to -20 °C 6
4. Heat transfer coefficients affected by fin pitch 8
5. Removable fin technique to measure frost mass 21
6. Illustration of the image acquisition method of frost thickness measurement. 23
7. Comparison of correlations for prediction of frost thickness. 30
8. Comparison of frost thermal conductivity correlations. 33
9. Variation of thermal conductivity in the parallel and perpendicular directions 34
10. Schematic of experimental apparatus 37
11. Schematic of the test surface assembly 39
12. Free convection coefficient determined by air and wall temperatures. 46
13. Frost thickness measurement locations. 49
14. Illustration of frost profile data generated by MATLAB® 50
15. Frost thickness profile after conversion to physical units. 50
16. Algorithm for determining frost thicknesses 51
17. Result of base image subtraction from droplet matrix. 53
18. Closing boundaries after black and white conversion. 54
19. Algorithm for determining droplet properties. 55
20. Front image of frost surface used for finding porosity. 64
21. Variation of N_V with the conversion value. 65
22. Absolute thickness measurement error based on calibration uncertainty. 68
23. Average thickness measurement error for different scaling and calibration 68
24. Effect on perimeter error as the size of variance and number 71
25. Effect of changing perimeter uncertainty on the error in area for 72
26. Error in estimation of the heat transfer coefficient for free convection 74
27. Error in thermal conductivity based on porosity error 76
28. Specific heat error resulting from uncertainty of porosity 78
29. Modification of geometry for modeling purposes 80
30. Problem splitting technique 81
31. Control volume for the lumped solution. 82
32. Comparison of homogeneous and inhomogeneous solutions 90
33. Comparison of homogeneous and inhomogeneous solutions 90
34. Changes in system response relative to homogeneous conditions 91
35. Changes in system response relative to homogeneous conditions 91
36. Comparison of exact and lumped solutions 93
37. Heat flux model prior to subtraction of the losses 95
38. Comparison of experimental and analytical temperature curves 95
39. Heat flux model prior to subtraction of the losses 96
40. Comparison of experimental and analytical temperature curves 96
41. Comparison of thickness measurements to correlation, Run 1. 99
42. Comparison of thickness measurements to correlation, Run 2. 99
43. Comparison of thickness measurements to correlation, Run 3. 100
44. Comparison of thickness measurements to correlation, Run 4. 100
45. Variation of K parameter with experimental data. 103
46. Comparison of correlation to experimental data. 104
47. Comparison of proposed correlation to data 105

48. Heat transfer coefficient (including latent effects) 106
49. Comparison of exponential correlation to experimental data. 109
50. Exponential correlation plotted over experimental data 109
51. Exponential correlation plotted over experimental data 110
52. Exponential correlation plotted over experimental data 111
53. Data fits for full set. Lines are 1:1. 111
54. Calculated porosity for three testing conditions 112
55. Trend of porosity changes over time. 113
56. Frost density over time estimated by porosity 114
57. Area fraction of test surface covered by water during defrosting 115
58. Average droplet perimeter during defrosting 116
59. Data fit for thermal conductivity of air. 145
60. Heat flux losses through wall 146

5 Nomenclature

A	area [m^2]
Bi	Biot number, $hV\ k^{-1}A^{-1}$
C_v	constant volume specific heat [$J \cdot kg^{-1}\ K^{-1}$]
C_p	constant pressure specific heat [$J \cdot kg^{-1}\ K^{-1}$]
COP	coefficient of performance
D	diffusion coefficient [$m^2 \cdot s^{-1}$] or diameter [m]
D^*	dimensionless diffusion coefficient, $D_{Ta} \cdot D_{Ttr}^{-1}$
D_h	hydraulic diameter, $4A \cdot P^{-1}$, [m]
Fo	Fourier number for mass diffusion, $D\ t \cdot D_h^{-2}$
F_t	dimensionless temperature factor, $1 + 0.052(T - T_{tr})(T_{tr} - T_w)^{-1}$
Gr_L	Grashof number, $g\beta\ \Delta T\ L^3 \cdot \upsilon^{-1}$
H	combined heat transfer coefficient, $h \cdot k^{-1}$
h	heat transfer coefficient [$W \cdot m^{-2} K^{-1}$]
$\bar{h}$	average heat transfer coefficient [$W \cdot m^{-2} K^{-1}$]
K	frost growth factor
k	thermal conductivity [$W \cdot m^{-1} K^{-1}$]
L	testing assembly thickness [m]
N	number of pixels by count
Nu	Nusselt number, $h\ D_h \cdot k^{-1}$
$\overline{Nu}$	average Nusselt number, $h\ D_h \cdot k^{-1}$
p	perimeter [m]
P	pressure [Pa]
Pr	Prandtl number, $\upsilon \cdot \alpha^{-1}$
q″	heat flux [$W \cdot m^{-2}$]
q	heat flow [W]
q_r	relative heat flow, $q''A_1 \cdot (hA_{2)}^{-1}$
r	radius [m]
R	gas constant [$J\ kg^{-1}\ K^{-1}$]
R_c''	thermal contact resistance [$W\ K^{-1}$]
Re_D	Reynolds number based on diameter, $\nu D \cdot \nu^{-1}$
RH	relative humidity [%]
RMSD	root mean square deviation
Sc	Schmidt number, $\nu \cdot D^{-1}$
T	temperature [°C]
T^*	dimensionless temperature ratio, $(T_{tr} - T_w)(T_a - T_w)^{-1}$
t	time [s]
TEM	thermoelectric module
V	volume [m^3]
v	velocity [$m \cdot s^{-1}$]
w	specific humidity ratio [$kg_{H2O} \cdot kg_{Air}^{-1}$]
x	position [m, px]

X^*	dimensionless position, $x \cdot (D_h\, Re_D\, Sc)^{-1}$
y	position [m, px]

Greek:

α	thermal diffusivity [$m^2 \cdot s^{-1}$]
β	coefficient of thermal expansion [$°C^{-1}$]
Γ	camera resolution conversion (scaling) ratio [$px \cdot mm^{-1}$]
γ	angle [deg/rad]
δ	frost thickness [mm]
ε	porosity with respect to air, $V_a \cdot V_i^{-1}$
θ	dimensionless temperature ratio, $(T_a - T_{dp})\ (T_a - T_w)^{-1}$
κ	pixel value distribution gradient [px^{-1}]
λ	Eigenvalue
μ	dynamic viscosity [Pa·s]
ν	kinematic viscosity, $\mu \cdot \rho^{-1}$, [$m^2 \cdot s^{-1}$]
Π	dimensionless pressure ratio, $(P_a - P_g)\ (P_a - P_{gfs})^{-1}$
ρ	density [$kg \cdot m^{-3}$]
σ	image conversion value
ϕ	relative humidity, $P_v \cdot P_g^{-1}$
ψ	dimensionless temperature ratio, $T - T_o$
ω	specific humidity ratio [$kg_{H2O} \cdot kg_{Air}^{-1}$]

Subscripts:

a	air property
air	air property
c	TEM (cold surface) property
f	frost property
fs	frost surface property
g	saturated property
h	indicates homogeneous solution
i	ice property
ice	ice property
∞	chamber air property
inf	chamber air property
M	maximum expected value
ma	mass averaged property
max	maximum value
mm	indicates measurement in units of [mm]
n	eigenvalue index
par	parallel direction
perp	perpendicular direction
px	indicates measurement in units of [px]

o	initial condition
s	test surface property
sp	spreader property
ss	indicates steady state solution
T	indicates a total quantity
tr	triple point property
v	vapor property
va	volume averaged property
voids	indicating voids in frost layer
w	TEM (cold surface) property

Superscripts:

*	dimensionless value
″	indicates flux value
a	actual value
p	predicted value

1 Introduction

The days of the first man made refrigeration systems are long past. Our capabilities have since improved drastically as a consequence of theoretical development and research, driven both by requirement and the insatiable human need of scientific progress. Fundamental to the improvement of these capabilities has been the verification of theory by the results of thorough experimentation. Not only does such experimentation provide the means to validate our ideas, but it also serves as an environment in which new observations may be made either by mistake or intentionally that can provide valuable insight about our world.

As theory becomes increasingly complex, so must methods of verification. Most generally, the development of improved theories is associated with the inclusion of additional information. It follows that experimentation must also evolve lest we begin to lose track of the variables at hand. Moreover, modern theory demands increasingly accurate measurements which can only be achieved by the use of more precise methods and equipment. In all cases, the choice of instrumentation and technique will govern both the validity of the results and influence any conclusions drawn about the theory. It is no surprise that the development of experimental methods is as vital to progress as the theories they are designed to test. Accordingly, it is necessary to keep a close watch over experimentation, especially in more recent areas of research where unwanted influences may creep up on results without being noticed due to an incomplete comprehension of the situation.

Refrigeration theory is a broad subject, and encompasses a variety of areas that are yet developing as well as many that are not. Amongst the developing areas, some are experiencing progress where careful experimentation will be necessary to validate new theories. The analysis and experimental methods presented herein will be applied to such an area to provide a basis for research and theoretical advancement.

An important and little understood phenomenon that occurs in refrigeration systems running in air environments below the freezing point of water is frost growth. The natural formation of frost on evaporator surfaces has plagued operators of such systems because of its detrimental effects on performance and efficiency. Frost layers increase airflow resistance by closing gaps between fins and ruin heat transfer characteristics by insulating surfaces. In the worst of cases, i.e.; high relative humidity and low coil[1] temperature, airflow may be blocked completely in relatively short periods of time. To resolve these issues, such refrigeration systems

[1] Coil is a term frequently used to describe heat typical heat exchangers in the refrigeration industry.

must undergo frequent defrost cycles, which further reduce efficiency by transporting heat into the refrigerated space and by requiring downtime of the entire refrigeration cycle. There exists a need for a deeper understanding of the phenomenon and theory to predict its behavior so that more efficient systems might be designed to reduce or eliminate concerns with frosting. However, the field has remained somewhat undeveloped for a long time because of the complexities associated with modeling. Recent theory suggests that frost growth may be theoretically explainable and predictable on a macroscopic level consistent with the improvement of refrigeration systems, even though it remains somewhat mysterious in nature at a smaller scale.

Established models of frosting include analytical predictions and empirical equations both of which aim to predict frost growth based on measureable ambient quantities and refrigeration system parameters. While they have been mildly successful in very specific situations, no model so far has shown a comprehensive understanding of the phenomenon and a capability to predict it accurately over a wide range of conditions. Knowledge and prediction of defrosting is even sparser, and very little research has been completed specific to the defrosting process. If the problems associated with frosting and defrosting are to be eliminated, theoretical development and experimental verification will be needed in both areas.

The objective here is to encourage progress by presenting and critically analyzing methods of experimentation used for frost research. In particular, the focus is on the validation of a testing facility and methods designed to provide data for the evaluation of a new defrosting model. Defrosting must begin with frosting, and the experimental operations must therefore be valid for both frost growth and removal so that initial defrost conditions can be accurately implemented. To aid in accomplishing these tasks, various experimental results will be compared with those predicted by numerical simulation and published theory. Doing so will allow for the validation of any assumptions made about the models or apparatus, and help to eliminate possible hidden sources of error.

Thus the investigation presented in this thesis encompasses both frosting and defrosting experimental methods, with the final goal of evaluating their performance and validity and thus the reliability of data acquired by their means.

2 Literature Review

2.1 Modern Research

Frost growth has been a topic of expanded scientific and engineering interest over the last few decades. Predictive equations which were once developed from observation and correlation have since evolved to comprehensive models based on theory and experimentation. Even so, there remains an apparent rift between the collective understanding of frost behavior and the predictive theory developed to date. The problem is evident both in the realm of experimentation where results frequently disagree, and in the wide variety of current models that are accurate only within narrow ranges of the governing parameters. Most likely that condition is the result of analysis that is not complex enough to reflect the subtleties of frost growth on a microscopic level rather than a total misunderstanding of the phenomenon. While theories about this behavior exist, they are mostly qualitative in nature, and the majority of frost growth models instead attempt to represent the overall effects on a macroscopic scale owing to the difficulties of modeling and the engineering tendency towards applicable progress as opposed to perfect understanding.

Nevertheless recent research indicates progress toward more comprehensive, robust and accurate models. This section presents a review of such research to bring the reader up to date and give the background information of this report.

In 2004, Irragory et al. [16] presented a review of past literature that included classifications of frost growth and property models and their categories of applicability. Hence, the reader is referred to their paper for background information prior to 2004, and only relevant sources will be included here along with post 2004 research.

Some recent research has focused on the effects of surface modification on frost growth. In particular, Liang et al. [24] have studied the influence of surface energy on the phase change of water vapor droplets and the frost growth on a flat surface. In their analysis, a statistical Gibbs free energy approach is used to evaluate the energy change of condensing water based on contact angle, which is the angle between the interior surface of the droplet and the wetting plane. The model evolved from the theory that condensation occurs in two processes: an initial nuclear appearance followed by nucleic growth. Their results show that at a fixed vapor pressure

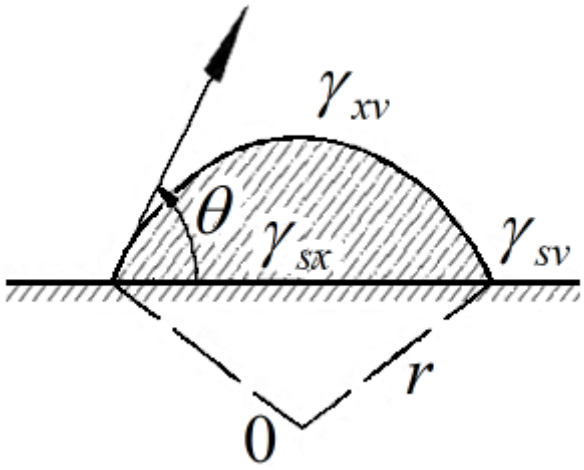

Figure 1. Surface wetting with interior contact angle [24].

and temperature, the contact angle is the only observable influence on the change in Gibbs free energy and thus the rate of freezing.

On surfaces with larger contact angles, known as hydrophobic surfaces, water droplets appeared more slowly and with greater diameter than those on a regular copper surface. They theorize that the reason for the change in condensation is the drastic reduction in nuclear growth speed that is predicted with increased contact angle. The drop in growth speed reduces the probability that a particular droplet will freeze and also hinders the propagation of phase change throughout a droplet. The net result of is the reduction of frost growth with larger contact angles. The hydrophobic surface in their experiments was copper with a thin wax coating, and results are compared to those of an uncoated copper surface. For a given time period, the density and height of the frost layer on the wax coated surface are lower than on the uncoated surface.

In many areas, the most important reason for determining the nature of frost growth is to improve modeling of heat exchanger performance under frosting conditions. Knowledge of thermal behavior is valuable to the engineer wishing to optimize performance in situations where frosting is not preventable, and to those hoping to maximize the efficiency of defrosting cycles. To that end, it is logical to spend time researching the heat transfer characteristics associated with frost growth even if the frost model itself remains undeveloped. One such study is that of Ngonda and Sheer [29], wherein a pressure drop and heat transfer model for cold room cooling coils is presented. The research focuses specifically on the effects of layer averaged properties of frost developing from supersaturated airflow over an evaporator coil. Supersaturated flow had seen limited research previously. Numerical simulation is used to solve the model and compare it to experimental results. Their model employs two subsystems: one for the calculation of frost related parameters, and the other for the coupled heat and mass transfer.

To improve accuracy the model is applied to small control volumes consisting of only one fin and section of tube, and the results are based on the sum of the sections across the entire evaporator. The heat transfer model is solved independently, and its outputs are used to determine requirements for updating the frost conditions. The frost model comprises the diffusion equation combined with a mass transfer coefficient and the deposition equation. Results of the simulation agree to within 18% of experimental values for coil duty and 24% for pressure drop at high temperature of airflow (0 °C). However, at lower temperatures (-12 °C and below), accuracy improves to a maximum error of 15%. The improvement is attributed to the frost model, which does not account for either re-melting of ice particles at higher temperature or the transition of water through a liquid phase into freezing (as opposed to sublimation, which occurs at and below -12°C). Results show that there is room for improvement in the frost modeling.

There has also been an abundance of recent research on the verification of predictive frost models for real refrigeration systems. Guilpart and Youbi-Idrissi [38] presented a paper on frost formation and growth thickness. Their model is made up of the fairly well established energy and mass balances for a frost layer, where empirical coupling equations are used to relate parameters. The primary focus of the research is on the effect of frost growth on the refrigeration system itself. To model the relationship, the characteristic fan curves are combined with equations for pressure drop and friction factor so that estimates of the system coefficient of performance (COP) can be made. The fans and compressors are tested and their efficiencies are included in the computations. The system was tested in a small temperature controlled storage room for varying levels of relative humidity and temperature. The predictive models agree reasonably well with the results. In particular, an observed drop in evaporating temperature over time implies a decrease in the COP. They have planned to continue future work in testing desiccant systems to reduce the frosting issue.

Many experiments involving frosting and defrosting depend on accurate knowledge of thermodynamic frost properties over the range of testing. These are almost always the frost density, thermal conductivity and specific heat, which are the primary properties used for heat transfer modeling. The accuracy of any model will ultimately depend on the use of these properties, it is therefore essential that they be predicted as reliably as possible. Yamashita et al. [36] performed experiments to evaluate these properties under low temperature conditions and compared their results to current predictive models. Prior to their study, most experiments with the goal of determining properties had been executed at air temperatures above 0 °C. Frost properties are thus measured at air temperatures ranging from 0 to -20 °C, which is illustrative

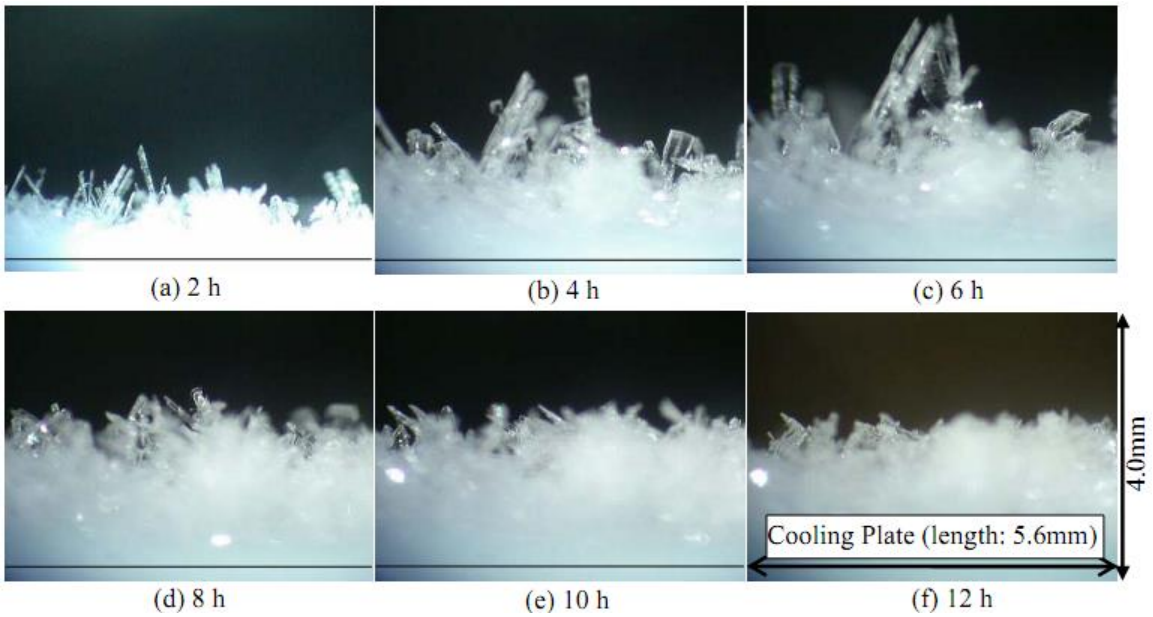

Figure 2. Frost growth occurring from 0 to -5 °C [36].

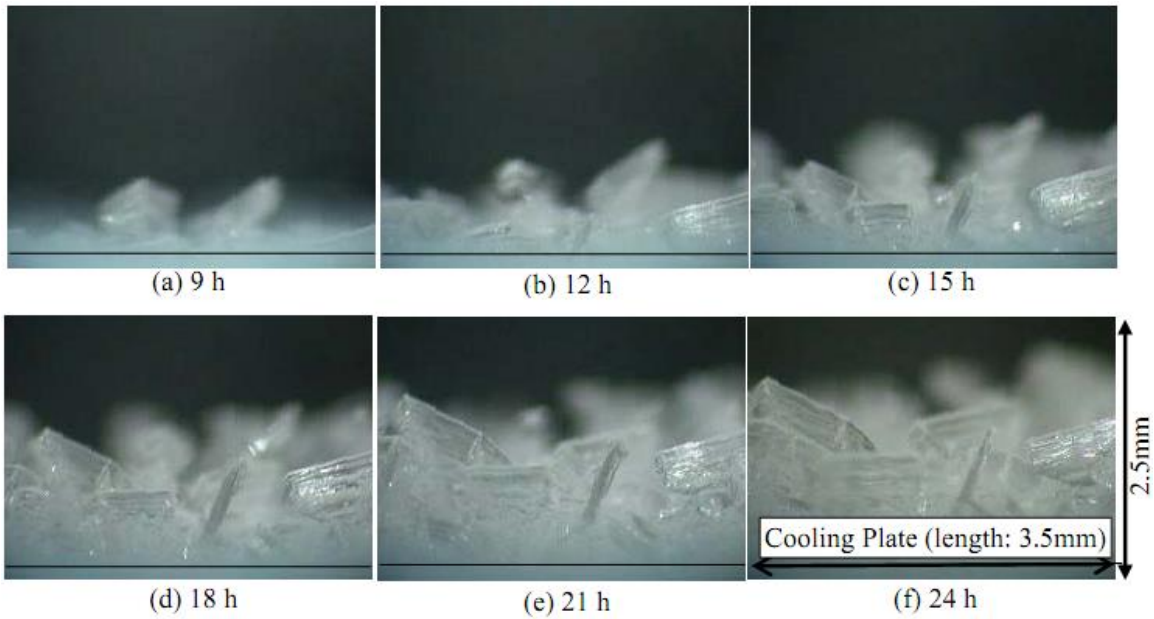

Figure 3. Frost growth occurring from -10 to -20 °C [36].

of common refrigeration operating conditions wherein frost might be expected to form. In addition to measuring the aforementioned properties, the heat and mass transfer coefficients are calculated.

Their experiment is performed in a controlled forced convection environment where the test surface can be photographed from the side with a stereoscopic microscope and camera to a resolution of 0.3 mm. Frost thickness is determined via photographic observation and its mass by

periodic weighing. Thermoelectric modules are used to regulate the test surface temperature while the properties are documented for frost heights up to 5 mm.

Two primary stages are observed: frost growth occurring from 0 to -5 °C and from -10 to -20 °C. The results show a marked difference in frost growth between these conditions (Figures 2 and 3, previous). In the higher temperature range, the ice crystals form needle like structures that eventually become the frame for a more dense frost buildup as time progresses. In the colder temperature range, the crystals tend to form block shaped structures that retain their formation even as the time becomes long. It is proposed that such a difference occurs because the total humidity ratios are lower for the low temperature condition than for the higher temperature condition (for an equal relative humidity). The results are of importance because they indicate that the properties, which depend on the frost structure, must vary with temperature in a complex manner [36].

The frost properties associated with the crystal structures are compared with the properties predicted by correlations from previous studies. As indicated by the photographs, the frost thickness increases rapidly for the high temperature range for the first several hours, before leveling off as bulk growth continues. Mass transfer and density show a linear increase. The surface temperature appears to be relatively constant, and little variation in thermal conductivity is observed. For the lower temperature conditions, the mass transfer and density changes are nonlinear, following the exponential trend exhibited by the thickness growth appearing in both cases. The surface temperature is again relatively constant and little change in thermal conductivity occurs.

In all cases, the properties appear to fall close to those predicted by correlations, but do not show signs of following the predicted trends. The Yonko-Sepsy [37] correlation appears to be more indicative of the actual thermal conductivity than the Brian [2] correlation. The Chilton-Colburn relation is applied to analyze the heat and mass transfer relationships. The analogy predicts that the ratio of the mass transfer coefficient to the heat transfer coefficient should approach the value of the specific heat if the Lewis number is assumed to be unity [36]. The results show variations from 0.31 to 0.68 in the mass to heat transfer ratio for the high temperature case, and 0.71 to 1.64 for the low temperature case. The results are not compared with the values of specific heat, as it was not measured in their experiment. However, they appear to be consistent with the specific heat of high porosity frost.

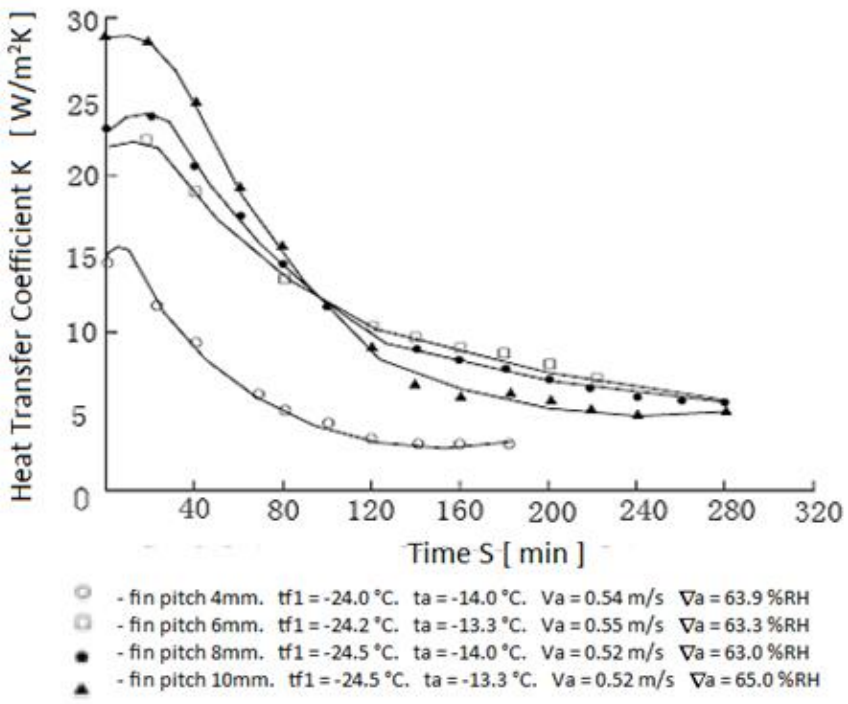

Figure 4. Heat transfer coefficients affected by fin pitch [4].

It is evident from these results that the prediction of frost properties can be difficult given the complex nature of ice crystal growth. Under some conditions, the structure appears to be significantly different, formed by blocks instead of needles, which has a notable impact on overall thermophysical properties. It is clear that more exact correlations will need to be developed to cover wider ranges of conditions.

Thermodynamic conditions are certainly not the only factor affecting frost growth. Water molecules must be deposited from the free air stream, and therefore the geometry of the cooling surface itself is also of significance. Ruiqui et al. [4] examine the effects of fin pitch on frost formation under low temperature conditions. Their study includes evaporator coils of four different fin pitches of 4, 6, 8 and 10 mm. A cryogenic wind tunnel is used to supply air below -10 °C at controlled humidity and wind speed across the coils for 100 min. The pitch of the fins is shown to affect both the amount and rate of frost buildup in the coil.

Initially, the rate of frosting is large for all cases because of the low density dendritic growth. As the layers begin to thicken, the frost surface temperature increases somewhat, which reduces further mass transfer and the growth slows. For the largest fin pitch (10 mm), the growth continues at a relatively high rate, which is most likely the result of a higher airflow resistance. In general frost thickness increases more slowly at lower fin pitches and less overall frost is deposited than at higher pitches.

As initial dendritic frost growth occurs, the heat transfer coefficient increases for all cases owing to the increased heat transfer surface area and induced turbulence, an effect also observed by Kondepudi [18]. However the effect is minor and the heat transfer coefficients drop sharply thereafter, most notably on the coil (heat exchanger) of 10 mm fin pitch. The larger fin pitch encourages frost growth, which explains the increased rate of decay in the heat transfer coefficient. The other coils show more gradual reductions and those with intermediate fin pitch (6 and 8 mm) eventually show the highest coefficients as that of the larger pitched coil drops more quickly. The smallest fin pitch exhibits the lowest heat transfer coefficient for the entirety of the experiment.

Figure 4 (previous page) shows the relative behaviors of the different coils. The effects of relative humidity on the heat transfer coefficients are also observed. The trend is quite similar to that of the coefficients' dependence on fin pitch. The coil with a pitch of 8 mm is tested under varying conditions of relative humidity. The results show that the heat transfer coefficient initially increases with relative humidity because of the increase in mass transfer rate. As mass transfer continues, the heat transfer coefficient under the condition of high relative humidity quickly drops below that at lower humidity. These results are consistent with earlier observations by Gathilor and Ivanova [10].

The same coil with a pitch of 8 mm is also subjected to different wind speeds. As turbulence is increased by roughening in the first stages of frost growth the heat transfer coefficient increases temporarily, before dropping as the growth begins to restrict airflow. Initially, the coefficients are widely different for different wind speeds, but all approach a common value as time progresses, indicating the effect of significant airflow blockage.

The study can be generalized with the conclusion that many of the conventional geometric means of heat transfer enhancement, i.e., increasing the number and angle of fins, may also correspond to an increased susceptibility to frost buildup. For the cases tested, the coils with larger fin pitch and thus larger initial heat transfer coefficients were affected more adversely than coils with smaller fin pitch. Nevertheless coils with higher fin pitch tend to remain more effective than those with lower pitch, though the heat transfer coefficients for both types begin to approach similar values as time goes on.

2.2 Traditional experimental measurement techniques

Although frosting and defrosting processes have been under study for several years, nearly all recorded experimental techniques are similar in nature. An analysis of the various methods applied to determine experimental quantities of value shows that there is much room for

improvement in terms of reliability and accuracy. The analysis presented here includes methods used to reach primary goals described in the general literature section, the conditions under which those methods were applied, and descriptions of the physical nature of the experiments. Several older experiments are included for completeness, but the vast majority of the projects evaluated range from 2004 to 2010. The intent is to produce an in depth comparison of recent and current frost research to draw conclusions about the validity of the current experiment as well as to outline areas where improvements can be made in general.

Much of the literature has neglected to include estimates of error associated with measured quantities, which makes numerical accuracy comparison difficult. Despite that shortcoming, the experiments can be compared qualitatively so that insight can be gained on the validity of new experiments. Qualitative comparison also allows areas of possible error common to multiple projects to be identified and discussed. Thus, the scope of this analysis is qualitative, but comparisons of actual error are made where possible.

In recent years, methods have become more diverse. Unfortunately, such diversity has not translated into improvement, as most of the current experiments appear to be subject to the same uncertainty as their predecessors. In particular, the precise measurement of vital parameters such as frost mass, thickness and density remains a challenge. Many experiments are limited by their geometry and technological capability, though some have managed to obtain reasonably accurate results, mainly with flat plate type designs. The type of experiment is directly related to difficulties in measurement and analysis

The types of experiments aimed at determining key parameters associated with frosting and developing generalized correlations are relevant to the experiment at hand and provide good models for comparison. For the most part, these types of experiments utilize flat plate geometries in either forced or free convection with or without fins. The simplicity of this design makes it easier to obtain accurate measurements and to study the frosting mechanisms used to develop governing equations and correlations, though their results are less directly applicable to full scale refrigeration systems.

A large percentage of modern research is focused on the analysis of heat exchanger performance under frosting conditions. While that is an important area of research, the physical complexity added to the experimentation by the use of tube and fin heat exchangers makes accurate measurements more difficult to obtain, and the added variables make analysis more difficult. The information gained from these types of experiments is valuable to improving the macroscopic performance of refrigeration systems in terms of heat transfer, defrosting time/frequency, and power consumption. Results and correlations obtained from such

experiments are less likely to be valid when applied to non-similar situations and in general shed less light on the physical processes involved with frost formation than flat plate type experiments. Nevertheless, they are included in here because the same quantities must usually be determined.

There is also a share of research concerned with characterizing changes in frost behavior due to changes in cold surface properties and with describing more specifically the crystal structure of the frost layer. Though the results from such experiments are generally more qualitative and focus on phenomenological behavior, the experimental techniques are often similar to those found in the other types of frost experiments. Thus, they are included here so that the widest variety of techniques possible can be compared.

2.2.1 Experimental Design

There are typically wide variations in the design of experimental setups. The test chambers themselves range anywhere from small, climate controlled chambers to full sized wind tunnels and open air experimentation. In addition, parameters like measurement methods, test surface/coil orientation, scale, materials, cooling methods and ambient conditions may all be chosen differently from apparatus to apparatus. Each of these choices has an impact on the final results of the experiment, and so must be chosen carefully to suit the end goal. Here, the experimental setups of recent research are explored.

In all cases experimentation is performed on a test specimen in an environment that is either at constant ambient conditions or one whose conditions can be controlled accurately. The test specimen must be cooled by some method to a subzero temperature below the dew point of the environment for frosting occur. Cooling is generally accomplished with a glycol/refrigerant loop or with a thermoelectric module and heat sink. Humid air is then allowed to reach the surface via forced or free convection, and frost buildup occurs over the course of several hours during which time the experimental parameters of interest are measured and qualitative observations are made. These measurements and observations are most commonly made with different types of thermocouples, infrared thermometers, hygrometers and visual techniques. Depending on the goal of the experiment, the data is used to generate correlations, verify theory, or draw conclusions about the nature of frosting and defrosting.

In many cases with adequate theoretical preparation, the more difficult measurements (such as frost thickness and surface temperature) can be avoided thereby improving the reliability of the experiment. When the desired outputs of the research are oriented toward system, (e.g., heat transfer and pressure drop), it is sometimes possible to work around the need for certain measurements by developing the governing equations appropriately. In other cases, when the

frost itself is of primary interest, there is little room for movement and difficult measurements must be made accurately and reliably. That is perhaps one reason for the wide range of experimental setups adopted in the course of research.

The most commonly used experimental enclosures are medium sized chambers and wind tunnels, and nearly all recent research has been performed with these types of facilities. Liang, et al. [24] used a small, temperature and humidity controlled room to observe the influence of contact angle on frost growth under free convection. The test surface was oriented horizontally so that droplets could form easily. In that case, the cooling method was thermoelectric and the test surface was a 16 cm^2 copper plate.

Ngonda and Sheer [29] made use of an environmental chamber (60 m^3 in size) and a copper coil under forced convection for measurement of coil duty during frost growth. The coil was contained within an attached duct so that the airflow conditions from the chamber could be controlled. A trichloroethylene refrigerant blend was used to cool the coil for testing. The dimensions of the coil were approximately 0.01 m^3 including fins. By measuring outputs relevant to coil duty (flow rate, pressure drop, heat transfer, and power input), the researchers were able to compare their results to theoretical models without needing to measure parameters such as frost mass, thickness or temperature. While both thickness and temperature were present in the models, the final outputs of the models were the same quantities measured. In effect, the important but hard to measure parameters were lumped into the experimental analysis.

Youbi-Idrissi and Guilpart [38] performed an experiment in a chamber of similar size (40 m^3) when evaluating coil performance under forced convection. The refrigerant used was R404A, and the test section was located within the chamber itself. The test apparatus was designed to simulate a refrigerated storage cell so that the result could be applied to design situations.

Chen et al. [4] used a cryogenic wind tunnel insulated with polystyrene foam to determine the effects of fin pitch, air velocity and air conditions on frost growth and the resulting decreases in coil performance. The copper coil was cooled with a 50% glycol and water mixture circulated externally. The coil dimensions were approximately 0.0064 m^3, with dimensions similar to those used by Ngonda and Sheer.

Yamashita et al. [36] ran forced convection experiments on a flat test surface machined from 1050 aluminum mounted in an acrylic duct. Their goal was to study frost properties (both qualitatively and quantitatively) in abnormally low temperature environments, down to -20 °C. The duct was approximately 0.04x0.04 m in cross section by 0.1 m long, and the test surface was

mounted in a vertical position. A thermoelectric module with a liquid cooled heat sink was used to cool the test surface, which was 36 cm^2 in size.

One more unique experiment was carried out by Getu and Bansal [11] in 2007. Rather than constructing an experimental apparatus, they measured conditions and data in real refrigeration cases located at a nearby supermarket over a 12 h day of normal operation. The aim of the experiment was to compare models developed in earlier research to real world applications. The model inputs were determined by the measured data. The experiment was performed in two different types of cooling cases: glass door frozen food (GFF) and through frozen food (TFF) types. The exact nature of the setups was not described.

Iragorry and Tao [15], who have performed several other notable frost experiments dating back to early frost research, used a wind tunnel experiment while investigating frost growth and possible defrosting sensing systems. A flat aluminum plate was used as a test surface, oriented vertically under forced convection. The plate was of a similar size to those used in other research, around 16 cm^2, and was cooled by a thermoelectric module on a glycol heat sink.

Lee et al. [23] attempted to compare frost growth and properties on both flat plate, finned plate, and tube and fin heat exchangers under similar conditions. To do so, they employed an acrylic wind tunnel setup with the specimens located near the center. The test surfaces were copper tubes and aluminum plates and fins, cooled by 50% glycol water mixtures circulated externally in both cases. The plate was relatively large, at 300 cm^2 and the coil was smaller than usual at $2.2 \cdot 10^{-3}$ m^3.

The governing equations for frost growth were developed into a transient distributed model for frost growth by Chen et al. [3] in 2001. After solving the model numerically, the results were compared to those of a wind tunnel experiment of frost growth on a finned plate. The aluminum plate was 100 cm^2. Air was drawn into the tunnel from an environmental chamber at preset conditions. The details of their apparatus were not discussed in depth.

In another wind tunnel experiment, Liu et al. [25] compared the mass of frost accumulated on a copper coil over a period of 40 minutes with that predicted by the distributed model for frost growth presented by Chen et al. for a flat finned plate. The system was cooled by a heat pump, and the coil was approximately 0.67 m^3, which is somewhat larger than usual.

Fossa and Tanda [8] performed a free convection analysis of frost growth that utilized a thin, vertical test chamber that was open on the top and bottom ends to allow air circulation. The chamber was located in a climate controlled lab to maintain the ambient conditions, and the plate was cooled by a glycol mixture. A relatively large copper test surface was used, about 254 cm^2

compared to the 30 - 60 cm^2 sizes most frequently used. The chamber was built from Plexiglas to allow observation, and was around 0.17 m^3.

Hao et al. [12] also ran a free convection experiment in lab conditions. No enclosure was used but the ambient lab conditions were controlled. The test setup exposed a horizontal aluminum test surface (16 cm^2) of the flat plate type to ambient air, so that holographic interferometry could be used to obtain the temperature distribution of the air just above the test surface during frosting. During the test, cooling was provided by a thermoelectric module with a 70% glycol water loop.

There has not been much comparative research wherein smaller scale, more carefully controlled test chambers have been used. Test setups have been, for the most part, either on a scale of meters or under forced convection in wind tunnels. The primary advantage of utilizing a smaller scale experiment is that the air conditions are easier to control, which translates directly into more reliable results.

Much research has been concerned with the testing and development of correlations for frost properties and thickness and determining the influence of certain parameters on frost growth. The majority of recent research has been under forced convection conditions, which represent more realistic approximations of actual operating systems. The free convection test setups are more appropriate for determining the validity of theorized governing equations and testing numerical and other approximate solutions to them.

For the reasons of controllability and end goals, the test setup used in this experiment is a free convection environment in a small scale chamber allowing for highly variable ambient conditions. The expected outcomes are experimental verification of a theoretical model governing frosting and defrosting and the application of these results to improve defrosting efficiency. Mohs [29] has explored this area in depth.

2.2.2 Test Surface Design

The choice of a frost growth surface is an important parameter. Test surface types can be divided into two general categories: finned and flat plates. The finned plates almost always entail the use of pre-constructed cooling coils, usually consisting of small diameter copper tubing (6-12 mm) and aluminum fins. In some experiments, such as those of Iragorry and Tao [15] and Chen et al. [3], finned plates have been used. In the case of Iragorry and Tao, the fins were removable so that frost mass could be measured after the experiment. Flat plates are usually custom made for the experiment, either from copper or aluminum. The surface material used does not appear

to significantly impact frost growth (aside from the drop-wise condensation stage), and different materials are chosen for either ease of construction or thermal conductivity.

As previously discussed, the finned sections (either plate fin or tube fin) are used in forced convection test setups where the primary outcomes are correlations and observations relating to coil performance during frosting. The flat plate types and sometimes the finned plate types are used when careful measurement of frost parameters is needed as for the verification of frost growth and defrosting models.

Test surface orientation is another parameter that must be considered. In most experimental research, the choice of test surface orientation appears arbitrary. When coils are used, they are universally oriented as per their design criteria. In contrast plate types may be situated horizontally or vertically. In most cases, the differences between these orientations are questionable at best. By observation it is clear that gravity has little effect on the drop-wise condensation stage, the precursor to frost growth, owing to the small volume of the water droplets. Under certain situations the choice becomes important. In the case of Liang et al. [24], a horizontal surface was desired so that the influence of contact angle on frost growth could be observed. Hao et al. [12] used a horizontal orientation so that the holographic interferometry technique could be employed to measure the air temperature distribution just above the frost surface. For experiments concerned with defrosting, it is clearly desirable to use a vertically oriented surface so that the effects of slumping (the sliding of frost layers on water films due to gravity) can be included in the analysis. This is desirable since it is a natural occurrence during defrosting of commercial refrigeration systems.

The size of a test surface can also be important. Experiments utilizing fin and tube coils are done with commercially available or slightly modified sections. As a result they are typically of similar size. Usually these are from 150 to 300 mm in length and height, and 40 to 150 mm in depth. The tube diameters most frequently between 4 and 12 mm, though they are occasionally larger (Lee et al. [23] used 20 mm tubes), and the fin thicknesses are between 0.1 and 0.3 mm. For flat plates the sizing is generally more consistent. Most experiments use square surfaces between 40 and 60 mm per side and 1 to 1.5 mm thick. Again, there are several exceptions to this convention, notably Lee et al. [23] and Fossa and Tonda [8]. The dimensions are important because when combined with different methods of cooling, they can influence both the rate of heat removal and the temperature distribution in the surface parallel to the frost. For the most reliable results, it is obviously desirable to have a test surface of uniform temperature. The nature of most cooling setups makes this easier to achieve with smaller surfaces. The variation of temperature within the test surface should be avoided because in a non-uniform situation the

locations where frost parameters are measured become important, as they are affected by the temperatures of both the air and the test surface. These factors both complicate the reduction of experimental data and add additional source of experimental uncertainty. For flat plate testing, the best results have been achieved with small copper and aluminum plates of medium thickness. In the present experiment, a square aluminum surface of 38 mm and 3.2 mm thickness is used.

A final factor to be considered is surface roughness, though very little research on the influence of roughness on frost formation is currently available. Liang et al. [24] performed experiments to observe the relationship between contact angle and frost formation. For now the surface roughness is considered and recorded as a parameter, but is only important during the drop-wise condensation phase when the surface is still exposed. As most research is concerned with the frosting and defrosting after that stage, surface roughness is a less important factor.

2.2.3 Cooling Method

There are two general methods by which test specimens have been cooled in experiments, liquid coolant circulation and thermoelectric modules (TEM's). The former is most usually employed in experiments where the test surface is large (i.e., heat exchanger testing), and the latter in experiments with smaller surfaces (flat plate or finned plate types).

Within each of these categories, several variations have appeared. For liquid cooling the norm is a mixture of glycol and water (~50/50), but occasionally true refrigerants are used, such as trichloroethylene in the case of Ngonda and Sheer [29], and R404A in the case of Youbi-Idrissi and Guilpart [38]. In most cases, the coolant is circulated externally through a cooling loop until the desired temperature is reached, at which point it can be redirected through the heat exchanger. The external cooling method varies. In some cases, liquid cooling has also been used for flat surface type experiments. Lee et al. [23] and Fossa and Tanda [8] used this approach.

Thermoelectric modules can be constructed from different types of semi-conductors which have different temperature ranges and responses to applied voltage. The most influential parameter on the performance of a TEM is the cooling method chosen for the heat sink, since lower heat sink temperatures correspond to lower cold side temperatures. Usually, cooling is accomplished with a water/glycol mixture loop circulated to the back side of the TEM. In other situations, air cooling is sufficient to maintain the desired temperature difference. As long as ambient conditions are relatively constant, both methods exhibit reasonable stability.

The primary differences between liquid cooling and thermoelectric modules are size and controllability. Liquid cooling is not usually used for small test specimens, because of the rather bulky and complex systems required to achieve very low coolant temperatures. Liquid cooling of

the heat sink is common because such low temperatures are not a requirement (water bath circulation is sufficient). Because the temperature difference across a TEM is governed by the heat sink cooling, applied voltage and current, it is possible to control the cold surface temperature precisely and uniformly. In contrast, while coolant temperature can also be regulated very accurately, temperature variation may exist from the entrance to exit of a heat exchanger.

Another difficulty arises if the mass of frost in a heat exchanger must be determined accurately, since the mass of the final assembly cannot be easily compared with the initial mass. In most experiments, the mass of frost accumulated has been calculated based on changes in air humidity between inlet and outlet sections of the tunnels. In TEM configurations, the mass can usually be measured directly by removal and weighing of the test surface.

Even with these differences, either cooling method can be used effectively if care is taken to ensure that measurements are accurate. The size and controllability of TEM systems make them most suitable for smaller experimental setups designed to test wide ranges of conditions and frost properties. Liquid coolants, while occasionally used for flat surfaces, are required for heat exchanger type experiments designed for performance evaluation during frosting and defrosting and the development of correlations for frost growth under realistic operating conditions.

2.2.4 Heat Flux

In some experiments it is necessary to obtain the heat flux during frosting and defrosting. This is often the case when the desired outputs include system efficiency or COP, and if frost surface temperature is not measured directly (an energy balance can be combined with heat flux to determine the temperature). For full evaporator test sections, heat flux is not a quantity that may be measured directly as a result of the complex geometry involved. Under these circumstances the heat flux must be ascertained by system level energy balances.

In flat plate type experiments, heat flux is measured easily. The task is accomplished universally by the use of thin film heat flux sensors [8,15,36]. Such an approach is convenient because most thin film heat flux sensors also double as thermocouples, thereby making it possible to obtain measurements at the test surface cold side simultaneously and as a surface average. Typically the size of thin film sensors can be matched to the area of the test surface, but in cases where the sizing is not equivalent multiple measurement points can be averaged as shown by Iragorry and Tao [15]. In some cases both the heat flux and the frost-air interface temperature are measured for redundancy and to simplify the need for many calculations. The duplicate measurements serve to establish the validity of one another because the accurate measurement of air-frost interface temperature is difficult.

2.2.5 Air-frost interface/frost interface temperature

An important parameter in nearly all frost growth models is the temperature at the interface between the frost surface and convective air environment. Unfortunately that quantity is relatively difficult to measure accurately because of the sensitivity of the frost layer to physical contact and because its location varies with the time of measurement as the layer grows in thickness. Typically the interface temperature is not measured during coil type experiments. The reason for its omission is that the temperature loses much of its meaning in such circumstances because the frost thickness varies widely depending on the measurement location (i.e., fins or tube surface, depth into exchanger, etc.). As a result the interface temperature also varies. It is substantially simpler to calculate quantities of interest based on system energy balances in such cases.

In plate type experiments, measurement of the interface temperature is simpler, but it still poses several challenges. When thermocouples are used to measure temperature directly, concerns may arise because it becomes difficult to specify exactly where the surface is located. The porosity of the frost layer resulting from the crystal structure means there is no exact surface height, and consistent results are difficult to obtain. The same conditions can also result in large portions of the thermocouple being exposed to the convective environment while measurements at the surface are being taken thus reducing their validity. Finally the frost crystals are physically fragile and highly sensitive to temperature changes if they are near 0 °C. Heat conduction and pressure due to contact with the thermocouple may cause the structure to collapse locally and influence the measurement. Adding to the difficulty is the movement of the interface over time, which means that the thermocouple must also be capable of movement. Fossa and Tanda [8] solve the problem with the use of a micrometer so that thickness can be measured simultaneously. However they also determined the surface temperature with infrared and electrode methods to maintain validity. In general physical measurement of the air-frost interface temperature has been avoided because of the above issues and non-invasive methods are most frequently utilized.

The most common non-invasive form of temperature measurement in is by infrared (also called radiation) temperature sensors. Infrared sensors operate by calculation of the surface temperature based on radiation and emissivity. While infrared measurement is an accurate method of measurement after calibration, there may be some error involved with the estimation of the emissivity of the frost surface especially since it varies depending on crystal structure (and thus transient ambient and surface conditions). There has been little investigation into the issue, but the use of infrared sensors for defrosting sensing systems has been explored by Iragorry and Tao [15]. Another problem that arises with infrared measurement is the influence of mediums

between the sensor and surface. In the case of small experimental chambers, there often exists a window of some sort (typically acrylic) between the observer and the frost surface. Under such circumstances the reflectivity of the window renders the infrared sensor useless if the intention is to use it from externally. The difficulty resulting from reflection could be avoided with a carefully designed setup and a dedicated interior sensor.

Hao et al. [12] have performed experimentation with another form of surface temperature measurement, known as holographic interferometry. Holographic interferometry can be used to obtain the temperature distribution in the air adjacent to the surface by using the interference patterns of light waves. Interferometry is capable of producing accurate projections of the temperature distribution across the entire surface rather than at a single location or at various data points which is a clear advantage. Furthermore it does not depend on difficult to estimate parameters such as the surface emissivity but only on the bulk air properties that are much easier to determine accurately. Holographic interferometry is clearly the best method of surface temperature measurement that has been applied, but the technical and physical difficulties of implementing this approach make it unsuitable for many experiments.

The infrared sensing technique appears to be the most common, and easiest to implement of the various surface temperature measurement methods. With appropriate calibration and careful experimentation, this method can be used accurately. It alleviates the difficulty associated with direct physical measurement and does not require the complex system design needed for holographic interferometry.

2.2.6 Ambient conditions

Most analyses of experimental data acquired for frost growth depend on the conditions under which it was acquired, and those conditions must also be measured accurately. The important quantities associated with most frost data analysis and correlation development are air/wall temperatures and humidity. In forced convection experiments the air flow rate is also important. Two of these parameters (temperature and flow rate) are typically simple to measure and do not require much discussion. Furthermore the type of experiment (coil or plate type) has little influence on the decisions regarding them. Ambient air temperatures are measured universally with thermocouples mounted near the test surface in free convection experiments and in grids across the airflow for forced convection experiments. Flow rates are measured with nozzles [29], flow rate sensors [4], and hot wire anemometers [36]. None of the devices are particularly advantageous under the circumstances, and the choices are made to suite the individual apparatus.

Humidity, while not difficult to determine, is an extremely important parameter in frost growth, so care must be taken in its measurement. The methods of measurement are varied, from the use of traditional wet and dry bulb thermometers [23] to techniques of sensible heating [29]. Much research has been conducted with the use of hygrometers. Though all of the methods are within the same range of error, a study of the apparatus used by Lee et al. [23] suggests that the wet and dry bulb thermometers may be slightly more accurate than the typical hygrometer. In general relative humidity has been determined to within 1-3 % for all current research. Furthermore the type of experimental setup has little bearing on which method of measurement can be used.

2.2.7 Frost mass

The subject of frost mass measurement is one that entails much discussion. The mass of frost deposited along with its density directly affects the performance of the cooling surface. Frost deposition is affected by all of the associated parameters (ambient and surface temperatures, humidity, flow rate, etc.), which makes it a complicated parameter to predict. A great many correlations have been presented in attempts to predict frost formation (usually in terms of density or thickness) as a function of conditions and time which have all depended on the measurements of frost mass or thickness to be developed. As a result, the accurate measurement of frost mass is of paramount importance in a large portion of frosting experiments. Many methods of frost mass measurement have been proposed which are discussed in turn below. It should be noted that frost mass is rarely measured directly in experiments involving fin/tube coils because of the associated technical difficulties. Rather it is calculated based on the change in humidity between the inlet and outlet air streams. All of the methods explored here are used for flat plate or finned plate experiments with the exception of Lee et al. [23], who have also measured mass on a finned tube setup.

The majority of research has made use of typical electronic scales for mass measurement. In all other cases the mass is calculated based on visually measured volume combined with density correlations. In order to use a scale, the frost must be either deposited onto the scale directly by scraping from the surface by either removal and weighing of the frosted surface, or by continuous measurement of the apparatus weight [8,25,36].

By far the most common method of measurement is the use of removable frost formation surfaces. In contrast to the scraping methods removable surfaces can be weighed at different

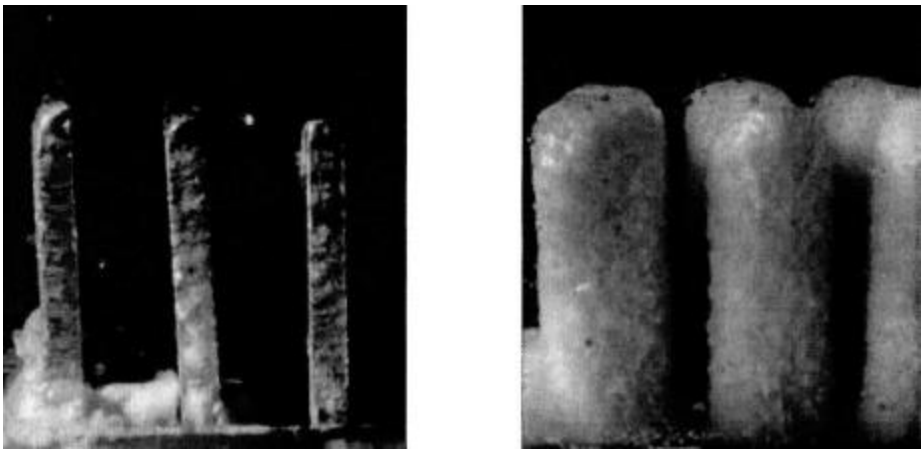

Figure 5. Removable fin technique used by Iragorry and Tao to measure frost mass [15].

times during the experiment instead of just at the end. Weighing provides a more direct way of evaluating the mass as a function of time and conditions.

Although many studies have used that approach, the specifics are widely varied. Iragorry and Tao [15] used removable fins attached to a base plate so that the entire assembly could be weighed at various times. Their setup is illustrated in Figure 5. Thomas et al. [34] used a similar method, but wrapped the fins in plastic wrap after removal to prevent accidental changes. Mao et al. [27] measured frost buildup on aluminum disks and measured mass by removing and weighing the disks.

An interesting approach was used by Chen et al. [4], who measured mass on both flat plate and fin and tube setups by applying strips of aluminum tape to the surfaces before the experiment. At certain times, strips could be removed and weighed.

One of the issues associated with measurement of frost mass by either removing the test surface or scraping is that the test session must be interrupted to obtain the measurement. Although interruption is not a problem in some cases, there are others (such as those with small containers and tightly controlled conditions) where it is an intrusive procedure that introduces avoidable potential sources of error. The resulting error can be avoided by using a continuous balance of the test apparatus. In a continuous method the mass of the frost can be monitored continuously after the scale has been calibrated appropriately, meaning it can be measured easily and without experimental interruption. Though continuous methods require the most careful calibration and control, they are certainly the most convenient.

Despite the differences between the various measurement techniques cited above, all of them rely on the use of an electronic scale to determine mass. As a result, they all share the same measurement error and, if carefully performed to avoid other types of error, are equally valid. However the removable surfaces and continuous monitoring are simpler to control and provide

clear advantages such as the ability for time dependent measurements without requiring repeated experimentation.

2.2.8 Frost thickness

As in the case of mass, frost thickness is a highly important factor in analysis. Since it has the greatest influence on air flow through a heat exchanger, a vital parameter in system performance, much research has been dedicated towards the development of predictive correlations for thickness as a function of time and conditions. Such correlations are presented as a design aid for the planning of defrost cycles and to provide insight into the behavior of frost.

Another reason for the significance of frost thickness is its direct involvement with the differential equations governing frosting and defrosting. The validation of these equations and distributed models is often a topic of interest, as in the work of Chen et al. [3] and Liu, et al. [25], which demands accurate measurement of frost thickness as well as other key parameters.

Nearly all research to date has made measurements of frost thickness via either visual methods based on image acquisition or physical measurement with micrometers and rulers. In some cases, other methods have been explored, e.g., Fossa and Tanda [8], who used an electrode measurement technique and verified their results with a micrometer.

As with the case of frost mass, much research involving the use of coils has used alternative methods to obtain frost thickness, such as the application of correlations from literature. Occasionally the frost is still measured directly under such circumstances if the geometry of the setup is conducive. Chen et al. [4] used a clear plastic ruler positioned between fins such that multiple readings could be obtained. While that method works, the frost thickness on coil type heat exchanger is dependent upon location, making it difficult to obtain representative averages.

For flat plate or finned type experiments, the measurements are usually accomplished by image acquisition by microscope and camera combinations which are capable of taking high resolution photographs at large magnifications, or by direct micrometer measurement. The latter of these while reliable and straightforward faces issues similar to those encountered with direct surface temperature measurement. It can be difficult to gauge the location of the frost surface accurately for the micrometer probe placement, and the pressure exerted by the tip may cause local variations in structure and height. Because of such issues the micrometer method is most effective when paired with a more accurate image acquisition method for verification. Measurements made with image acquisition are typically of far greater accuracy than physical measurements of frost thickness.

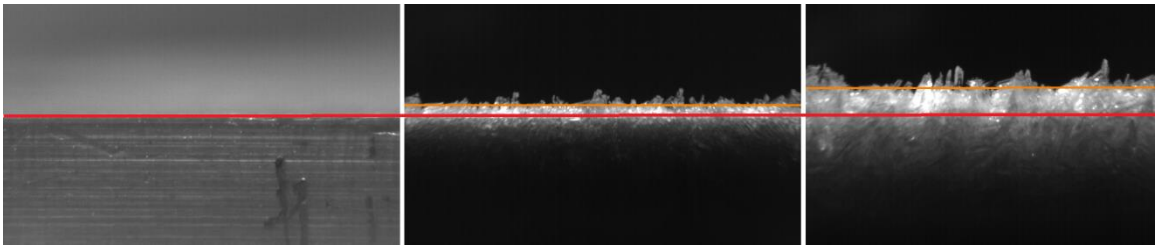

Figure 6. Illustration of the image acquisition method of frost thickness measurement. Acquired at a resolution of 133 pixels / mm.

With the appropriate system and calibration, resolutions in the lower micrometer range are easily obtainable with minimal error. Though the overall resolution is similar, image acquisition methods are of greater accuracy than micrometer measurements because the pitfalls associated with invasive procedures and the difficulty of estimating surface location are largely reduced. Because the crystal structure of the frost is clearly visible from a cross sectional view at high resolution, the average surface location (as opposed to voids and protrusions) is easily observed. Furthermore, the surface location is an average across the length of camera view, rather than at a singular point.

A typical image acquisition setup used for thickness measurement is described in detail in the next section, but in general consists of a microscope lens designed for use with a CCD camera linked to a computer system. The additional benefits associated with this setup also include continuous monitoring capabilities and depending on the system, the possibility of recording video during the process.

The typical visual measurement process is shown in Figure 6. After the images have been captured by the acquisition system, the baseline of the test surface is established prior to frost growth. As images are captured at later times, they are aligned and the average frost surface location is estimated visually as shown. The imaging equipment is usually calibrated beforehand to a scale in terms of pixels per unit length, so that the thickness can be calculated directly by measuring pixels once the surface line is drawn.

The advantages of measuring frost thickness by visual methods are clear and have been reinforced by the extensive use of such methods in modern research. Though the specifics may vary slightly from study to study, the methodology is straightforward. Physical measurement methods of thickness appear to be outdated except in the case of coil type experiments. In research presented here, a different approach is used (section 3.3.3).

2.2.9 Image acquisition and structure analysis

An essential area of experimental design is visual observation, particularly when such observations can lead to new or improved theories relating to the research. The case of frost growth is one such situation. As shown in the study of Yamashita et al. [36] the structure of frost may vary greatly depending on ambient conditions. The variation of the crystalline structure of frost layers corresponds directly to changes in physical properties of significance, such as thermal conductivity and density. If the goal is to understand and model frost formation and defrosting, then it is necessary that such dependencies are accounted for and explained. The small scale of structure changes makes them nearly invisible to the naked eye, and as a result nearly all modern research incorporates the use of high powered magnification equipment and computer based image acquisition systems.

As explained in section 2.2.8, one vital measurement that is greatly improved by the use of advanced imaging technology is frost thickness. In general, the magnification of the image acquisition systems used in frost growth research gives the ability to make such measurements with accuracies down to 0.1 mm or lower.

Depending on the goal of the experiment, the total magnification of the system may vary. Liang et al. [24] used a system with a magnification of 320X to observe the effects of contact angle on frost formation, while Hao et al. [12] used an extremely powerful system with a magnification of 800X for microscopic observation and characterization of frost growth during the early stages of transition from the liquid to ice phase. Yamashita et al. [36], were able to take high resolution photographs of frost crystal structures under different temperature conditions (see Figures 2 and 3) by using a system with a magnification of varying power from 7X to 450X. It is apparent that a magnification ~300X or greater is desirable to obtain reasonable resolution when observing frost growth.

The image acquisition itself is accomplished with the aid of a microscope and CCD (charge coupled device) camera. These devices are designed for the acquisition of high quality image data, which makes them ideal for frost experimentation. While it depends on the exact setup, it is often possible to obtain recorded video during frosting and defrosting in addition to the high resolution photographs. Though video recordings are typically shot at lower resolution, the combination of photographs and video gives the researcher an observational ability that is powerful and relatively new.

Table 1. Experimental setups used in recent frost research.

Experimental Design					
Authors	Year	Enclosure	Convection	Orientation	Cooling Method
Hao, et al.	2005	Lab environment	Free	Horizontal	Thermoelectric w/ 70% glycol/water
Liang, et al.	2007	Climate controlled room	Free	Horizontal	Thermoelectric w/water
Cho, et al.	2010	Wind tunnel	Forced	Horizontal	Multiple surface types w/ 50% glycol/water
Iragorry, Tao	2004	Cold chamber (2x2x2.5 m)	Forced	Vertical	Thermoelectric w/glycol
Yamashita, et al.	2007	Air duct (0.04x0.04x0.1 m)	Forced	Vertical	Thermoelectric w/brine cooler
Fossa, Tanda	2001	Open chamber (0.2x3.6x2.4 m)	Free	Vertical	Flat surface w/ glycol
Youbi-Idrissi, Guilpart	2007	Storage room (40 m^3)	Forced	NA	Fin/tube evaporator w/R404A
Chen, et al.	2007	Cryogenic wind tunnel	Forced	NA	Fin/tube evaporator w/ 50% glycol/water
Getu, Bansal	2007	TFF/GFF	NA	NA	TFF/GFF evaporators
Liu, et al.	2005	Wind tunnel	Forced	NA	Fin/tube evaporator w/heat pump
Chen, et al.	2001	Wind tunnel	Forced	NA	NA
Ngonda, Sheer	2007	Environmental chamber (4x5x3 m)	Forced	NA	Fin/tube evaporator w/ trichloroethylene

Table 2. Comparison of test surfaces used for frost growth in recent experimentation.

Test Surface Design						
Authors	Year	Geometry	Material	Dimensions [mm]	Fin Thickness [mm]	Tube Diameter [mm]
Fossa, Tanda	2001	Flat plate	Copper	95 x 282	NA	NA
Hao, et al.	2005	Flat plate	Aluminum	40 x 40 x 1.6	NA	NA
Liang, et al.	2007	Flat plate	Copper	40 x 40 x 1.5	NA	NA
Yamashita, et al.	2007	Flat plate	1050 Aluminum	60 x 60 x 1	NA	NA
Chen, et al.	2001	Finned plate	Aluminum	100	NA	0.3
Iragorry, Tao	2004	Finned plate	Aluminum	40 x 40 x 3.8	NA	NA
Cho, et al.	2010	Flat plate and fin / tube	Aluminum plate/fins, copper tube	Plate: 150 x 200, tube: 38 x 38 x 150	0.1	20
Ngonda, Sheer	2007	Fin / tube	Copper w/ Al fins	300 x 150 x 250	NA	11.07
Youbi-Idrissi, Guilpart	2007	Fin / tube	NA	NA	NA	4
Chen, et al.	2007	Fin / tube	Copper w/ Al fins	300 x 80 x 270	0.3	8.5
Liu, et al.	2005	Fin / tube	Copper w/ Al fins	6.7 m^2 x 0.1 m	0.12	9.5
Getu, Bansal	2007	TFF/GFF	NA	NA	NA	NA

Table 3. Outline of experimental conditions used to obtain results in recent frost research.

Experimental Conditions					
Authors	Year	Test Surface Temp Range [°C]	Air Temperature Range [°C]	Relative Humidity [%]	Air Velocity [m/s]
Cho, et al.	2010	-5 to -15	0 to 7	84	1 to 2.5
Liang, et al.	2007	-5 to -25	NA	65 to 70	0.25
Ngonda, Sheer	2007	-35	0 to -12	8 to 142	NA
Youbi-Idrissi, Guilpart	2007	-10 to -25	-20	80 to 90	NA
Chen, et al.	2007	-24	-14	65 to 80	0.55
Yamashita, et al.	2007	-10 to -30	0 to -20	52 to 72	0.5
Getu, Bansal	2007	-30	NA	NA	NA
Liu, Zhu, Wang	2005	NA	0	70	NA
Hao, et al.	2005	-18 to -30	23	41 to 68	NA
Iragorry, Tao	2004	-20 to -26	-15 to -20	NA	3.3 to 10
Chen, et al.	2001	-30 to -41	-13 to -21	90 to 100	4 to 5
Fossa, Tanda	2001	-4 to -13	26 to 28	31 to 58	NA

Table 4. Modern experimental techniques used in frost related research, part 1.

Measurements I					
Authors	Year	Air-Frost Interface Temperature	Test Surface Temperature	Air Temperature	Heat Flux
Liang, et al.	2007	NA	8 T type TC's on surface	KANOMAX Thermo-hygrometer	NA
Yamashita, et al..	2007	3 radiation TC's	Embedded T type TC	T type TC's in airstream	Heat flux sensor
Iragorry, Tao	2004	Infrared thermometer	Embedded T type TC	T type TC's in airstream	HFS-3 heat flux sensor
Cho, et al.	2010	Infrared thermometer	Embedded T type TC	Dry / wet bulb thermometers	NA
Hao, et al.	2005	Holographic Interferometry	4 Embedded TC's	2 TC's above test surface, Fischer hygrometer	NA
Chen, et al.	2007	NA	T type TC's	Unspecified sensors	NA
Fossa, Tanda	2001	2 T type TC's on micrometer	5 Embedded T type TC's	Fine gauge TC's in airstream	3 Heat flux sensors
Liu, et al.	2005	NA	NA	NA	NA
Ngonda, Sheer	2007	NA	NA	T type TC's in airstream	NA
Youbi-Idrissi, Guilpart	2007	NA	NA	Humidifier / unspecified sensors	NA
Getu, Bansal	2007	NA	NA	NA	NA
Chen, et al.	2001	NA	NA	NA	NA

Table 5. Modern experimental techniques used in frost related research, part 2.

Measurements II					
Authors	Year	Air Velocity	Relative Humidity	Frost Mass	Frost Thickness
Liang, et al.	2007	NA	KANOMAX Thermo-hygrometer	NA	Visual via imaging system
Yamashita, et al.	2007	Hot wire anemometer	Dew point meters	Scraped onto electronic scale	Visual via imaging system
Iragorry, Tao	2004	NA	NA	Removable fins / scale	Visual via imaging system
Cho, et al.	2010	NA	Dry / wet bulb thermometers	Removable surface (Tape) / scale	Visual via imaging system
Hao, et al.	2005	NA	Fischer scientific hygrometer	NA	Visual via imaging system
Chen, et al.	2007	Turbo flow rate sensor	HCP-2 Multipoint humidity detector	Calculated based on humidity change	Plexiglass ruler between fins
Fossa, Tanda	2001	NA	Capacitance hygrometers	Scraped onto scale	Micrometers and electrodes
Liu, et al.	2005	Nozzle	Humidity transducer	Calculated based on humidity change	NA
Ngonda, Sheer	2007	ISA 1932 Nozzle	Sensible heating of extracted air	NA	NA
Youbi-Idrissi, Guilpart	2007	NA	Humidifier / unspecified sensors	NA	NA
Getu, Bansal	2007	NA	NA	NA	Calculated via correlation
Chen, et al.	2001	NA	NA	NA	NA

2.2.10 Tabulated Comparison

A large portion of recent (post 2004) and some earlier experimental work is summarized in Table 1 to 5. Specifically the experimental setups and operational conditions are compared across a wide range of parameters.

It is clear from the observation of these tables that the scope of research is still widely varied in nearly all areas. That is an indication that frost growth research is still in a relatively early stage. So far, most work has been focused on the analysis of the influence of important parameters during frosting and defrosting, such as air flow rate, temperature and relative humidity. Once the influence of those important factors (and any other contributing factors) is understood more fully, more refined theory can be developed. Quantitative results have been used primarily for the development of correlations designed for specific applications and for numerical validation of proposed theoretical growth models.

Some experimental quantities of interest, such as frost mass and surface temperature, remain difficult to quantify, and many relatively crude measurement methods are yet in use.

Even when these quantities can be determined accurately, the evaluation of other thermo-physical properties such as density, thermal conductivity and specific heat remains difficult. Since such properties remain dependent on the little understood development of the frost structure itself, they can only be estimated even if extensive properties and temperatures are known exactly.

It is obvious that there is great room for improvement in both the understanding of frost and in related experimental methodology. The early stages of frost growth and the internal structure are almost universally ignored in modeling, and the best models to date include gross approximations that depend on highly difficult to measure, or variable parameters. While the general details of frost growth and governing equations are known, the influence of all related parameters is still not well understood, and the variation of properties with those parameters poses a serious problem when it comes to accurate modeling.

Of the studies listed in the above tables, the one most similar in nature to the experiment described in this thesis is that of Hao et al. [12]. Although their experiment makes use of a holographic interferometer in a laboratory environment (as opposed to a small chamber), the other experimental parameters and methods are similar. The research of Yamashita et al. [36] is also similar except under forced convection conditions. As such, results are compared to these studies and others where possible.

2.3 Classification of correlations from literature

There have been several correlations developed from various studies that are typically used for comparison with experimental frost data as outlined by Irragory et al. [16] in their literature review. The classification of these correlations, in terms of the experimental conditions under which they were developed, is given in Table 6. These correlations are the most frequently used in recent literature, although many others exist.

2.3.1 Frost thickness

The majority of correlations for frost thickness are simply linear combinations of relevant parameters raised to experimentally determined powers. In most cases, the parameters considered are the temperature difference between the wall and air, or the frost surface and air, the absolute humidity of the ambient air, ambient air conditions and the Reynolds number based on dry surface hydraulic diameter. In some cases, dimensionless position parameters are also included (particularly for the case of forced convection) to account for the variation of thickness with location. In most cases the correlations correspond to flat plate types (horizontal or vertical), with the exception of Cremers and Mehra [6], who used a cylinder.

Table 6. Applicable frost thickness correlations and their development conditions.

Frost Thickness Correlations						
Study	Year	Wall Temp [°C]	Air Temp [°C]	Re or Air Velocity	Time [min]	Geometry
Schneider	1978	-5 to -30	5 to 15	4000 to 32000	60 to 480	Flat Plate
Cremers and Mehra	1980	-15 to -25	20	-	50 to 350	Vertical Cylinder
Mao, et al.	1992	-5 to -15	15 to 23	1.15 to 2.67 m/s	-	Flat Plate
Mao, et al.	1999	-20 to -41	-10 to -26	3280 to 13110	-	Flat Plate
Lee and Ro	2002	-10 to -20	5 to 20	1000 to 3000	-	Vertical Plate
Shin, et al.	2003	-22	12	1.57 m/s	-	Flat Plate

The correlations corresponding to the conditions in Table 6 are given in Eqs. (2.1) to (2.6):

Schneider (1978),

$$\delta_f = 0.465\left[\frac{k_i t}{h_{sg}\rho_i}\left(T_{fs} - T_w\right)\right]^{1/2}\left(\frac{t}{60}\right)^{-0.03}\left(T_{fs} - T_w\right)^{-0.01}\Pi^{0.25}F_t, \tag{2.1}$$

Cremers and Mehra (1980),

$$\delta_f = 0.12\left[t\left(T_{fs} - T_w\right)\right]^{0.43}, \tag{2.2}$$

Mao et al. (1992),

$$\delta_f = 0.156\left(w\right)^{1.723}\left(x^*\right)^{-0.098}\left(T^*\right)^{1.10}\left(Re_D\right)^{0.343}\left(Fo\right)^{0.655}, \tag{2.3}$$

Mao et al. (1999),

$$\delta_f = 9.183\cdot 10^{-5}\left(w\right)^{0.4}\left(x^*\right)^{-0.085}\left(T^*\right)^{-1.712}\left(Re_D\right)^{0.449}\left(Fo\right)^{0.669}, \tag{2.4}$$

Lee and Ro (2002),

$$\delta_f = 0.1083\left(w\right)^{1.704}\left(x^*\right)^{-0.1488}\left(T^*\right)^{3.177}\left(Re_D\right)^{0.1424}\left(Fo\right)^{0.6724}\left(D^*\right)^{13.36}, \tag{2.5}$$

Shin et al. (2003),

$$\delta_f = \left(0.0852 + 0.00134\cdot\gamma\right)t^{0.6954-0.00154\cdot\gamma}, \tag{2.6}$$

where the parameters required for evaluation are defined,

$$\Pi = \frac{P_a - P_g}{P_g - P_{gfs}}, \qquad F_t = 1 + 0.052\frac{T - T_{tr}}{T_{tr} - T_w}, \qquad Fo = \frac{D_{T=T_a}\,t}{D_h{}^2}.$$

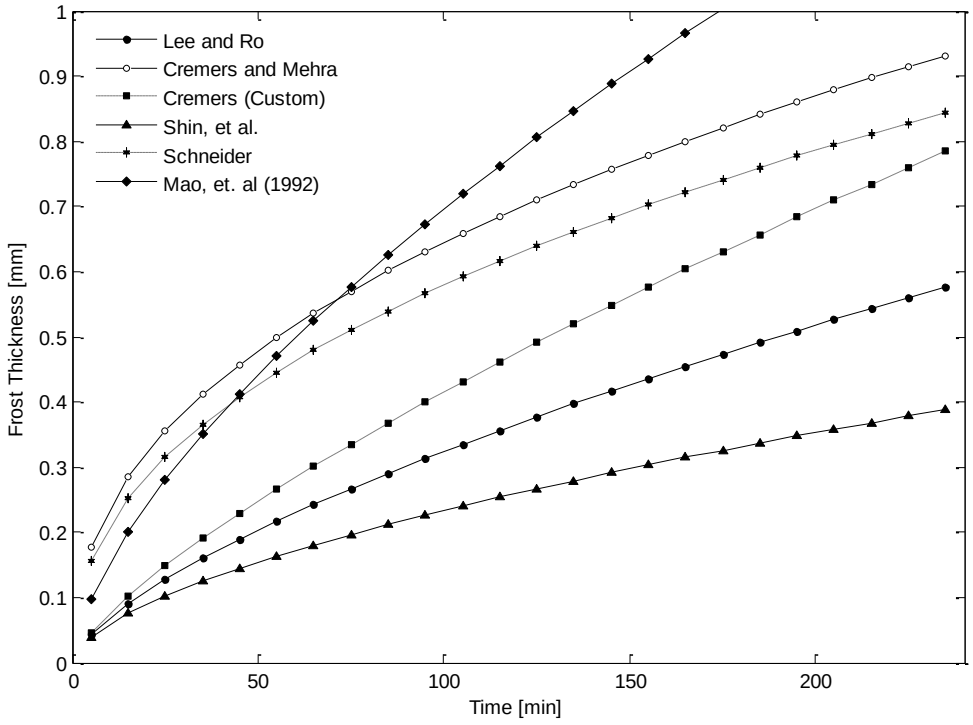

Figure 7. Comparison of correlations for prediction of frost thickness. T_w = -10 °C, T_a = 0 °C, ω = 0.003, Re_D = 100 (free convection).

$$D^* = \frac{D_{T=T_a}}{D_{T=T_{tr}}}, \qquad T^* = \frac{T_{tr} - T_w}{T_a - T_w}, \qquad X^* = \frac{x}{D_h Re_D Sc}.$$

Equations (2.1) to (2.6) are plotted in Figure 7 for a hypothetical set of free convection conditions with dimensions modeled after the experimental setup used for the test chamber described in chapter 3. Equation (2.4) has not been included because its bounding conditions do not fit the demonstrative model, which results in a skewed and more difficult to observe plot when it is combined with the more fitting correlations.

All of the equations tend to follow a power law fit closely. The difference between them lies in the evaluation of coefficients. It is interesting to note the close relationship between the correlations presented by Cremers et al. [6] and Schneider [32]. Although the equations appear to differ greatly in a mathematical sense, they predict a nearly identical growth profile. This agreement is an indication that the older Schneider correlation has managed to capture a more detailed view of the frost growth process.

Table 7. External conditions for empirical thermal conductivity correlations.

Frost Thermal Conductivity Correlations						
Study	Year	Wall Temp [°C]	Air Temp [°C]	Air Velocity [m / s]	Max Density [kg / m^3]	Geometry
Yonko and Sepsy	1967	-10 to -30	20 to 25	-	573	Flat Plate
Sanders, et al.	1974	-22 to -11	-10 to 0	4 to 9	500	Flat Plate
Lee, et al.	1994	-15	25	0.5 to 2	400	Flat Plate
Le Gall, et al.	1997	All	All	All	800	Flat Plate

2.3.2 Frost thermal conductivity

Thermal conductivity is an important parameter because the solutions of the governing equations for frost growth depend heavily on it. Furthermore thermal conductivity may vary widely based on the frost density and crystal structure, which makes it impossible to assume a standard thermal conductivity for frost. Instead the conductivity must be either measured experimentally or determined by the use of empirical correlations.

For this experiment, the thermal conductivity of the frost layer is established by the use of correlations from recent literature. The measurement of thermal conductivity is not simple to obtain accurately in many experimental setups. Parameters upon which the thermal conductivity depends, however, can be determined with greater accuracy, making the use of empirical correlations a preferable approach. Several different accepted correlations are compared. Although they cannot be verified here by experimental data (unlike thickness correlations), they can be evaluated by qualitative comparison based on knowledge of the frost growth process.

Four correlations are compared. The correlations are developed to be valid within the range of the external conditions listed in Table 7. The correlation presented by Le Gall et al. [20] is the most universal, as it is based on a theoretical model as well as experimental data. The other three are fully empirical relations based on curve fits to frost density. The correlations are given below in Eqs. (2.7) to (2.9) according to year:

Yonko and Sepsy (1967),

$$k_f = 0.02422 + 7.214\times10^{-4}\rho_f + 1.7917\times10^{-6}\rho_f{}^2, \tag{2.7}$$

Sanders et al. (1974),

$$k_f = 1.202\times10^{-3}\rho_f{}^{0.963}, \tag{2.8}$$

Lee et al. (1994),

$$k_f = 0.132 + 3.13\times10^{-4}\rho_f + 1.67\times10^{-7}\rho_f{}^2, \tag{2.9}$$

LeGall et al. (1997),

$$\frac{1}{k_f} = \frac{C_1}{k_{perp}} + \frac{1-C_1}{k_{par}}, \tag{2.10}$$

where the variables k_{perp} and k_{par} correspond to thermal conduction in the directions perpendicular and parallel to the cold surface. The basis for the distinction is that heat conduction may initially occur mostly perpendicular to the surface since the frost formation process is at first dominated by vertical growth. After bulk densification begins, the potential for conduction parallel to the surface is increased.

The components of thermal conductivity in the horizontal and perpendicular directions depend on the crystal structure and locations of voids. As a result the components can be expressed as functions of the porosity, which describes the volume ratio of air to ice within the layer. The proposed relationships are given in Eqs. (2.11) and (2.12) where the parameter ε_i represents the volume fraction of ice to air as opposed to the more commonly used definition which is that of air to ice,

$$\frac{1}{k_{perp}} = \frac{1-\varepsilon_i}{k_a} + \frac{\varepsilon_i}{k_i}, \tag{2.11}$$

$$k_{par} = (1-\varepsilon_i)k_a + \varepsilon_i k_i. \tag{2.12}$$

The constant C_1 is determined by the experimental correlation of Auracher [1] to be,

$$C_1 = 0.042 + 0.42 \cdot (0.995)^{\rho_f}. \tag{2.13}$$

Equations (2.11) and (2.12) can be interpreted on a physical basis to shed more light on the theory. The parallel conduction model of Eq. (2.12) can be thought of as conduction throughout a homogeneous medium composed of two different materials. The conductivity in that case is based upon the ratio of the component materials and the thermal conductivity of each material. Equation(2.11), which represents conduction in the direction perpendicular to the cold surface, is analogous to the inverse sum equation used to obtain electrical resistance for resistors in parallel (just as Eq. (2.11) is analogous to a series combination). This interpretation makes

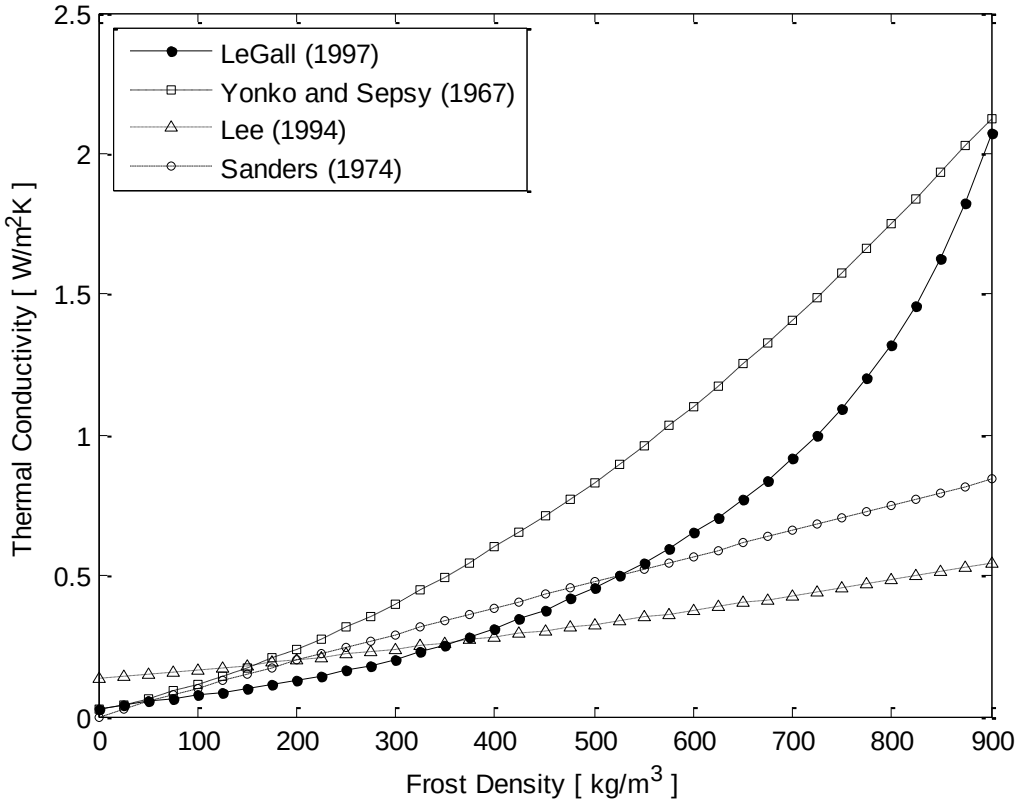

Figure 8. Comparison of frost thermal conductivity correlations.

physical sense because conduction perpendicular to the surface will take place through either frost or air depending on location.

For the most part, frost peaks and valleys persist even after some of the bulk densification has taken place, which means the definitions of parallel and perpendicular described by Eqs. (2.11) and (2.12) should remain separable for most of the duration of frost growth. After bulk densification advances significantly, the individual directions become more convoluted, but in their sum describe fully the behavior of the frost layer in terms of heat conduction.

The comparison of Eqs. (2.7) to (2.9) is shown in Figure 8 for a variation over frost layer densities of 0 to 800 kg/m^3. It is immediately evident that in the lower ranges of density, the correlations tend to agree. However as the density approaches that of ice (~920 kg/m^3) correlations presented by Lee and Sanders [21,31] tend to under predict the conductivity, whereas that of Yonko and Sepsy [37] tends to over predict owing to the mathematical form of the equation. As a result the range of validity of these equations has been limited to frost densities of less than 600 kg/m^3.

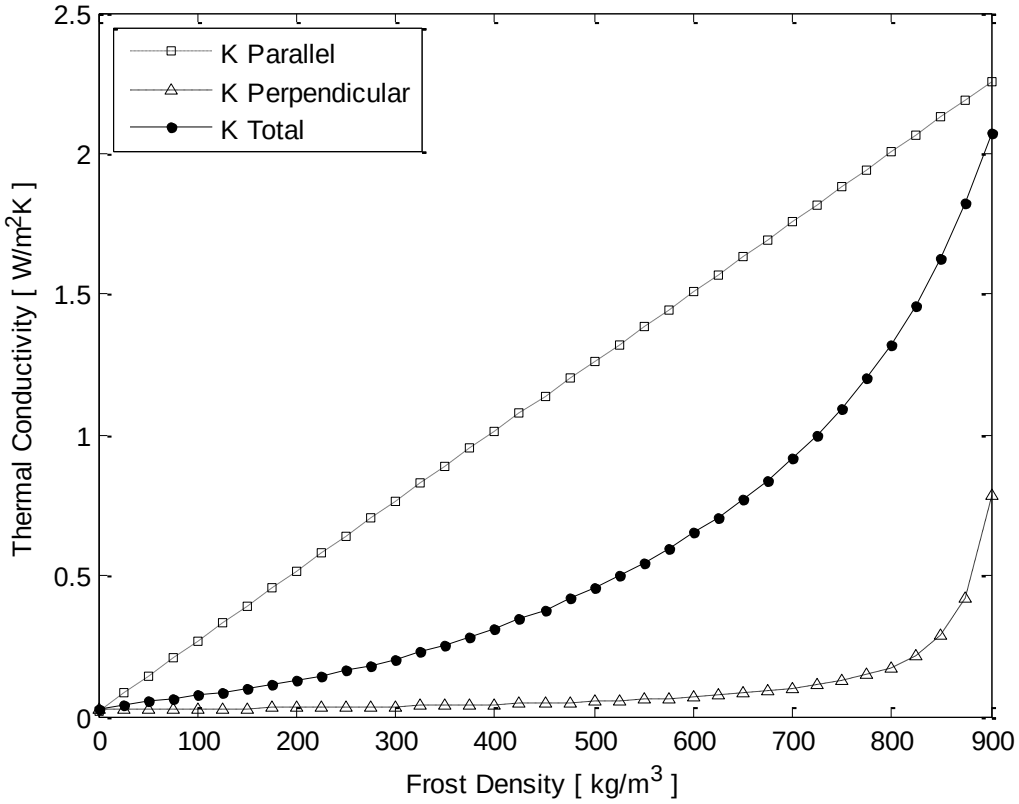

Figure 9. Variation of thermal conductivity in the parallel and perpendicular directions.

The correlation presented by Le Gall et al. [20] remains valid over a wider range of conditions because it accounts for the changes in frost crystal structure. Because of its theoretical basis, it is chosen for this research to be the most suitable correlation for obtaining frost thermal conductivity. The behavior of the correlation is illustrated with Figure 9, which shows how the two thermal conductivities vary over time compared to the overall (isotropic) conductivity.

The thermal conductivity in the direction parallel to the surface increases linearly over density, because it depends directly on the quantity of holes (or the porosity) of the layer which is a linear function of composition. The conductivity in the perpendicular direction, on the other hand, remains low for the majority of frost growth. As time goes on (and density increases), bulk densification phase begins. Most frost growth during this time is within the layer as opposed to on top of it, and the initially large gaps between peaks are filled in, thereby increasing the thermal conductivity. The total thermal conductivity is the linear combination of the individual conductivities and is taken as an isotropic property depending only on frost density.

Thus the major problem in determining thermal conductivity is that of obtaining the density at a given time, and multiple methods exist. It is preferable to obtain the density by direct

measurement of mass and thickness to ensure accuracy. However in the absence of this possibility, the correlation presented by Hayashi [13] can be used if the frost surface temperature is known,

Hayashi, et al. (1977),

$$\rho_f = 650e^{0.277T_{fs}}. \tag{2.14}$$

Other correlations may also be used, but they are not reviewed here since the method of direct measurement is a better approach. A third alternative technique is to calculate the density from a visual measurement of porosity. This method has benefits over other methods and may be just as accurate if the system is calibrated correctly. See section 3.3.3 for a detailed description of this method. Once the density is known, frost porosity can be calculated easily (or the density from porosity) by using the definition of porosity as described by Eqs. (3.13) to (3.16).

3 Experimental Setup

3.1 General details

In accordance with the typical experimental setup outlined in section 2.2, the apparatus used for this experiment is designed with the goal of high accuracy measurements. In addition to employing many of the traditional measurement methods described earlier, new techniques are tested that may improve experimental accuracy in certain areas. Though the final objective of the experiment is the acquisition of data for validation of a defrosting model presented by Mohs [29], the results are used here for an analysis of experimental methods and measurement validation. To that end the testing facility is described with an emphasis on parameters relating to measurement methods and accuracy. A more detailed report on the nature of the experiment and parameters not included here but is given by Mohs [29].

The chapter is split into two sections for clarity. The first section gives a description of the experimental facility itself along with relevant parameters and information. Included are a physical description and illustration, sizing and environmental factors, and possible sources of error. In the second section, the experimental methods and calculations used to obtain important parameters are described in detail. In some cases, new methods are employed and their results are compared to the traditional methods.

3.2 Experimental setup

A schematic of the experimental apparatus is shown in Figure 10. The design incorporates a small insulated polycarbonate chamber within which a test surface is mounted in a vertical orientation. The test surface is mounted on a cooper heat spreader block and a stack of two thermoelectric modules in series, which are used for cooling the surface to temperatures as low as -20 °C. Heat generated by the modules is rejected to the ambient air via a forced convection sink.

The interior air temperature is moderated by two thermoelectric modules in a parallel assembly mounted on the top side of the chamber. An interior sink is used along with a set of electronic fans to aid in the cooling process. Removed heat is rejected to cold water through a small cooling block. Cooling water is run from a tap of approximately constant temperature to avoid the need for further rejection.

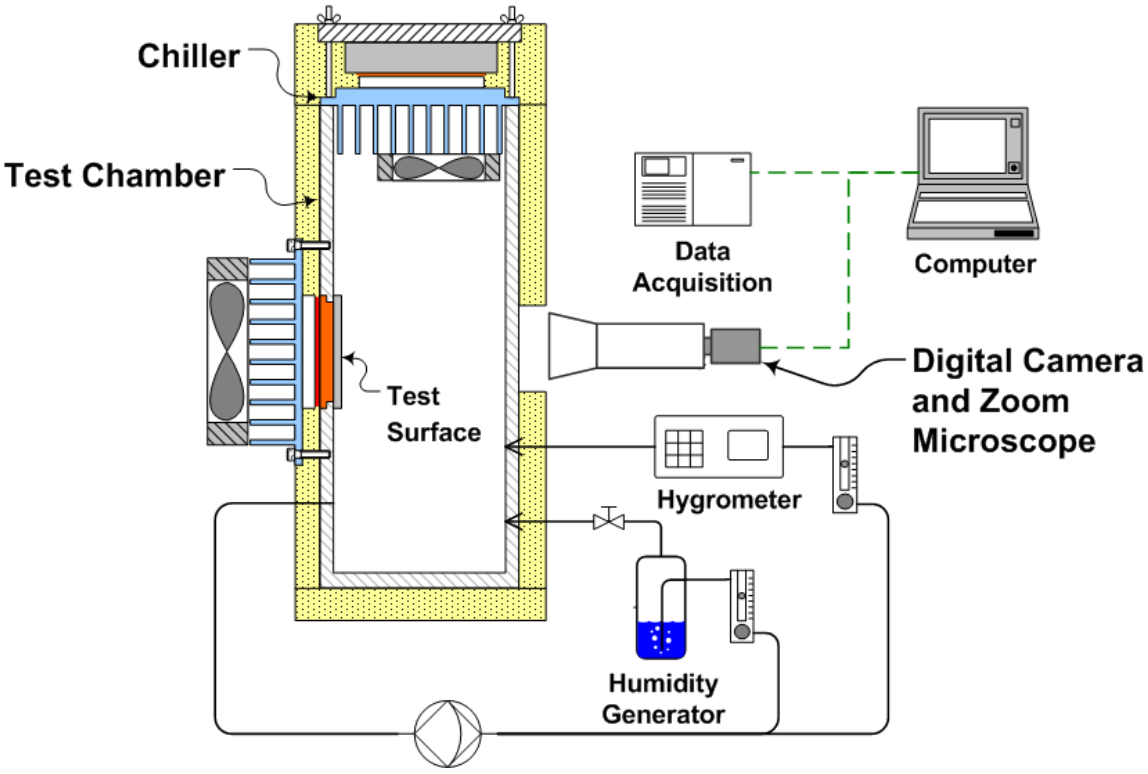

Figure 10. Schematic of experimental apparatus. [29]

To adjust the interior air dew point, circulation lines are attached as shown in Figure 10. Air is pumped out of the chamber at a constant volume flow rate using a sealed pump system. After passing through the pump, the airflow is split into a two streams which pass through adjustable flow meters so that the ratio of airflow between the two lines can be controlled. One line is then passed through a pool of water for humidification, while the other is used for a measurement of dew point using a typical hygrometer before being returned to the chamber. By beginning with a dry air chamber and adjusting the flow ratio, the desired chamber dew point is obtained.

Two holes are cut into the insulation through which the imaging equipment is able to see clearly the test surface. High resolution cameras are used for both cases, to acquire real time images of the front and side of the test surface simultaneously at high magnification. The images are collected via a computer system. Both cameras are also capable of capturing video at reasonable frame rates.

Aside from air circulation lines used to control the interior dew point, the chamber is totally sealed so that conditions may be precisely maintained once a steady state is reached. After construction the apparatus is not opened or altered until experimentation is complete.

The important parameters to be measured physically are temperature, heat flux and dew point. Temperatures are obtained by the use of thermocouples placed in appropriate locations (see section 3.3.2) and heat flux by a thin film heat flux sensor placed between the thermoelectric module and heat spreader. Data from these sensors is collected by a computer with a logging system for later analysis.

In addition to the thermodynamic properties, the mass must also be measured. The exact procedure for this is outlined in section 3.3.2. Frost mass is measured as the change in water mass contained in the humidifier over time during the experiment and verified as a change in desiccant mass following the post experiment dry out procedure.

3.2.1 Test chamber

As described previously, the test chamber is of relatively small size in contrast to many of the test setups used in prior frost research (section 2.2.1), which tend to be larger, wind tunnels or unenclosed entirely. The advantages to the present design are clear because the interior environmental conditions can be maintained more easily and reliably. In addition the small internal volume makes it possible to operate the system over a wide range of conditions without requiring large external cooling units and humidifiers for moderation.

The chamber used here has a rectangular internal geometry with a footprint of 0.10 × 0.05 m and is 0.20 m in height. The test surface is mounted on the wider wall so that closer views of the surface can be obtained. The walls are constructed from polycarbonate which was chosen because its optical quality is superior to that of similar plastics, and it is a good thermal insulator. The walls are 12 mm thick and are surrounded by 25 mm of foam insulation except where viewing windows are located. Of the studies outlined in Table 1, only that of Yamashita et al. [36] has used a chamber with dimensions similar to the one described here. In that study however the chamber was an air duct with forced convection conditions.

3.2.2 Test surface and assembly

The test surface used here is of the flat plate type, with dimensions similar to those found in the studies of Hao et al. [12], Liang et al. [24], Yamashita et al. [36]. The plate is constructed from 5052 aluminum with a lapped surface and is a 38 mm square approximately 3.88 mm in thickness. The surface is mounted on a copper plate to encourage a more uniform flow of heat from the surface to the thermoelectric module, resulting in an even surface temperature (Figure 11). The copper plate (or heat spreader) is 9.5 mm thick, just over twice the thickness of the test

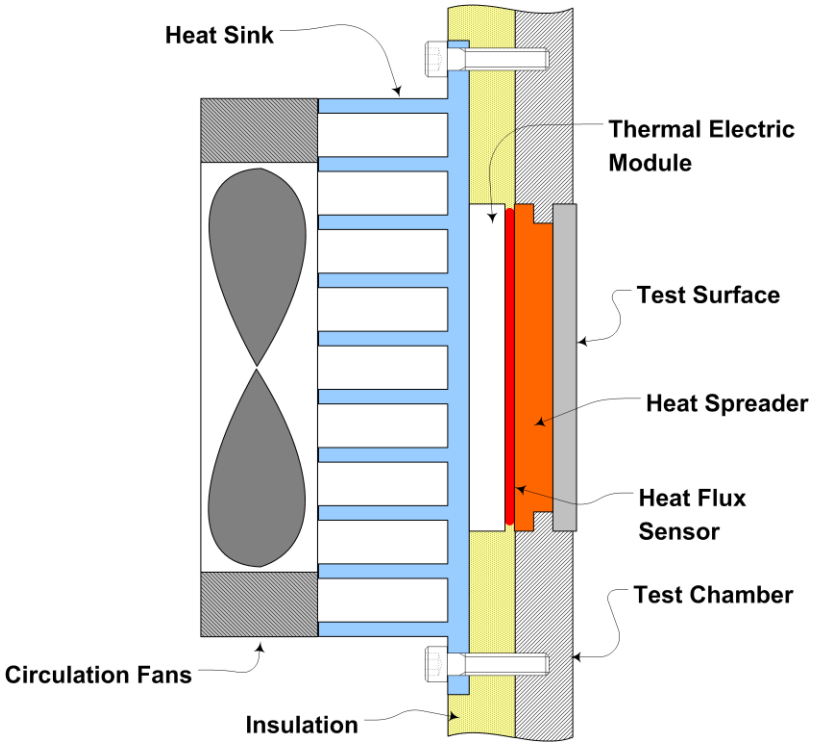

Figure 11. Schematic of the test surface assembly. [29]

surface. The interface between the surface and spreader is filled with thermal grease to reduce the contact resistance.

A thermoelectric module is used as the cooling method for the surface. The module is manufactured as a series stack of two individual modules so that the temperature difference between the external hot and cold sides can be made greater. The thermoelectric module is mounted to the back side of the spreader/test surface assembly, with an interfacial thin film heat flux sensor for measuring surface heat flux. Again, thermal grease is used in the remaining area to improve conduction.

Thermoelectric modules operate over a temperature difference, as opposed to an absolute temperature. Thus the minimum cold side temperature is governed by the cooling available on the hot side. Better hot side cooling results in the ability to achieve lower cold side temperatures. Here an aluminum pin finned heat sink is used along with an electronic fan to reject heat to the ambient environment as shown in Figure 11.

This cooling method is in contrast to that of most prior frost experiments, which typically involve the use of liquid cooling for thermoelectric modules. The module used here is a series combination, and low temperatures are achieved easily even without resorting to liquid cooling. The use of liquid cooling is excellent if the coolant temperature and flow rate can be well controlled because even lower cold side temperatures can be reached. That advantage, if not to as

great an extent, is shared by modules stacked in series. If temperatures in the desired range can be obtained in the latter manner, it becomes preferable since the heat rejection system (in this case air cooling) may be less complex and easier to control.

3.2.3 Testing conditions

By using the integrated top mounted cooling system as shown in Figure 10, the interior air temperature can be regulated down to -15 °C which allows for a wide range of testing conditions. With air cooling, the cold side of the test surface can be brought down to an approximate minimum of -20 °C. With measured dew points in the range of -7 to -18 °C, the usual relative humidity during experimentation is in the range of 50 to 65%.

Electric fans inside the chamber provide the air with a velocity of around 0.7 m/s. When the fans are not running, a free convection case is assumed. For both cases, the Reynolds numbers based on the hydraulic diameter of the plate are given below. These testing conditions are similar to those typically found in frost growth research, as outlined in Table 3,

$250 < Re_D < 400$	Free Convection (Equivalent)
$2000 < Re_D < 2400$	Forced Convection

3.2.4 Image and data acquisition

The use of a computer and data acquisition system are used to simplify the task of monitoring and recording experimental parameters. An Agilent 34970A data logging system is used with an Agilent 34901A module to measure 18 of the parameters on 30 s intervals, while the mass is determined manually. Acquired data is recorded via the Benchlink Data Logger© software.

The images used for calculation of the physical characteristics of the frost layer (see section 3.3.3) are obtained with the use of high resolution, high magnification digital CCD cameras. The cameras are capable of recording images as well as real time footage of the frost growth process. The front view images are taken with a BigCatch™ DCM510C 5.1 megapixel camera and an Edmund Optics VZM 450i zoom lens. Together the equipment is capable of resolving features on the order of 1 μm with a total magnification of 4.5X. For most of the images, a 2.0X magnification is used with a resolution of 2.61 μm and a measurement of 765 pixels per millimeter.

Images of the frost profile are acquired in a similar manner, using an Edmund Optics model EO-1312M camera and Navitar Zoom 7000 lens. At 6.0X magnification, features on the

order of 15 μm can be resolved with a measurement calibration of 133 px/mm. Refer to Mohs [29] for a more detailed description of this equipment.

3.3 Experimental strategies

Many types of measurements are used in this experiment, ranging from traditional methods to newly proposed techniques based on image acquisition and computer analysis. All of the experimental methodology is described in this section along with the process by which the experiments are performed.

3.3.1 Experimental process

The most important parameters to maintain during the frost growth and defrosting process are related to the chamber environment. It is essential that the interior temperature and humidity remain approximately constant throughout the growth so that the physical characteristics and thermodynamic properties of the frost can be paired with constant growth conditions for analysis. Such a strategy not only greatly simplifies analysis, but also makes it possible to develop correlations for growth.

To enable that approach, the chamber must be brought to a steady state at the desired conditions before any frost growth can take place. Elimination of the transient phase which involves cooling of the chamber air and removing stored energy from the testing assembly and walls means that heat flux removed during frost growth can be quantified accurately into losses and surface flux. The steady state conditions are reached by dehumidifying the chamber air to a temperature below the desired test surface temperature. At the same time, the chamber air is cooled by the circulation fans on the upper heat sink, and the test surface is cooled to its testing temperature.

Once steady state has been reached, which typically takes between thirty minutes to an hour, the experiment can begin. Removed air is then allowed to pass through the circulation pool and the dew point in the chamber rises quickly. Once the dew point is above the test surface temperature, growth begins. The transients associated with this phase are small, since the desired chamber dew point is reached within a short time.

During the growth, which occurs over a period of ~240 min, data is captured at regular intervals of 30 s and images are taken every 5-10 min depending on the desired outputs. The chamber conditions and test surface temperature are moderated so that they remain approximately constant during this time.

Upon conclusion of the frost growth, the thermoelectric modules are disabled. The large temperature gradient between the test surface and outside conditions causes a rapid defrost with no need for applied heat flux. For the duration of the defrosting phase, data is recorded quickly (1 s intervals) and digital footage is recorded.

Following the defrosting phase, the chamber is allowed to reach the ambient external temperature while dehumidification is implemented by replacing the water pool with a desiccant. The process is allowed to continue until the dew point has returned to its initial value (when steady state was reached). At that point, all of the deposited water has been absorbed by the desiccant, so its mass may be determined. The measurement is validated by comparing it to the change in mass of the water pool. Once the follow up dry out phase is completed, the process is complete.

3.3.2 Measurement of interior data

Measurement of airflow

Airflow is not measured within the chamber because testing occurs under free convection conditions. However airflow to and from the chamber through the air humidifier is moderated via adjustable valves. Built into the valves are mechanical flow meters which give real time readings of the volume flow rate. The airflow is adjusted according to chamber dew point as opposed to flow rate. Thus measurement of the airflow serves little purpose here except to estimate possible thermal losses to the environment during transport to and from the humidification chamber. The flow rates of cooling fans (for the main thermoelectric assembly) and circulation fans for air inside the chamber are calculated based on the flow ratings from the fan manufacturers.

Measurement of chamber temperature

The temperature is measured in several locations in the chamber. To obtain the chamber air temperature far from the test surface, which is approximately constant during testing, two type T thermocouples are located around 2.54 cm (1 in.) outward normal from the surface and just above and below its vertical location. The average of these temperatures is taken as an approximate mixing temperature to reduce local measurement error due to convective effects in the chamber.

Measurement of the cold plate temperature is accomplished by the use of type T thermocouples which are placed into the test surface from the side through pre-drilled holes and sealed into place. The temperature is measured in the center of the test surface as well as near a corner so that the uniformity of the temperature distribution across the surface can be analyzed. For the purpose of calculation, the average of these temperatures is used.

The temperatures within the copper spreading block are found in the same way. By the combination of these temperature measurements, the temperature profile throughout the assembly can be examined, and estimates of losses through the chamber wall can then be considered. It is necessary to determine the losses so that the measured heat flux can be corrected to reflect only heat transfer through the frosted surface. The use of a thermocouple on the back side of the chamber wall near the test surface provides information about the thermal resistance, and hence thermal losses from between the test assembly and the outside air.

Thermocouples are also used to monitor the temperatures of the upper cooling surface, as well as the temperatures on both sides of the primary thermoelectric stack. The ambient temperature external to the chamber is also monitored.

Measurement of chamber humidity

The chamber humidity is monitored by a chilled mirror hygrometer, capable of determining dew points within the range of -50 to 90 °C with an accuracy of ± 0.2 °C. The process by which the dew point is measured is illustrated in Figure 10. Air which is extracted for the purpose of humidification is split into two lines at a constant volume flow rate. One of the lines is circulated through a humidification pool, while the other is returned to the test chamber but passes through the hygrometer. It is assumed that heat leakage to the air lines during the extraction process is small so that error between the actual and measured dew points is negligible. Refer to Mohs [29] for an explanation of the functionality of the hygrometer.

Measurement of frost mass

As described in section 3.3.3, the frost mass is determined by weighing both water and desiccant before and after the experiment. The scale used for measurement is a low mass, high accuracy scale which is able to determine mass accurately to within 1 mg.

Determination of convection coefficient

The convection coefficient for heat transfer between the test surface and interior air is an important parameter since it is a required as an input for modeling of the thermal boundary conditions during heating and cooling. The convection coefficient can be obtained by the use of experimental data from the knowledge of heat flux and temperature difference between the cold surface and interior air using Newton's law of cooling,

$$\bar{h} = \frac{q''}{\left(T_c - T_\infty\right)}. \tag{3.1}$$

However, if the heat flux measurement is imprecise as a result of difficulty in estimating thermal losses through the chamber walls to the external environment, the convection coefficient determined by Eq. (3.1) may be unreliable. To help ensure that the calculation is valid (which also implies that the heat flux has been determined correctly), it is useful to compare it to the heat transfer coefficient as predicted by accepted free convection theory. According to Incropera and DeWitt [14], the average Nusselt number for free convection over the surface of a vertical plate is given by Eq (3.2), where m(Pr) is an experimental correlation and is determined by Eq (3.3),

$$\overline{Nu_L} = \frac{\bar{h}L}{k} = \frac{4}{3}\left(\frac{Gr_L}{4}\right)^{1/4} m(Pr), \tag{3.2}$$

$$m(Pr) = \left(0.75Pr^{1/2}\right)\left(0.609 + 1.221Pr^{1/2} + 1.238Pr\right)^{-1/4}. \tag{3.3}$$

The Grashof number, Gr_L is the free convection analogue of the Reynolds number, and can be found using Eq. (3.4), where ΔT is the surface to air temperature difference, and β is the coefficient of thermal expansion,

$$Gr_L = \frac{g\beta(\Delta T)L^3}{\nu^2}. \tag{3.4}$$

The quantities in Eq. (3.4) all depend on the air temperature, and it is convenient to reformulate the equation so that air temperature and wall temperature are the only required inputs over the temperature range of interest. The dynamic viscosity for air can be related to temperature by the general correlation for gas viscosity presented by Fox et al. [9] given in Eq. (3.5), where b and s are experimentally determined constants for the gas of interest. For air, they given by Fox as $b = 1.46 \cdot 10^{-6}$ and s = 110.4, with T in K.

$$\mu = \frac{bT^{3/2}}{s + T}. \tag{3.5}$$

Air can be treated as an ideal gas, and the kinematic viscosity can be found as a function of pressure and temperature by combination of the ideal gas law with Eq. (3.5),

$$\nu = \frac{\mu}{\rho} = \frac{1}{\rho}\frac{bT^{3/2}}{s+T} = \left(\frac{P}{RT}\right)\frac{bT^{3/2}}{s+T}. \tag{3.6}$$

Upon re-arrangement and squaring, Eq. (3.6) can be expressed,

$$\nu^2 = \frac{\left(bR\right)^2 T^5}{P^2\left(s+T\right)^2}. \tag{3.7}$$

By substitution into Eq. (3.4), the Grashof number is,

$$Gr_L = \frac{g\beta P^2 L^3 \left(\Delta T\right)\left(s+T\right)^2}{\left(bR\right)^2 T^5}. \tag{3.8}$$

For an ideal gas the coefficient of thermal expansion is 1/T, and Eq. (3.8) can be finally expressed,

$$Gr_L = \frac{gP^2 L^3 \left(\Delta T\right)\left(s+T\right)^2}{\left(bR\right)^2 T^6}. \tag{3.9}$$

Substitution into of Eq. (3.9) into Eq. (3.2) gives,

$$\bar{h} = \frac{4k}{3L}\left(\frac{gP^2 L^3 \left(\Delta T\right)\left(s+T\right)^2}{4\left(bR\right)^2 T^6}\right)^{1/4} m\left(Pr\right). \tag{3.10}$$

The thermal conductivity of air is related to temperature by a direct curve fit over the temperature range of interest with 99.99% accuracy to tabular data using Eq. (3.11). See **Error! Reference source not found.** for details.

$$k = 1.555\cdot 10^{-4} T^{0.9}. \tag{3.11}$$

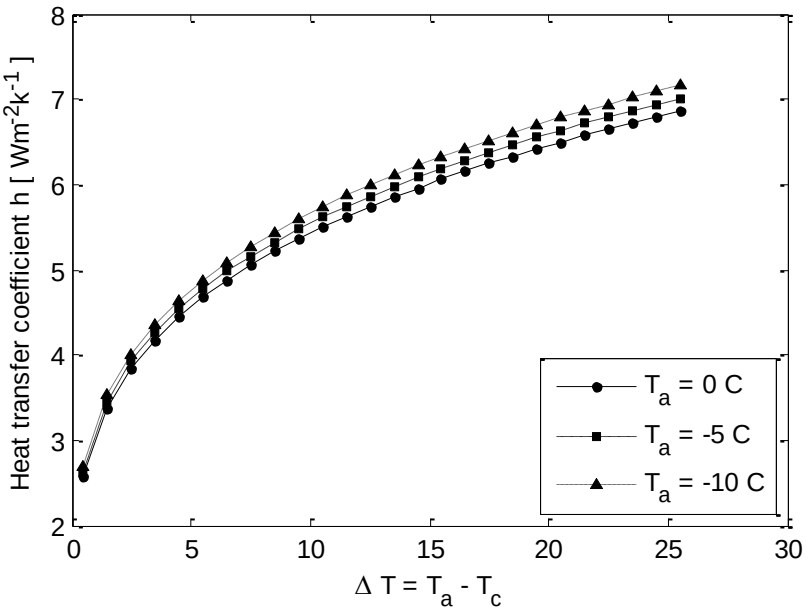

Figure 12. Free convection coefficient determined by air and wall temperatures.

By the use of Eqs. (3.3), (3.10) and (3.11), the free convection coefficient can be calculated for the system knowing only the cold surface temperature, inside air temperature and pressure. Figure 12 shows a plot the resulting convection coefficients for various temperatures within the experimental range of the present study. Based on these results, the convection coefficients are expected to be in the range of 5 to 7 W/m^2K.

3.3.3 Measurement of frost properties

The importance of determining the frost properties is essential for both the purpose of experimental validation and to establish initial conditions for use in defrosting models. The most frequently used measurement techniques have been discussed in general in section 2.2. Here, the methods employed specifically in this experiment are presented for comparison.

Most of the experimental techniques described in this section are original and have been employed for the first time in this research. Their validity is established by comparison to expected results and the results given in the publications described earlier. Furthermore, they are compared to traditional methods in terms of error and reliability in the next section.

With the high powered imaging capabilities now available, unique and more accurate methods are possible for the measurement of items such as frost thickness and porosity, and for the general observation of frost structure at a small scale. The instrumentation used in this

experiment has provided such opportunities, and thus the emphasis in the experimental methods has been placed on the exploration of these new possibilities.

Wherever possible the imaging technology is utilized with a combination of software-based and physical measurements to obtain highly accurate measurements consistently at a very small scale, which is in contrast to traditional visual methods that have employed high powered imaging equipment but have not explored thoroughly the post processing possibilities.

Previously unexplored areas include the automation of measurement to eliminate human error due to subjective placement of rulers and probes (for measuring thickness), and measurement of the maximum, minimum and average frost thicknesses. It is also possible to acquire clearer views of the frost surface profile, determine the porosity and density, and measure average water droplet area and perimeter during defrosting.

Measurement of heat flux through the frost surface

Heat flux measurement has been achieved in the usual way for this experiment, by the use of a thin film heat flux sensor located between the thermoelectric module and the thermal spreader. The heat flux sensor in that arrangement measures a mixture of heat flow, some of which is to or from the test surface, which is the desired quantity. The remainder of the measured heat flux can be attributed to losses through the chamber walls both inside and outside of the chamber. To establish those losses as a function of test surface temperature, the apparatus is operated at a uniform temperature and the heat flux is measured.

Specifically, the test surface and interior air temperature are balanced so that the only heat transfer is through the chamber walls. The measurement of heat flux under such conditions must correspond to the wall losses for corresponding surface temperatures. The calibration data can be found in **Error! Reference source not found.**.

It should be noted that the losses are not only incurred due to the temperature difference between the inside and outside air, but also to the rear side of the thermoelectric module and heat sink. These are also in contact with the test chamber walls, along with the top side thermoelectric cooling system. As a result of these complicating factors an accurate prediction of heat loss based on analytical methods is not possible, and numerical simulations are found to be too sensitive to uncertain parameters such as the conductivity between the test surface components and chamber walls to be of real value (0). The actual heat flux can only be inferred from the apparent losses during calibration and the total data. A future revision of the experiment would include a more accurate method of obtaining the heat flux.

Measurement of frost surface temperature

Originally, the frost surface temperature was to be measured using an infrared thermometer, falling in line with the usual approach. However, the presence of the acrylic walls prevented this option from working correctly. Due to the nature of the experimental apparatus, no other means of measuring this temperature existed without performing of a complete rebuild. Since a rebuild was not a feasible option, the surface temperature was not measured. However, its primary purpose in this experiment is for use in frost correlations to validate visual measurements. For the purpose of validation, it is reasonable to obtain the temperature by calculation or estimation knowing the heat flux, test surface and air temperature because a bounding range of thicknesses can be generated.

Estimation of frost mass

The original experimental design included an electronic scale system wherein the testing apparatus was balanced using a lever arm (to avoid overloading the scale) so that its mass could be measured at any time. The mass of the frost was to be obtained by measuring the changes in total mass over time after calibration using known masses. Owing to the very unstable dynamic system created by the balance, though, it was discovered that the mass could not be measured accurately. Slow and fast oscillations of the balancing arm which were imperceptible to the naked eye meant that it was not possible to obtain reliable readings.

An alternative approach was used to solve the problem. The mass is determined by direct measurement following an experimental run. Instead of measuring the mass of the frost itself, as has been the typical method, the mass of the water supply for the system air is measured before and after the experiment to determine the total amount deposited.

To verify the measurement, the chamber air is evacuated and dried after the defrost cycle using a desiccant over the course of several hours until the interior dew point has reached its original (pre-experiment) level. The change in mass of the desiccant is measured along with that of the water in order to obtain a reliable measurement of the frost mass.

The mass was not measured continuously in this manner, though it could easily be adapted for a future experiment. In that case, the mass of the water container can be monitored during the course of the frosting process, and the results can be verified with the desiccant method following the experiment.

Estimation of frost thickness

Frost thickness is used as one of the primary parameters for experimental validation. Its comparison with results obtained by correlations both reinforce the validity of those correlations

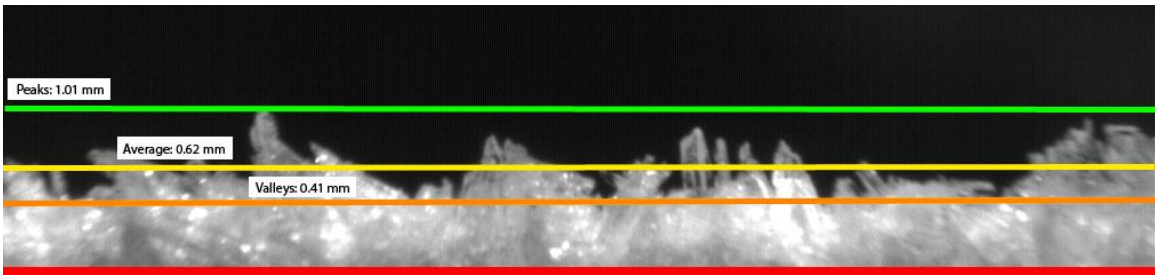

Figure 13. The extreme variation possible when choosing frost thickness measurement locations.

under various conditions and show that optical measurement methods are both reliable and accurate. The measurement of frost thickness in this experiment is accomplished through the use of automated software-based measurement and analysis of digitally acquired images. The correct operation of the code is verified by the manual measurement of frost thickness obtained by the visual method outlined in section 2.2.8.

The measurement of frost thickness can be difficult because the thickness of a frost layer is not rigorously defined in the scientific community at this time. As will be shown later, it is possible to obtain significantly different frost thickness measurements depending upon where one chooses to define the top of the frost layer. Frost thickness can be evaluated based on the location of frost peaks, the apparent average height, or the frost valleys. Current literature does not appear to acknowledge the distinction, which makes it somewhat difficult to compare results. It is therefore most reasonable to determine the thickness by all three possibilities and compare them simultaneously with correlations in order to account for any location choice on the part of the researcher. The sensitivity of the measurement to location is illustrated in Figure 13, which shows that the difference between measurements made in the peaks and valleys is nearly 0.5 mm, a significant variation given the small scale and slow growth of frost layers.

It is most natural to assume that the thickness presented in literature would be the average thickness because it gives the best representation of the overall frost layer behavior. During the initial phase the peak growth is fast, but it slows substantially as the layer becomes denser. The opposite effect is observed in the valleys. Therefore, the average thickness appears to give the most reasonable measurement of growth since it tends to increase regardless of the time.

It is not always possible to make the distinction between heights when taking thickness measurements. Much of the literature has relied on the use of physical based measurements like micrometers or rulers to establish frost thickness. In such cases, the choice of location has little effect because the measurement error of the devices often exceeds the margin of difference due to location choice. Without the ability to resolve the frost structure clearly at a large magnification, it is impossible to choose an exact location. For that reason, correlations and results found in

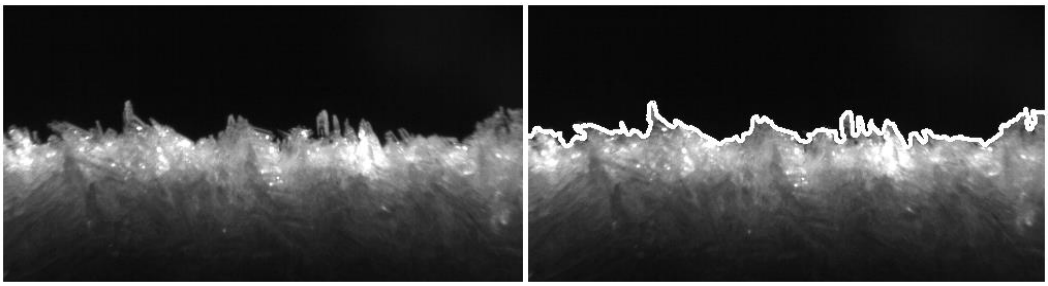

Figure 14. Illustration of frost profile data generated by MATLAB®.

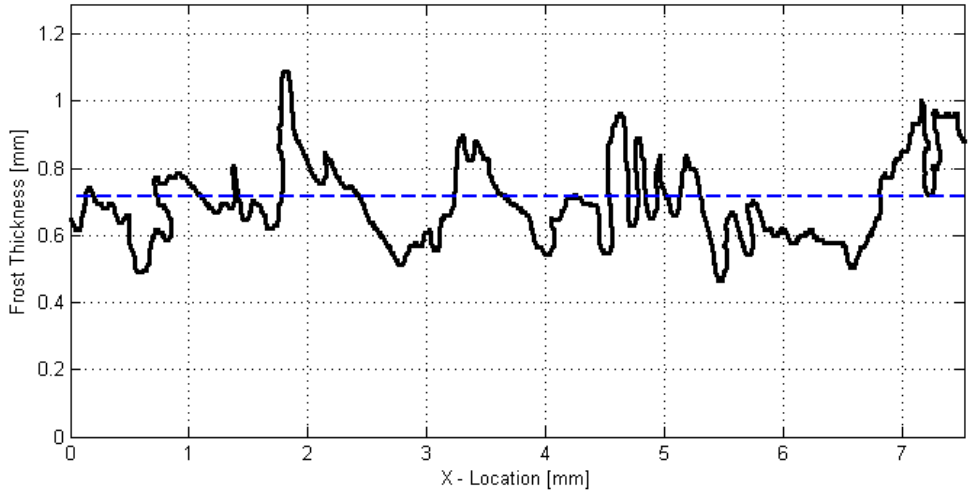

Figure 15. Frost thickness profile after conversion to physical units. Calculated average is shown as the dotted line.

literature could be reporting measurements at any of the levels, or at a mix of them. Even when high resolution image acquisition approach is used, there is error due to subjectivity in estimating locations on the part of the researcher.

All of those factors make the consistent and reliable measurement of frost thickness more complicated than one would immediately imagine. The aim of the method presented here is to eliminate both the human error associated with judging location, to obtain more accurate and consistent results that clearly distinguish the possible different frost thicknesses, and to compare them to those available in literature. The goals can be reached using a software based measurement algorithm that interprets data from high resolution images of the frost profile.

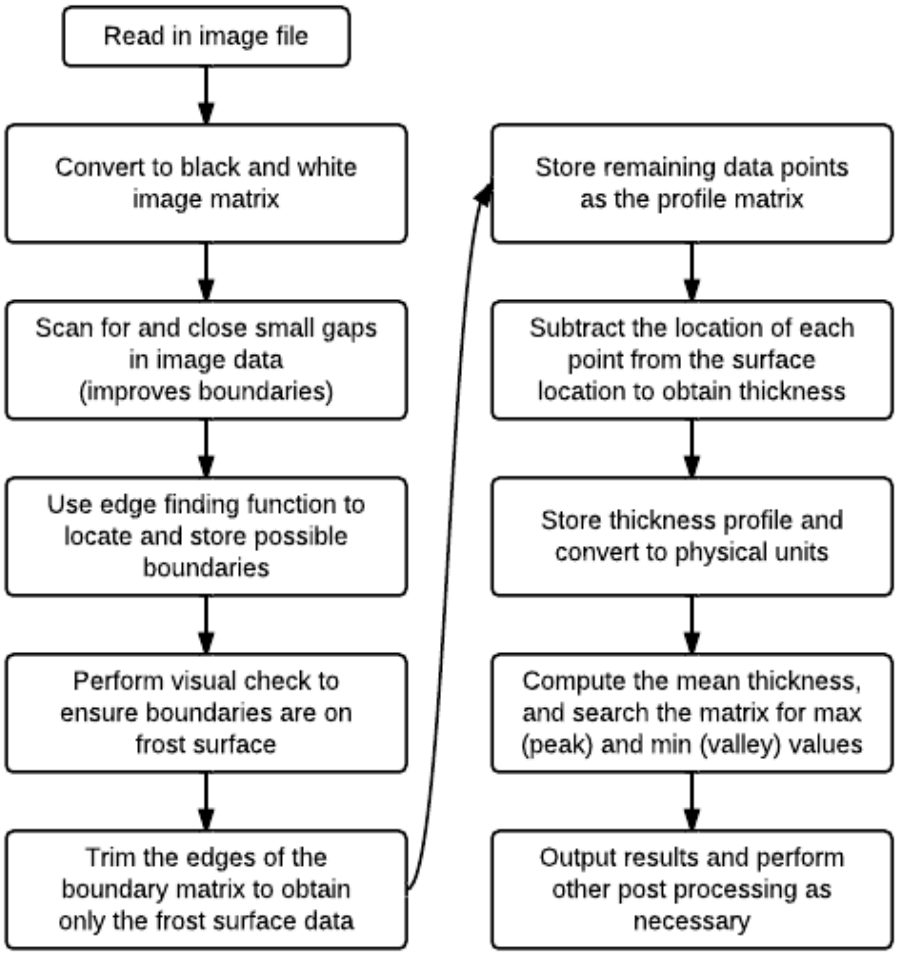

Figure 16. Algorithm for determining frost thicknesses. Performed using MATLAB®.

The basic approach is straightforward. High resolution images are taken at regular intervals at very large magnification so that structural features can be resolved on the order of micrometers. The images are later analyzed by an algorithm designed to measure each of the three thicknesses for each image.

The algorithm first converts the image data into a black and white matrix of a size equal to that of the image resolution. Each matrix value is a measure of relative intensity (or brightness) ranging from 0 as black to 1 for white, while its position within the matrix corresponds to the pixel location on the image.

An edge detection algorithm is then employed to seek out the frost crystal boundaries based on the local contrast (intensity gradient). Those boundaries are stored in a new matrix as a series of values representing the horizontal and vertical position of each counted pixel.

The new matrix is a collection of data points representing the frost surface profile in units of pixels. The result would be the same if one were to measure the distance from the edge of the image to each pixel along the frost surface profile manually and compile them into an array of points giving the horizontal and vertical location of each pixel. The fitment can be verified by superimposing the data points over the image itself, as shown in Figure 14. It is clear that when boundaries are well defined (in terms of contrast), it is possible to obtain very accurate representations of the surface profile.

The frost thickness at each data point can be obtained by measuring the location of the test surface on an image taken prior to frosting and taking the absolute difference between that location and the location of each data point. The thickness obtained by this method has units of pixels, but can be converted into millimeters if the magnification is known. The images presented here are taken at a magnification of 133 px/mm. After the correct thickness has been found for each location it is stored in a new array, from which it is simple to determine the average, maximum and minimum thicknesses for each image.

Figure 15 shows an example plot of this information at an enlarged size for the same frost layer shown in Figure 14. The blue dotted line indicates the calculated average thickness, taken as the numerical mean of the location array. It is clear that by this approach, frost thickness can be calculated consistently and with high accuracy provided the appropriate steps are taken to ensure calibration. The average measurement error in the calculation is around 0.01 mm (or about 0.6%, a marked improvement compared to physical methods (micrometers and rulers) which have been estimated to have overall errors of around 0.1 to 0.3 mm. [4,8,33] The entire process is illustrated in Figure 16 for clarity.

Estimation of droplet size and perimeter

One of the major objectives of frost related research is to improve the understanding of defrosting for the purpose of improved refrigeration systems. A major issue encountered during the typical defrosting process is the problem of eliminating water droplets after the melt phase is complete. The majority of the frost layer usually slumps (slides due to gravity) off of exchanger surfaces once a thin water film has been created at the frost-metal interface. However, water droplets are frequently left behind due to surface tension effects. In areas not conducive to slumping (e.g., horizontal surfaces), larger pools of water may also remain.

Given enough defrosting time remaining droplets will evaporate, leaving the surface dry (as desired) before the next cooling process is initiated. The downside to this is that because a significant portion of the frost is removed quickly due to slumping, much of the energy expended

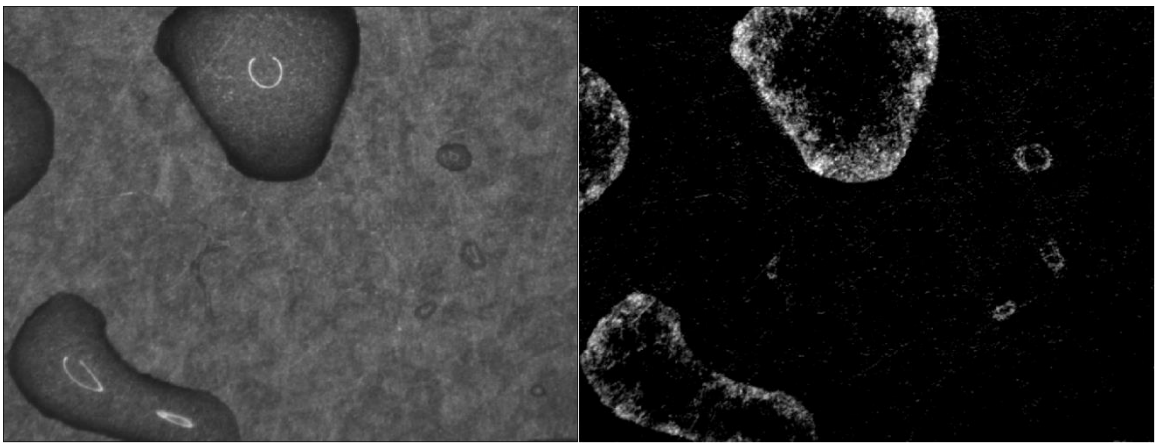

Figure 17. Result of base image subtraction from droplet matrix.

during the evaporation process is lost into the cold environment, which is counterproductive and impacts overall system efficiency. In fact, the fraction of lost heating energy is so large that most industrial defrosting processes are stopped early after slumping has occurred. The remaining water is left on the surface and re-freezes with the next cooling cycle.

As cycling continues, the amount of total water present at the start of a given cooling cycle tends to increase. When the water re-freezes, it disrupts airflow and provides more nucleation sites for air moisture. The end result is that defrosting cycles become more and more frequent and system performance drops continuously until the system can be completely dried.

Thus the behavior of the remaining water during evaporation is of interest when investigating defrosting performance. That behavior is observed and measured in this experiment by a new approach based upon image acquisition and computer based measurements, similar to that used for determining frost thickness. The quantities of interest are the droplet area and perimeter which are used in determining average droplet volume at any given time.

It is possible as with the case of thickness to ascertain those values by physical (or virtual) measurements applied to front view images of the surface during evaporation if the total magnification and resolution are known. Owing to the irregular shape of some drops, it may be difficult to measure area by this approach. Furthermore, the task of doing so for each droplet on every image over a time series is highly time-consuming. A faster and more accurate approach is to use computer software to perform the same task and compile the results.

The algorithm used for calculating droplet related data is based off the algorithm originally created for finding the frost layer thickness. It begins with the acquisition of a series of images throughout the evaporation process. Images are taken from a view normal to the test surface and at high resolution and contrast so that droplet boundaries are well-defined.

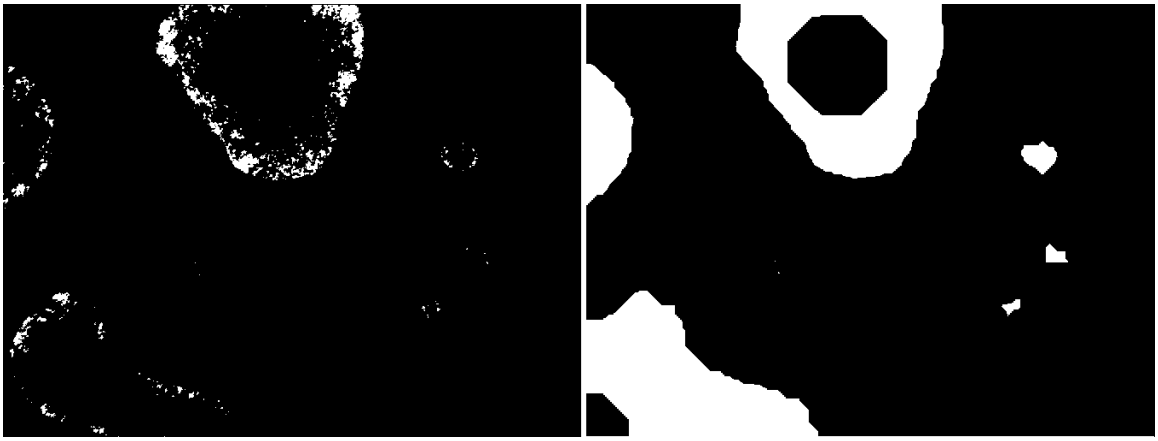

Figure 18. Closing boundaries after black and white conversion.

Different magnifications can be used, but if the averages are calculated and a per droplet basis then significant jumps may occur in the computed values at very high magnifications when one or more of only a few droplets disappears. The interpretation of this effect is similar to the notion of continuum, wherein at lower magnifications the changes in averages are gradual due to the larger number of droplets present in the image.

The images are read into the computer one at a time and converted to a grayscale format for adjustment. They are then adjusted automatically to improve contrast so that droplet edges are enhanced. To further reduce noise due to roughness on the test surface, the procedure is repeated for an image of the same area of the test surface with no droplets present. At that point, two image matrices exist that store values ranging from 0 to 255 for each pixel: one for the dry (base) image, and one for the image containing droplets for analysis. By performing an element-wise subtraction of the matrices the noise resulting from test surface roughness is cancelled out of the image matrix containing the droplets leaving an image matrix that is black in all areas besides the droplets. An illustration of the conversion is given in Figure 17. It is clear that by this approach the droplets may be easily identified and their boundaries clearly defined.

After the subtraction process, some noise remains because of slight differences in the images. Two subsequent steps are taken to eliminate this noise and fully define the droplet areas. The first of these is a conversion from grayscale to black and white. Since the remaining noise is generally of low intensity (i.e., values near zero in the image matrix), most of it is eliminated during this conversion, leaving an image matrix of ones and zeroes that is zero everywhere except on droplet areas. More work is required because many of the droplet data points are also of low intensity and are thus set to zero.

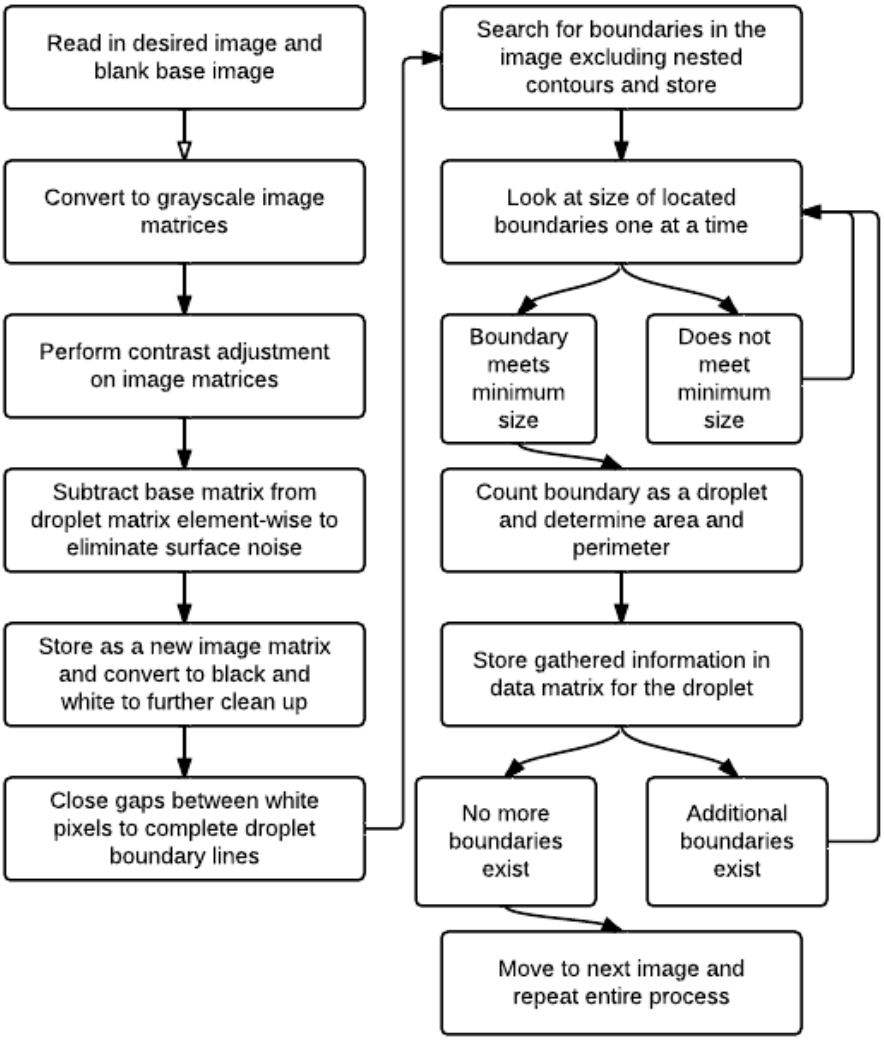

Figure 19. Algorithm for determining droplet properties.

The image matrix at this point consists of a series of white dots scattered along the droplet boundaries and within the droplets themselves (see left side of Figure 18). The final step required to prepare the image for analysis is a boundary closure algorithm, which fills in the gaps between pixels separated by a user-specified distance. The result of is the image on the right side of Figure 18, where the droplets are clear and continuously defined in the matrix. The fact that some of the drops may end up with black centers is unimportant because when boundaries are traced nested boundaries can be ignored.

Boundaries are traced on the image matrix excluding holes (or "nested boundaries") and the results are stored as a compilation of horizontal and vertical points indicating boundary locations as with the frost thickness algorithm. Each boundary is stored as a separate array of points during this step so that each array represents one droplet. All boundaries are closed

contours, and therefore the droplet area can be found for each of the arrays by numerically integrating along the boundary array.

The droplet perimeter for each droplet is found in a similar way. Since the minimum unit of length is one pixel, the length in pixels of a curved segment along the droplet boundary can be determined numerically by stepping through each pixel and computing the change in horizontal and vertical position. The computation is performed as in Eq. (3.12), where N is the total number of data points in the array.

$$p \approx \sum_{i=1}^{N} \sqrt{\left(\Delta x_i\right)^2 + \left(\Delta y_i\right)^2}. \tag{3.12}$$

Once the areas and perimeters of all droplets are known, the averages can be calculated on a per-droplet or per-image area basis. The latter is convenient for finding the average area fraction of the surface covered by water at any given time, whereas the former can be useful for investigating average droplet behavior directly. The perimeters and areas can also be converted into physical units if the magnification level is known.

The entire procedure is repeated for each image in the series, and the results from each image are compiled into a three dimensional structure. The structure (also called a "cell") contains the results for each individual droplet and the total and average results for each image,. Thus all data corresponding to any droplet on any image is available following the analysis along with the elapsed for each image and provides a full picture of the droplet behavior during the evaporation phase, upon which further conclusions and analysis can be based.

Estimation of frost porosity and density

The porosity of frost is a necessary parameter to acquire. The thermodynamic properties of frost are highly dependent on the porosity, which is the ratio of voids to total space in a porous medium. The porosity of a layer of frost may vary depending on the ambient conditions and the physical conditions of the frost formation. The interaction of ice crystals inside the layer governs the diffusive behavior of thermal energy through it, and therefore properties such as thermal conductivity and specific heat can be predicted if the porosity is known. Furthermore the porosity provides a means of estimating the frost layer density based on an external measurement of thickness. The value of the porosity thus is two-fold. First it may serve as a basis for correlating the frost properties themselves, and secondly it can be used to verify the same results obtained by other means. For example, it can be used to verify the density by means of comparison with a mass measurement.

The actual formation of frost crystals cannot be predicted accurately by either analytical or empirical models, and thus the porosity is most easily obtained by measurement. In this experiment a photographic technique is employed to determine frost porosity at any given time. The porosity of a mass of frost may be defined by,

$$\varepsilon_a = \frac{V_{voids}}{V_{total}}. \tag{3.13}$$

If the porosity is assumed to be constant throughout the frost layer, Eq. (3.13) can be reduced to an area fraction because the ratio of empty to total area anywhere throughout the height of the layer would be equal to the equivalent volume fraction of the total layer. So the porosity used here is defined by,

$$\varepsilon_a = \frac{A_{voids}}{A_{total}}. \tag{3.14}$$

Equation (3.14) can be rewritten in terms of air and ice, where the porosity subtracted from the total area ratio (equal to 1) can be used to distinguish the two,

$$\varepsilon_a = \frac{A_{air}}{A_{total}} = 1 - \frac{A_{ice}}{A_{total}}. \tag{3.15}$$

Equation (3.15) can be used to relate physical properties that depend on frost density to the porosity because porosity can be viewed as a dimensionless form of density. If the ratio of areas on the frost surface can be determined accurately, those properties may be calculated thereafter if they are known for pure ice and air. As an example, frost layer density can be found by taking the sum of partial densities based on area fraction given by Eq. (3.16). The approximation works when the volume ratio of solid to air is large. For smaller ratios the air properties play an increasingly significant role which must be accounted for, and the effects of crystal structure become very important (see section 2.3.2).

$$\rho_f = \frac{A_{air}}{A_{total}}\rho_a + \frac{A_{ice}}{A_{total}}\rho_i = \varepsilon_a\rho_a + (1-\varepsilon_a)\rho_i. \tag{3.16}$$

Similarly, for thermal conductivity and specific heat,

$$k_f = \varepsilon_a k_a + (1 - \varepsilon_a) k_i. \tag{3.17}$$

$$C_{Pf} = \varepsilon_a C_{Pa} + (1 - \varepsilon_a) C_{Pi}. \tag{3.18}$$

Equations (3.16) to (3.18) can be used to determine the thermodynamic properties of the frost layer based on measurements of the porosity. These relationships can then be compared to correlations based on ambient conditions and validated by experimental measurements. It should be noted that while Eq. (3.18) is reasonable, Eq. (3.17) predicts a thermal conductivity which is non-directional. In other words, it carries with it the implicit assumption that the frost layer is a homogenous medium composed of air and ice. In reality the conductivity of the layer is heavily influenced by the crystal orientation. Thus, Eq. (3.17) tends to predict the thermal conductivity incorrectly. To reduce that error the equation can be modified to account for some variation based on probable crystal structure. One such approach is that presented by LeGall et al. [20], and is outlined in section 2.3.2.

The photographic technique used to determine frost porosity is based on Eq. (3.15) and the reflectance of light on the frost surface. When incident light strikes a void on the surface of the frost, the ray is reflected differently than it is for a relatively flat area. The voids show up as darker areas on a photograph of a frosted surface. If the resolution of the camera is sufficient, these areas can be identified, counted, and compared to the total area of the image, giving a reasonable estimate of porosity. It follows that the higher the resolution of the camera, the more accuracy can be achieved because finer distinctions between voids and solid areas can be made. The camera used in this experiment is capable of obtaining extremely high resolution photographs on the scale of tenths of a millimeter making it ideal for this type of technique.

Counting light and dark areas manually becomes an exceedingly long procedure as the number of pixels (and thus accuracy) is increased. To take full advantage of the capability of the camera, a computer algorithm (to be described shortly) was written to count the pixels and calculate the porosity, density, thermal conductivity, specific heat and mass of the frost layer.

To validate the assumption that the porosity is constant throughout the frost layer, images can be collected periodically and their calculated porosities can be compared. If the images are taken frequently, a reasonable series should be generated corresponding to the development of the frost layer over time and thickness. By observing this evolution, conclusions can be drawn about the uniformity of the frost layer's properties.

The algorithm is straightforward. High resolution, close up images of the frost surface are taken over time. These images are converted to grayscale matrices. The conversion to grayscale serves two purposes. First, the amount of data that must be interpreted as void or solid is simplified from a three dimensional array to a two dimensional matrix of values ranging from 0 to 255, which represent white or black respectively. The intermediate values are a simple linear grayscale between the two. The second function of the conversion is that it provides a situation where objective determination of space or solid is more easily implemented. Instead of developing a complex set of rules, a simple numerical value between 0 and 255 can be assigned as a criterion, which represents the average brightness of a void. Pixels meeting the criteria are counted as voids, and others are not. The correct average value can be determined by making experimental measurements to find the actual porosity and iteratively adjusting the algorithm to match it for each case. The result will be a distribution of averages, which will not only yield the most likely value of porosity for a frost layer but also the statistical uncertainty associated with that choice. More complex algorithms that use several average values may be able to improve the estimates. Once the porosity has been established, the computation of the frost properties as described above is a simple matter.

The algorithm uses Eq. (3.15) modified for use in images. The approximation made is that each pixel may be counted as void or solid. The area ratio of voids to solid is simply the numerical ratio of pixels assigned void to the total number of pixels,

$$\varepsilon_a = \frac{N_{void}}{N_{total}}, \tag{3.19}$$

where N is the number of pixels counted for each case. An alternative algorithm was also investigated, wherein the grayscale matrix is converted to black and white so that each pixel automatically represents a void or not. Then the total sum of the values in matrix should equal the area fraction of ice. Dividing by the total number of pixels in the image then gives the porosity in terms of ice, so that the air porosity can be found with Eq. (3.15).

The second method does not yield the same results, but gets rid of the need for determining an average pixel value as a void criterion. Instead the method relies on the intensity scaling of the image. If all images are illuminated equally, then the black and white conversion factor need only be determined for a single image based on calibration and may then be applied to all of the images. The conversion factor is a numerical value of intensity between zero and one that determines whether a gray pixel is counted as black or white. As such, it is analogous to the

previous method of counting pixels individually but is faster and simpler. It has been shown by Mohs [29] that this approach tends to yield more reliable results than the individual count method based on a grayscale matrix.

3.4 Comparison of experimental methods

Listed in Table 8 are the equivalent experimental parameters which were used to obtain data in some of the studies most similar to the one described here. The major differences in are the chamber dimensions, experimental conditions and thickness measurement techniques. Thus, it is clear that the current setup falls within approximately the same parameters of typical frost growth experiments, implying that data recorded should be comparable to that obtained by others.

Table 8. Comparison of experimental setup to those of similar studies.

Authors	**Current Experiment**	**Yamashita, Hamada, Ise, Ohkubo [36]**	**Iragorry, Tao [15]**	**Fossa, Tanda [8]**	**Hao, Iragorry, Tao, Castro [12]**
Year	2011	2007	2004	2001	2005
Experimental Design					
Enclosure	Cold chamber (0.1x0.05x0.2 m)	Air duct (0.04x0.04x0.1 m)	Cold chamber (2x2x2.5 m)	Open chamber (0.2x3.6x2.4 m)	Lab environment
Convection	Free	Forced	Forced	Free	Free
Orientation	Vertical	Vertical	Vertical	Vertical	Horizontal
Test Surface Design					
Geometry	Flat Plate	Flat plate	Finned plate	Flat plate	Flat plate
Material	5052 Aluminum	1050 Aluminum	Aluminum	Copper	Aluminum
Size [mm]	38 x 38 x 3.88	60 x 60 x 1	40 x 40 x 3.8	95 x 282	40 x 40 x 1.6
Cooling Method	Thermoelectric w/air cooling	Thermoelectric w/brine cooler	Thermoelectric w/glycol	Flat surface w/ glycol	Thermoelectric w/ 70% gylcol
Measurements					
Interface Temperature	NA	3 radiation TC's	Infrared thermometer	2 T type TC's on micrometer	Holographic Interferometry
Test Surface Temperature	2 embedded T type TC's	Embedded T type TC	Embedded T type TC	5 Embedded T type TC's	4 Embedded TC's
Air Temperature	2 T type TC's near surface	T type TC's in airstream	T type TC's in airstream	Fine gauge TC's in airstream	2 TC's above test surface
Heat Flux	HFS-4 thin film sensor	Heat flux sensor	HFS-3 heat flux sensor	3 Heat flux sensors	NA
Air Velocity	NA	Hot wire anemometer	NA	NA	NA
Relative Humidity	Hygrometer	Hygrometer	NA	Capacitance hygrometers	Hygrometer
Frost Mass	Water and desiccant mass changes	Scraped onto electronic scale	Removable fins / scale	Scraped onto scale	NA
Frost Thickness	Computer based analysis	Visual via imaging system	Visual via imaging system	Micrometers and electrodes	Visual via imaging system
Experimental Conditions					
Surface Temp Range [°C]	0 to -20	-10 to -30	-20 to -26	-4 to -13	-18 to -30
Air Temp. Range [°C]	0 to -15	0 to -20	-15 to -20	26 to 28	23
Relative Humidity [%]	50 to 65	52 to 72		31 to 58	41 to 68
Air Vel. [m/s]	0.7	0.5	3.3 to 10	NA	NA
Reynolds #	250 to 400	NA	1400 to 4500	NA	NA

Table 9. Measurement error of experimental quantities.

Measurement	Type	Error
Temperature	T-type TC	±0.5 C
Dew Point	Hygrometer	±0.2 C
Mass	Electric scale	±3 mg
Heat Flux	Thin film HFS	±0.5 %
Pressure	Transducer	±0.05 %
Length	Image acq.	±15 μm

3.5 Error of measured quantities

There is inevitably uncertainty associated with the measurement of experimental quantities. The effect of this error is reflected not only in the values of the quantities themselves, but also in any calculation based upon those values. The propagation of error can have large impacts on calculated quantities if the measurement errors are large. The error associated with measurement and the resulting uncertainty in calculations is outlined here. There are five important quantities which are measured during the frost growth process, that are used directly and indirectly to obtain the desired outputs. These are listed in Table 9 along with their respective measurement errors.

Based on measurement error, the absolute uncertainty in each of the calculated quantities can be obtained in the usual way, as per Eq. (3.20). The function f represents the quantity of interest, x_i are the dependent variables satisfying the relationship $f = f(x_i)$, and Δx_i is the measurement error associated with each variable.

$$\Delta f = \sqrt{\sum_{i=1}^{N} \left| \frac{\partial f}{\partial x_i} \right|^2 \cdot \Delta x_i^{\,2}}. \tag{3.20}$$

3.6 Uncertainty associated with primary parameters

Since the validation of the experimental results is dependent on the accuracy of the primary measurements outlined in Table 9, it is necessary to quantify the associated uncertainty. This is especially true for the case of image based measurements performed by the computer, since they are to be compared with traditional methods.

Estimating the uncertainty associated with visual measurements and digital calculations can be difficult since it depends on the algorithms used to convert image matrices into physical measurements. Several ideas are proposed here for the estimation of the uncertainty of frost porosity, thickness and droplet perimeter as calculated in section 3.3.3.

Porosity

The porosity is an important value for the determination of the frost properties. As demonstrated in section 3.3.3, it is used to determine density, specific heat and thermal conductivity. Recalling Eq. (3.19), porosity is calculated as the ratio of pixels counted as voids divided by the total number of pixels,

$$\varepsilon = \frac{N_{void}}{N_{total}}, \tag{3.19}$$

where the number of pixels counted as voids are determined by the conversion criterion. The conversion criterion, as described in section 3.3.3, is a numerical value which is either between 0 and 255 for a grayscale image matrix or 0 and 1 for a black and white matrix. A value in the matrix is counted as a void pixel if it is smaller than the conversion criterion, i.e., if it is a dark area on the image it is counted as a void pixel.

To evaluate the uncertainty of ε in Eq. (3.19) by the use of Eq. (3.20), it is necessary to determine the variance in N_{void} and N_{total}, which are denoted from here on as N_V and N_T, respectively. The total number of pixels N_T for an image has a zero variance because it is a fixed value determined by the imaging equipment. However, the number of pixels counted as voids depends on the chosen conversion value. Direct application of Eq. (3.20) yields,

$$\Delta\varepsilon = \sqrt{\left|\frac{\partial\varepsilon}{\partial N_T}\right|^2 \Delta N_V{}^2} = \sqrt{\frac{1}{N_T{}^2}\Delta N_V{}^2} = \frac{\Delta N_V}{N_T}. \tag{3.21}$$

The variance ΔN_V must be determined before Eq. (3.21) can be evaluated. However, it is difficult to speculate on this error directly because knowledge of the relationship between N_V and the conversion value is needed. Although that relationship depends ultimately on the image itself, it is theorized here that it will be similar between similar images of the frost surface so that the average uncertainty of ε for all images is approximately the same. The relationship depends only on the conversion value, denoted as σ. The value of σ for a gray to black and white conversion varies between 0 and 1, it is reasonable to assume the following proportionality,

$$N_v \propto \sigma N_T, \tag{3.22}$$

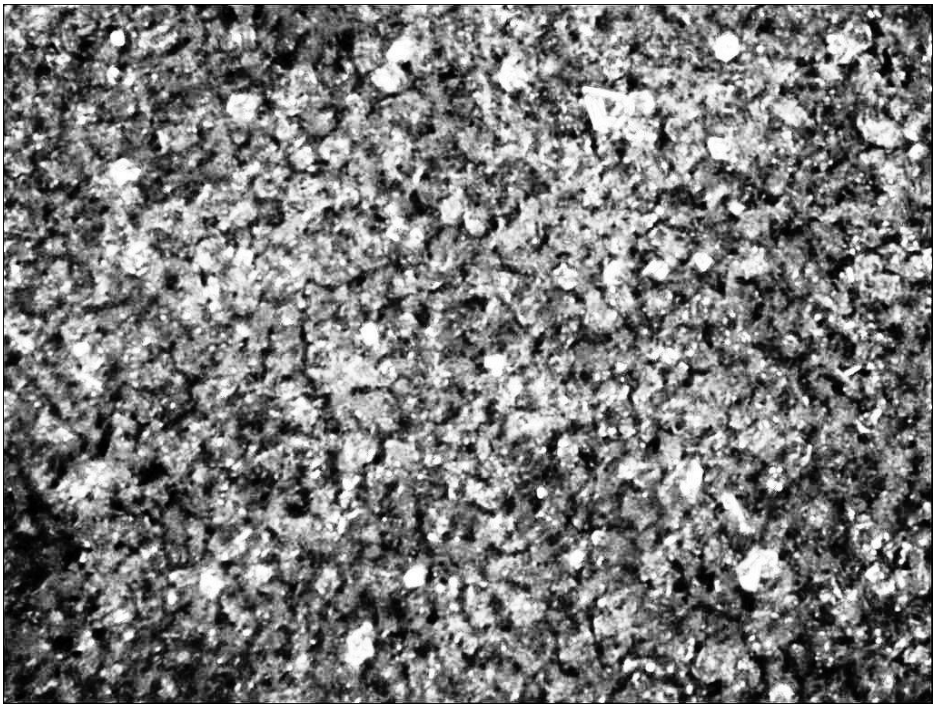

Figure 20. Front image of frost surface used for finding porosity.

so that $N_V = N_T$ if $\sigma = 1$ and $N_V = 0$ if $\sigma = 0$.

To examine the actual relationship, consider Figure 20, which is a typical front view of the frost layer surface. Based on the image, it appears that the distribution of intensity varies somewhat uniformly black and white. As a result, it is proposed that the relationship between the number of voids counted and the conversion value is approximately linear. In other words Eq. (3.22) should be a linear relationship of the form,

$$N_v = \kappa\sigma N_T, \tag{3.23}$$

where κ is the slope. Following Eq. (3.20) again, the variance ΔN_V can be found assuming that κ and N_T are fixed,

$$\Delta N_V = \sqrt{\left|\frac{\partial N_V}{\partial \sigma}\right|^2 \Delta\sigma^2} = \sqrt{\left(\kappa N_T \Delta\sigma\right)^2} = \kappa N_T \Delta\sigma. \tag{3.24}$$

Substituting (3.24) into (3.21) gives the uncertainty of ε in terms of the variance $\Delta\sigma$,

$$\Delta\varepsilon = \kappa\Delta\sigma. \tag{3.25}$$

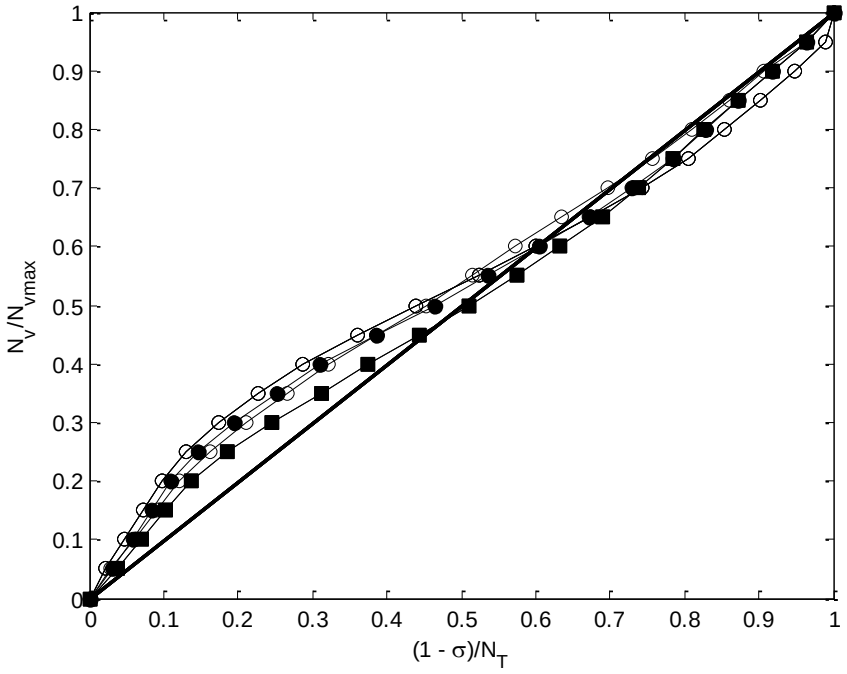

Figure 21. Variation of N_V with the conversion value.

Thus, the uncertainty of ε is directly related to the error in choosing σ. It is easier to speculate on this error than on $\Delta\varepsilon$ or ΔN_V because it is both on a scale of 0 to 1 and is based on the average image intensity.

To determine the constant κ, Eq. (3.23) is plotted (with reversed slope) for several images. Typical results are shown in Figure 21. It is clear that the assumption of a linear variation is in reasonable agreement with results. Furthermore the slope of the lines indicates that $\kappa \approx -1$, meaning that the uncertainty of ε can be written,

$$\Delta\varepsilon = \pm\Delta\sigma. \tag{3.26}$$

Equation (3.26) is an intuitive result. Nevertheless it is important to make the connection through Eqs. (3.21) to (3.26) in order to estimate the magnitude of the uncertainty. The conversion value σ varies on a range of 0 to 1, and is typically calculated as the average image intensity. However, there is some error ($\Delta\sigma$) even when σ is calibrated to a specific image by iteration and comparison to the porosity as determined by physical mass and volume measurements. The error is inherent to the technique because of the discretized nature of a digital image. The final step is to estimate the error $\Delta\sigma$, which is determined by experimental observation. Here, it is estimated to be ~0.1.

Thickness

The frost thickness is determined by taking pixel measurements of distance and converting them into lengths, as outlined in section 3.3.3. Results show that the method has the potential to increase the accuracy of frost thickness measurement by an order of magnitude over the traditional physical methods. It is important to analyze the uncertainty that arises in converting the digital image into useable data for thickness measurements to verify that claim. The conversion is made by Eq. (3.27), where the subscripts indicate the units of thickness and Γ is the resolution ratio in pixels per millimeter,

$$\delta_{mm} = \frac{\delta_{px}}{\Gamma}. \tag{3.27}$$

The uncertainty in δ_{mm} is,

$$\Delta\delta_{mm} = \sqrt{\left|\frac{\partial\delta_{mm}}{\partial\delta_{px}}\right|^2 \Delta\delta_{px}{}^2 + \left|\frac{\partial\delta_{mm}}{\partial\Gamma}\right|^2 \Delta\Gamma^2}. \tag{3.28}$$

It is argued that the error associated with δ_{px} is ±1 px because the thickness at each point is rounded to the nearest pixel by the computer. Thus $\Delta\delta_{px} = 1$. The error $\Delta\Gamma$ is due to mis-calibration of the imaging equipment (i.e., a slightly angled viewing plane, skewing near the edges of the lens, slight position changes, etc.). Depending on how the equipment is calibrated to determine Γ the error may be mostly eliminated, but it is included in this analysis to account for the possibility of its existence. Evaluating Eq. (3.28) for $\Delta\delta_{px} = 1$ gives,

$$\Delta\delta_{mm} = \sqrt{\frac{1}{\Gamma^2} + \frac{\left(\delta_{px}\Delta\Gamma\right)^2}{\Gamma^4}} = \frac{1}{\Gamma}\sqrt{1 + \left(\frac{\delta_{px}\Delta\Gamma}{\Gamma}\right)^2}. \tag{3.29}$$

Thus the uncertainty in the thickness measurement $\Delta\delta_{mm}$ depends on both the error in scaling and the thickness itself. Because the uncertainty varies as a function of thickness, it is most convenient to express an average uncertainty which will occur over the range of interest. The average thickness error is determined by integration of Eq. (3.29) up to the maximum expected thickness as is shown in Eq. (3.30).

$$\overline{\Delta\delta}_{mm} = \frac{1}{\delta_{max}} \int_{\delta_{px}=0}^{\delta_{max}} \frac{1}{\Gamma} \sqrt{1 + \left(\frac{\delta_{px} \Delta\Gamma}{\Gamma} \right)^2} \, d\delta_{px}. \tag{3.30}$$

Evaluation of the integral is omitted here, but results in Eq. (3.31),

$$\overline{\Delta\delta}_{mm} = \frac{1}{2\Gamma} \sqrt{1 + \left(\frac{\delta_{max} \Delta\Gamma}{\Gamma} \right)^2} + \frac{\sinh^{-1}\left(\frac{\delta_{max} \Delta\Gamma}{\Gamma} \right)}{2\delta_{max} \Delta\Gamma}. \tag{3.31}$$

It is convenient to express the maximum encountered thickness as a multiple of the resolution ratio Γ, so that units of mm can be inserted directly into Eq. (3.31). Denoting the maximum expected thickness in mm as a constant δ_M then by Eq. (3.27) it follows that $\delta_{max} = \Gamma\delta_M$. Insertion of this relationship into Eq. (3.31) gives Eq. (3.32), which can be used to estimate the average thickness error knowing the maximum thickness in mm and the possible scaling error.

$$\overline{\Delta\delta}_{mm} = \frac{1}{2\Gamma} \left(\delta_M \Delta\Gamma + 1 \right)^{1/2} + \frac{\sinh^{-1}\left(\delta_M \Delta\Gamma \right)}{2\delta_M \Gamma \Delta\Gamma}. \tag{3.32}$$

In the case where the scaling error is not present then the total error is,

$$\underset{\Delta\Gamma=0}{\Delta\delta_{mm}} = \frac{1}{\Gamma}. \tag{3.33}$$

As with the case of porosity, the actual error ΔΓ is difficult to estimate. However various values can be chosen for the purpose of illustration. The actual value depends on the calibration method used for the equipment. These results are shown in Figures 22 and 23, for varying uncertainties in ΔΓ and different values of Γ. It is clear that even for reasonably large errors of ±8 px/mm the overall error is on the order of ±0.1 mm, lower than that of many traditional techniques. If a higher resolution and magnification are used the associated error drops greatly as evidenced in Figure 23. With good calibration, it is easily possible to reach accuracies in the range of ±0.01 mm, which is a great improvement over that of previous methods.

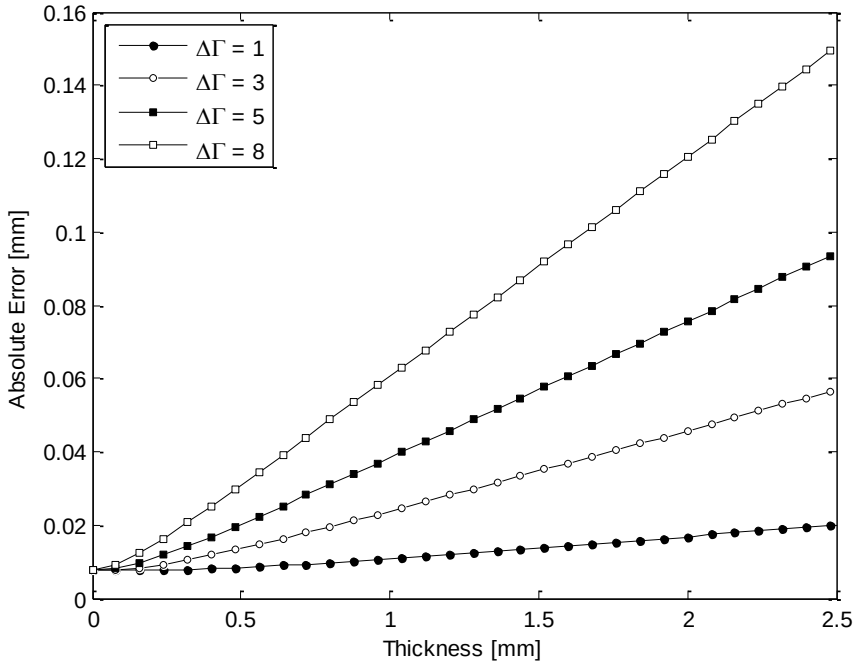

Figure 22. Absolute thickness measurement error based on calibration uncertainty. $\Gamma = 133$ px/mm.

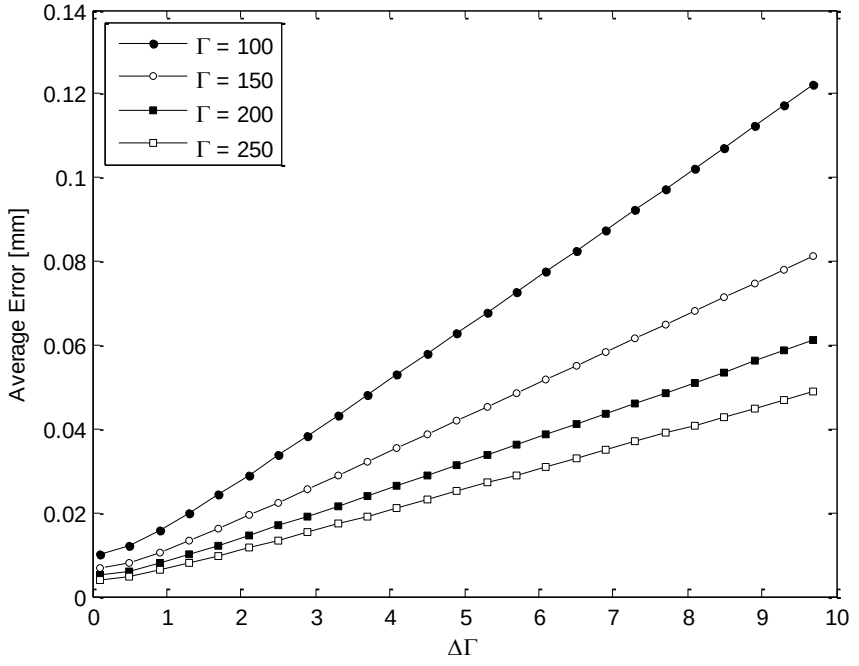

Figure 23. Average thickness measurement error for different scaling and calibration.

Droplet perimeter

Average and total drop perimeter is determined by an edge finding algorithm that attempts to locate edges based on intensity gradients and calculate their length in pixels. To close the boundaries it is occasionally necessary to interpolate between points. Furthermore, to capture all of the desired boundaries it is sometimes also necessary to adjust the parameters used by the algorithm to locate them. Introducing so many variables creates the potential for significant amounts of uncertainty. It is recommended that the method be calibrated by testing and comparison to the actual images before it is taken as accurate.

The uncertainty associated with the perimeter calculations is found in a similar way to that of the thickness because it is another length scale. The major difference is that there may be a variance of more than one pixel at each point, since it is difficult to determine exactly where a boundary is. Furthermore, this error is propagated because the location of all points must be used to determine the perimeter, and the uncertainty exists at all points. The distance in pixels between two points counted as boundary points is approximated by a linear interpolation according to Eq. (3.34). The total perimeter is the sum of each interpolation,

$$p_i \approx \sqrt{(x_i)^2 + (y_i)^2}. \tag{3.34}$$

To determine the error in p_i, Eq. (3.20) is applied which gives,

$$\Delta p_i = \sqrt{\left|\frac{\partial p_i}{\partial x_i}\right|^2 \Delta x_i^{\,2} + \left|\frac{\partial p_i}{\partial y_i}\right|^2 \Delta y_i^{\,2}}. \tag{3.35}$$

Taking the derivatives and simplifying gives,

$$\Delta p_i = \sqrt{\frac{(x_i \Delta x_i)^2 + (y_i \Delta y_i)^2}{x_i^{\,2} + y_i^{\,2}}}. \tag{3.36}$$

It is assumed here that the error associated with each point is about the same in both x and y. Thus for all i, $\Delta x_i = \Delta y_i = \Delta L$, and Eq. (3.36) reduces to,

$$\Delta p_i = \sqrt{\frac{\Delta L^2 \left(x_i + y_i\right)^2}{x_i^{\,2} + y_i^{\,2}}} = \Delta L. \tag{3.37}$$

It is this possible to determine the error in the total perimeter of a drop in terms of pixels by finding the error of the sum of Δp_i. The total perimeter is given by Eq. (3.38), where N represents the total number of points counted in the perimeter (the matrix length),

$$p = p_1 + p_2 + \ldots p_N = \sum_{i=1}^{N} p_i. \tag{3.38}$$

Direct application of the uncertainty formula yields,

$$\Delta p = \sqrt{\left|\frac{\partial P}{\partial P_1}\right|^2 \Delta p_1^{\,2} + \left|\frac{\partial p}{\partial p_2}\right|^2 \Delta p_2^{\,2} + \ldots \left|\frac{\partial p}{\partial p_N}\right|^2 \Delta p_N^{\,2}} = \sqrt{\sum_{i=1}^{N} \left|\frac{\partial p}{\partial p_i}\right|^2 \Delta p_i^{\,2}}. \tag{3.39}$$

Because the derivative is equal to unity for all i, Eq. (3.39) reduces to,

$$\Delta p = \sqrt{\sum_{i=1}^{N} \Delta p_i^{\,2}} = \sqrt{N \Delta L^2} = \Delta L \sqrt{N}. \tag{3.40}$$

Once the error Δp is known then the total error after conversion from pixels to millimeters can be determined in the same way as for thickness, the only difference being that the pixel error is now Δp rather than unity. Equation (3.41) illustrates the similarity of the procedures. The repetition of the derivation is omitted but leads to the Eq. (3.42).

$$p_{mm} = \frac{p_{px}}{\Gamma}, \tag{3.41}$$

$$\Delta p_{mm} = \frac{1}{\Gamma} \sqrt{N \Delta L^2 + \left(\frac{p_{px} \Delta \Gamma}{\Gamma}\right)^2}, \tag{3.42}$$

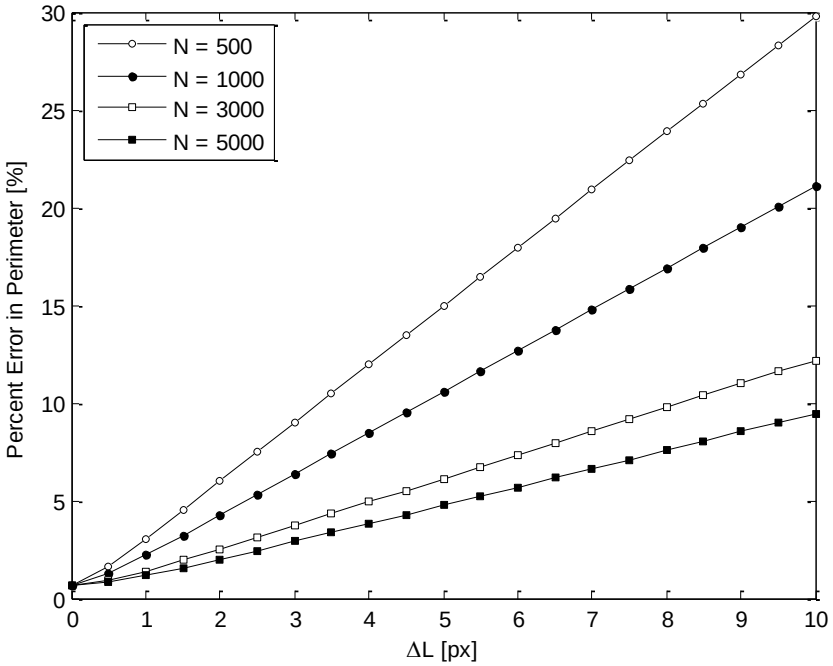

Figure 24. Effect on perimeter error as the size of variance and number of points varies. Γ = 765 px/mm, $\Delta\Gamma$ = 5 px, p_{px} = 1.5N.

Figure 24 illustrates the effect of changing ΔL for different perimeter sizes under typical conditions. As the perimeter location becomes more precise, error is on the order of 1-3%. However if the fit becomes worse, errors as high as 20-30% may occur, which reinforces the importance of correct calibration. It is also apparent that as the total size of a drop increases, the error is decreased because the effect of the small variations relative to the total perimeter is decreased. Measurement of drop perimeter is not typically discussed in frost growth literature, as it is not usually considered an important parameter. Thus there is no data for comparison. This method nonetheless has the potential for great accuracy as long as care is taken to calibrate the equipment properly.

Droplet area

The drop area depends on the drop perimeter and shape. Due to its dependence on shape, it is not simple to evaluate the error associated with area calculations on an arbitrarily shaped drop. However, the possibility exists to estimate the error if it is assumed that droplets tend to form nearly circular shapes. In that case, the error can be found to give an idea of its order of magnitude and it is assumed that drops of similar shape will share similar errors.

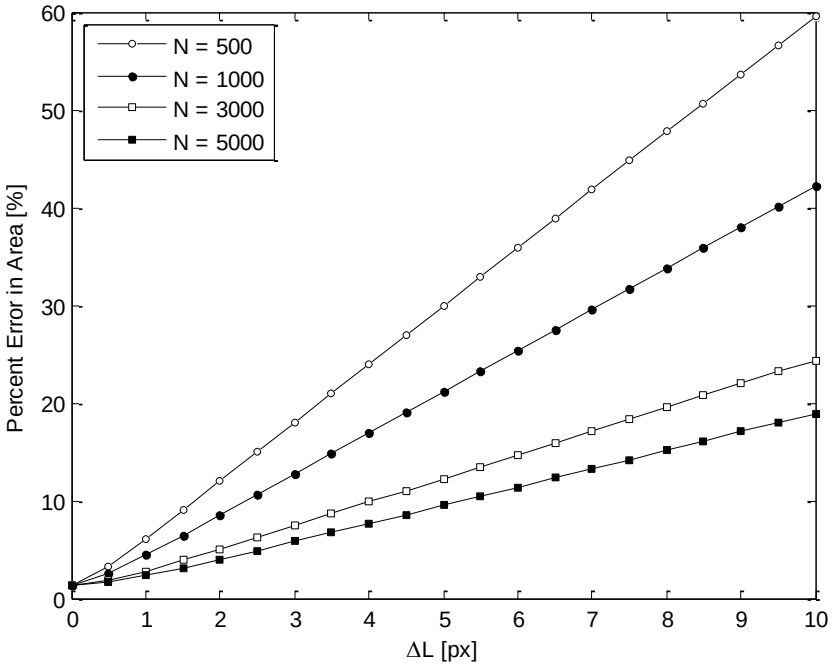

Figure 25. Effect of changing perimeter uncertainty on the error in area for various perimeters. Γ = 765 px/mm, $\Delta\Gamma$ = 5 px, P_{px} = 1.5N.

For a circular droplet, the area in mm can be calculated with Eq. (3.43),

$$A_{mm} = \pi r_{mm}^{\ 2} = \frac{p_{mm}^{\ 2}}{4\pi}. \tag{3.43}$$

Application of the uncertainty equation yields Eq. (3.44), where all measurements are in millimeters except where noted,

$$\Delta A = \sqrt{\left|\frac{\partial A}{\partial p}\right|^2 \Delta p^2} = \frac{\partial A}{\partial P}\Delta p = \frac{2p}{4\pi}\Delta p = \frac{p_{px}}{2\pi\Gamma}\Delta p. \tag{3.44}$$

The total uncertainty can be evaluated rather by taking combining Eqs. (3.41), (3.42) and (3.44) to obtain Eq. (3.45),

$$\Delta A_{mm} = \frac{p_{px}}{2\pi\Gamma^2}\sqrt{N\Delta L^2 + \left(\frac{p_{px}\Delta\Gamma}{\Gamma}\right)^2}. \tag{3.45}$$

The percentage of error in area resulting from changing the perimeter variance for various perimeter lengths is shown in Figure 25 for the same parameters as Figure 24. It is clear that while absolute perimeter error is easier to keep small, the relative error in area calculations may easily exceed 10% especially for small drops. It is obvious that to obtain good results it is necessary to eliminate as much of the variance as possible by making careful calibrations. As with perimeter, droplet area is not covered in most frost growth literature. However it is once again clear that reasonably good accuracy may be found given careful preparation.

Convection coefficient

Uncertainty associated with the convection coefficient is straightforward since the variance of temperature is known from Table 9. Direct application of Eq. (3.20) to the convection coefficient equation (Eq. (3.10)) will yield a useable result,

$$\bar{h} = \frac{4k}{3L}\left(\frac{gP^2L^3\left(T_a - T_c\right)\left(s + T_a\right)^2}{4\left(bR\right)^2 T_a^{\,6}} \right)^{1/4} m\left(Pr\right). \tag{3.10}$$

Consider a rearrangement of the terms in Eq. (3.10) so that the constants are grouped,

$$A \equiv \left(\frac{4m\left(Pr\right)k}{3L} \right)\left(\frac{gP^2L^3}{4\left(bR\right)^2} \right)^{1/4}. \tag{3.46}$$

Note that that thermal conductivity, k, and Prandtl number of the air have also been grouped as constants to greatly simplify the analysis because they do not vary much over the temperature range of interest. Then Eq. (3.10) is re-written as Eq.(3.47),

$$\bar{h} = A\left(\frac{\left(T_a - T_c\right)\left(s + T_a\right)^2}{T_a^{\,6}} \right)^{1/4}. \tag{3.47}$$

Applying the uncertainty equation gives Eq. (3.48), where ΔT is factored out because it is equal for all of the thermocouples.

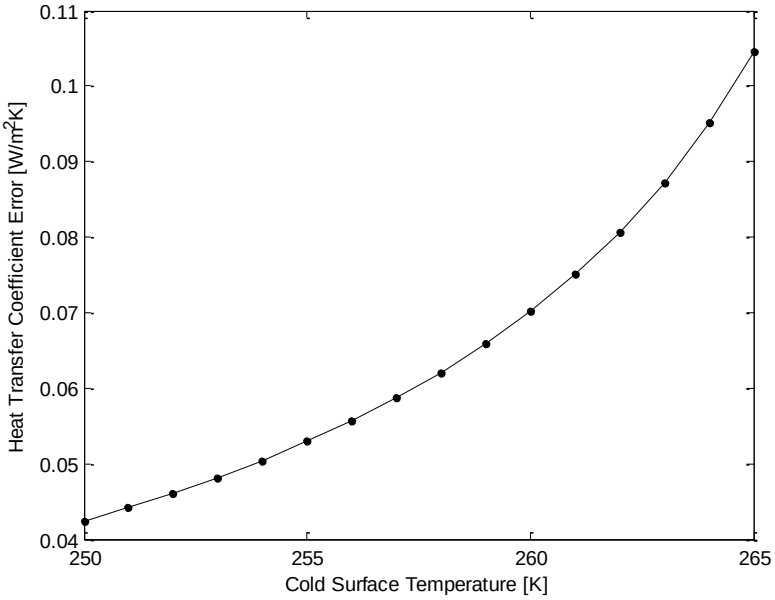

Figure 26. Error in estimation of the heat transfer coefficient for free convection.

$$\Delta\bar{h} = \Delta T \sqrt{\left(\left| \frac{\partial \bar{h}}{\partial T_a} \right|^2 + \left| \frac{\partial \bar{h}}{\partial T_c} \right|^2 \right)}. \tag{3.48}$$

A complete analysis of Eq. (3.48) entails a lengthy solution process, and is therefore omitted (see **Error! Reference source not found.**). After performing the required operations, Eq. (3.49) is the outcome,

$$\Delta\bar{h} = \frac{A\Delta T}{4} \frac{\left[T_a{}^2 (s + T_a)^2 + (5sT_a + 3T_a{}^2 - 6sT_c - 4T_a T_c)^2 \right]^{1/2}}{T_a{}^{5/2} \left(T_a - T_c \right)^{3/4} \left(s + T_a \right)^{1/2}}. \tag{3.49}$$

Observation of Eq. (3.49) leads one to the conclusion that as T_a approaches T_w the error approaches a singularity. This occurs because at that point heat transfer ceases to occur, making the derivatives dh/dT tend towards infinity. To avoid introducing the resulting error into the computation (it is physically unrealistic), the average convection coefficient error is calculated by integrating Eq. (3.49) over the range of 250 to 265 K (Figure 26), which is the approximate range of surface temperature conditions (encompassing both the cold plate and air frost interface) while the air temperature is held at 273 K. Integration is performed numerically owing to the

complexity of Eq. (3.49). For the conditions of Pr = 0.71 and 38.1 mm plate length, it is found that $\Delta\bar{h} \approx \pm 0.064$ W/m^{2}K over the range of interest.

Frost density

Frost density can be found using Eq. (3.16) (repeated below) by neglecting the presence of water vapor in the voids for simplification. Water vapor density is on the order of 0.02 kg/m^3 in the range of -10 to 0 °C, which is not significant compared to the densities of ice and air.

$$\rho_f = \varepsilon_a \rho_a + (1 - \varepsilon_a)\rho_i. \tag{3.16}$$

Finding the uncertainty in Eq. (3.16) if air and ice density are treated as constants over the range of interest gives Eq. (3.50).

$$\Delta\rho_f = \sqrt{\left|\frac{\partial\rho_f}{\partial\varepsilon_a}\right|^2 \Delta\varepsilon_a{}^2} = \left|\frac{\partial\rho_f}{\partial\varepsilon_a}\right| \Delta\varepsilon_a = \Delta\varepsilon_a \left|\rho_a - \rho_i\right|. \tag{3.50}$$

The density difference is about 917.7 kg/m^3. Thus, Eq. (3.50) can be written as Eq. (3.51). The uncertainty in the frost density is greatly affected by the porosity error, which was defined in Eq. (3.26) as the error in the conversion value, σ,

$$\Delta\rho_f = 917.7\Delta\varepsilon_a. \tag{3.51}$$

It is estimated that the error in σ is on the order of ±0.05, about a 10% error. For a calibrated system it is likely that error will be around or less than this value. Then through Eq. (3.51), the average expected density error is about 46 kg/m^3. This is an interesting result, because it is rather large (9 - 15% relative error) and is consistent with the variation between many correlations.

Thermal conductivity

The thermal conductivity is determined by the LeGall [20] correlation as described in section 2.3.2. The equations are re-written below in terms of the air based porosity, ε_a, (volume fraction of air to ice) as opposed to the ice fraction porosity. The LeGall correlation is,

$$\frac{1}{k_f} = \frac{C_1}{k_{perp}} + \frac{1-C_1}{k_{par}}, \tag{2.10}$$

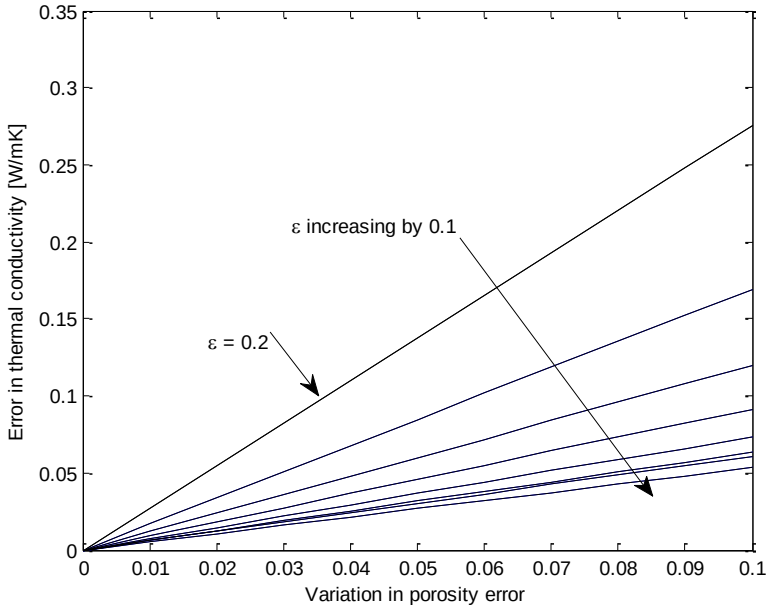

Figure 27. Error in thermal conductivity based on porosity error. ρ_f = 350 kg/m^3.

$$\frac{1}{k_{perp}} = \frac{\varepsilon_a}{k_a} + \frac{1-\varepsilon_a}{k_i}, \tag{2.11}$$

$$k_{par} = \varepsilon_a k_a + (1-\varepsilon_a) k_i, \tag{2.12}$$

$$C_1 = 0.042 + 0.42(0.995)^{\rho_f}, \tag{2.13}$$

and the uncertainty is due to uncertainty in the frost density and porosity estimation. The uncertainty equation gives,

$$\Delta k_f = \sqrt{\left|\frac{\partial k_f}{\partial \rho_f}\right|^2 \Delta\rho_f{}^2 + \left|\frac{\partial k_f}{\partial \varepsilon_a}\right|^2 \Delta\varepsilon_a{}^2}, \tag{3.52}$$

where $\Delta\rho_f$ and $\Delta\varepsilon_a$ are defined by Eqs. (3.51) and (3.26) respectively. If it is assumed that the thermal conductivities of ice and air are approximately constant in the range of interest, Eq. (3.52) can be evaluated. However, the resulting expression is large and inconvenient to work with. As a

result, it is excluded here in favor of a graph showing the variation of Δk_f with $\Delta\varepsilon$ (Figure 27). The average error is estimated to be $\Delta k_f \approx \pm 0.05$ W/mK.

Specific heat

The specific heat can be found using Eq. (3.18) in which case the uncertainty will be analogous to that for the density (Eq. (3.50)). However, neglecting the water vapor will result in less realistic specific heat. The density of water vapor is low, but the specific heat is not. Chen, et al. [3] have used a mass averaged specific heat that includes water vapor. The result is given as Eq. (3.53). If the specific heat and density of the water vapor and air are treated as constants over the range of interest, the analysis is greatly simplified.

$$C_p = \frac{(1-\varepsilon_a)\rho_i C_{pi} + \varepsilon_a \left(C_{pv}\rho_v + C_{pa}\rho_a\right)}{\rho_f}. \tag{3.53}$$

Evaluation of the uncertainty yields,

$$\Delta C_p = \sqrt{\left|\frac{\partial C_p}{\partial \rho_f}\right|^2 \Delta\rho_f{}^2 + \left|\frac{\partial C_p}{\partial \varepsilon_a}\right|^2 \Delta\varepsilon_a{}^2}, \tag{3.54}$$

which can be simplified upon substitution of the density error, Eq. (3.51) to obtain,

$$\Delta C_p = \Delta\varepsilon_a \sqrt{\left|\frac{\partial C_p}{\partial \rho_f}\right|^2 (917.7)^2 + \left|\frac{\partial C_p}{\partial \varepsilon_a}\right|^2}. \tag{3.55}$$

Evaluation of the derivatives and simplification gives Eq. (3.56) which shows that the specific heat error depends on the error in porosity, the frost density, and the value of the porosity.

$$\Delta C_p = \frac{\Delta\varepsilon_a}{\rho_f{}^2} \sqrt{\begin{aligned}&\rho_f{}^2\left[\rho_a C_{pa} - \rho_i C_{pi} + \rho_v C_{pv}\right]^2 + \\ &(917.7)^2\left[\varepsilon_a\left(\rho_v C_{pv} + \rho_a C_{pa}\right) + (1-\varepsilon_a)\rho_i C_{pi}\right]^2\end{aligned}}. \tag{3.56}$$

Figure 28 shows a plot of Eq. (3.56) over a variation in ε and $\Delta\varepsilon$. It is clear that the uncertainty is great, owing to the already large uncertainty of the frost density. The compounding

effect of both uncertainties makes it difficult to estimate the specific heat in this manner unless the porosity error is quite small. The average error is estimated to be $\Delta C_{pf} \approx \pm 300$ J/kgK.

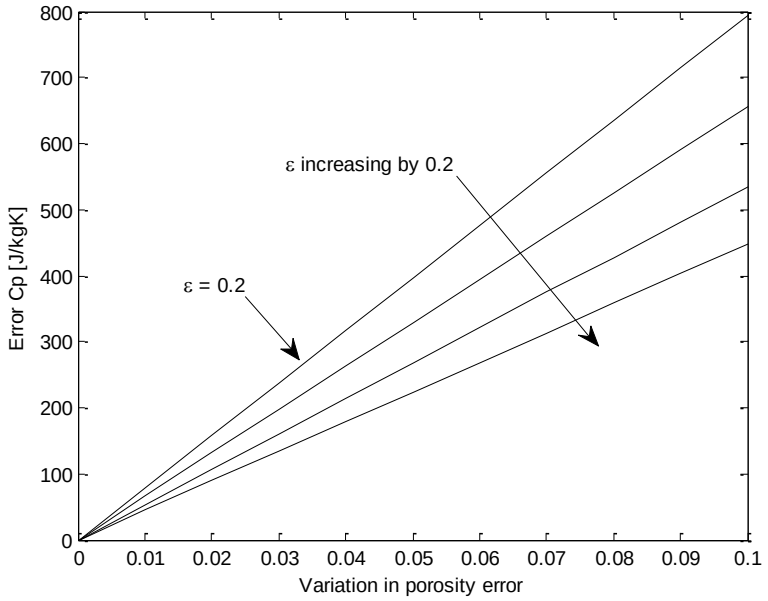

Figure 28. Specific heat error resulting from uncertainty of porosity. ρ_f = 450 kg/m^3.

Table 10. Summary of uncertainty of experimental parameters.

Calculated Parameters	Method	Uncertainty
Thickness	Physical	±0.1 mm
Thickness	Image Acq.	±0.01 mm
Drop Perimeter	Image Acq.	±10%
Drop Area	Image Acq.	±10%
HT Coefficient h	Calculated	±0.064 W/m²K
Thermal Conductivity	Calculated (ε)	±0.05 W/mK
Density	Calculated (ε)	±46 kg/m³
Specific Heat	Calculated (ε)	±300 J/kgK

Summary of uncertainty

Table 10 gives a summary of the estimated average uncertainty for the variables listed above. It is evident from the analysis that computer based visual measurements are indeed capable of achieving high levels of accuracy. The caveat is that very fine calibration is required, or large errors begin to show up in the physical properties such as density and specific heat. Variables such as thickness, perimeter and area are less susceptible to miscalibration but still require good estimation of the scaling error Γ.

4 Comparative models for frosting and defrosting Analytical Solutions

4.1 Background

Before accurate comparisons between experimental data acquired during frost growth and correlations from literature can be made, the testing procedure and apparatus must be carefully examined. Frost growth models are based on ambient and test surface conditions, making it essential that the apparatus is capable of providing exact measurements of related parameters. The parameters to be considered are the heat flux through the test surface, heat leakage from the thermoelectric modules, test surface temperatures, humidity, and coefficients for heat and mass transfer between the surface and interior air.

The general approach is to obtain measurements of temperature and heat flux for the test surface along with interior and exterior ambient temperatures under conditions of controlled humidity (so that latent effects are removed). By removing the latent effects (i.e.; condensation and frost formation) the system can be simplified for representation by classical analytical models. The measured data can then be compared to the models to establish their validity.

Once the testing procedure is shown to be valid under dry conditions, it can be extended to include the frost growth (non-dry) conditions. It can be inferred from the dry testing that the results obtained during frost growth will also be valid in the test assembly domain, since there is no change in the procedure or measurement technique. The results obtained during frost growth are compared to the correlations and models presented in current literature (chapter 5).

4.2 Test surface model for heating and cooling

Under dry conditions, several analytical and approximate techniques can be used to predict the temperature distribution and heat flux in the test surface and through the chamber walls. The most reasonable choice for this type of analysis is a full three dimensional model that can be solved numerically because the geometry of the apparatus does not lend itself to analytical solution easily. Before such a model can be developed, a series of logical steps must be taken to ensure that it accurately predicts the system behavior. Chapter 4 outlines those steps and the results required to set the stage for deeper analysis. Owing to its complexity, a full three-dimensional analysis is only discussed briefly (0), but is suggested for use in future apparatus development to optimize improvements.

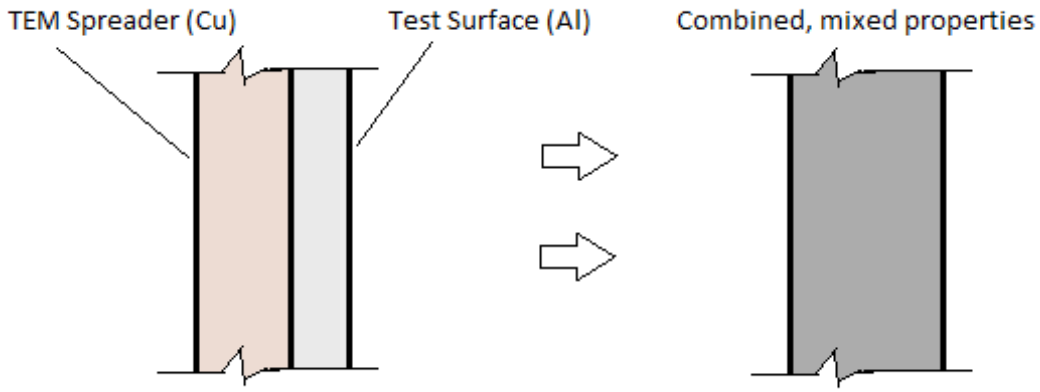

Figure 29. Modification of geometry for modeling purposes. Mass and volume averaged properties are applied to maintain behavior.

The geometry of concern, which is the copper heat spreader and aluminum test surface, is modeled first as a one dimensional transient problem. An approximate lumped solution developed to mimic experimental conditions with more simplicity follows, which is validated by comparison under identical conditions. The results can then be extended to the three dimensional domain and appropriate geometry for further analysis. The approximate models are developed with a flexible approach so that heat flux measured during the experiment can be applied to them when represented as a time dependent function.

There are two bounding possibilities for heat removal on the test surface by the thermoelectric module: constant applied temperature and constant applied heat flux. The actual heat removal rate will fall somewhere between these two extremes. Thus, experimental results exist somewhere within that range.

4.3 One-dimensional transient models: Exact solutions

The one-dimensional transient problem is considered as a plane wall of the same thickness as the test surface and spreader combination, but with weighted properties to account for the different material types. The cases of volume averaged and mass averaged properties are considered and compared (Figure 29). The contact resistance between the pieces is neglected, as it is small due to the use of thermal grease and also because the model is to serve primarily as validation for the numerical model into which the resistance is more easily incorporated. Thus, the solution domain is reduced from the variable area multiple sectioned geometry to an isotropic plane wall which is easily handled by direct application of the heat equation.

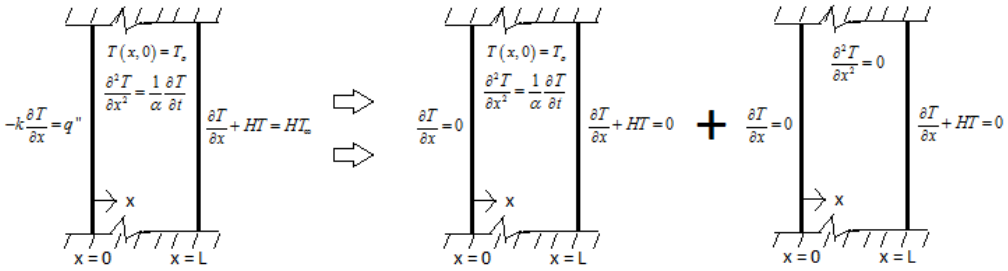

Figure 30. Problem splitting technique as applied to the test surface for the case of a constant applied heat flux.

In addition to the full solution to the heat equation the simplified case of a lumped system is considered. It is advantageous here because it allows for the application of time varying boundary conditions without the need for more mathematically complex techniques required when spatial distribution is included. In particular, this is useful for implementing experimentally recorded heat flux through the thermoelectric module as a function of time to model the most realistic situation possible.

4.3.1 Exact solution: One dimensional conduction with an applied heat flux and surface temperature

Two cases are investigated: applied heat flux and applied surface temperature. The applied heat flux model is considered first. The heat equation can be applied to the geometry in Figure 29 directly. With the assumption of constant properties, the governing equation is reduced to the parabolic form. The boundary condition representing the thermoelectric module is a constant applied heat flux, and the exposed test surface is modeled as a mixed (convective) environment at an ambient temperature (Eqs. (4.1) and Figure 30).

$$\frac{\partial^2 \mathrm{T}}{\partial \mathrm{x}^2}=\frac{1}{\alpha}\frac{\partial \mathrm{T}}{\partial \mathrm{t}},$$

$$\begin{aligned} -\mathrm{k}\frac{\partial \mathrm{T}}{\partial \mathrm{x}} &= \mathrm{q}'', && \mathrm{x}=0,\ \mathrm{t}>0, \\ \frac{\partial \mathrm{T}}{\partial \mathrm{x}}+\mathrm{HT} &= \mathrm{HT}_\infty, && \mathrm{x}=\mathrm{L},\ \mathrm{t}>0, \\ \mathrm{T}(\mathrm{x},\mathrm{t}) &= \mathrm{T}_{0,} && 0\le \mathrm{x}\le \mathrm{L},\ \mathrm{t}=0. \end{aligned} \tag{4.1}$$

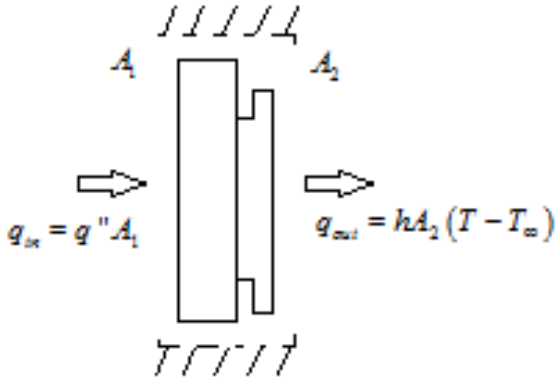

Figure 31. Control volume for the lumped solution.

Because of the nonzero heat flux and ambient temperatures, the problem given by Eqs. (4.1) is not homogenous and must be solved by the technique known as problem splitting [40]. The problem splitting method is illustrated in Figure 30. To solve the problem it is assumed that the solution takes the form given by Eq. (4.2), which is the superposition of a solution to the homogeneous version of the problem and the steady state solution,

$$T(x,t) = T_h(x,t) + T_{ss}(x). \tag{4.2}$$

It can be shown (**Error! Reference source not found.**) that the pieces of Eq. (4.2) based on the problem of Eqs. (4.1) are given by Eqs. (4.3) and (4.4), where λ_m is the eigenvalue and the positive zeros of the Eq. (4.5),

$$T_h(x,t) = 2\sum_{m=1}^{\infty}\left[\frac{\lambda_m^2 + H^2}{L\left(\lambda_m^2 + H^2\right) + H}\right]\cdot\left[\frac{1}{\lambda_m}\right]\cos(\lambda_m x)\sin(\lambda_m L)\left(T_o - T_\infty - \frac{q''}{h}\right)e^{\left(-\alpha t\lambda_m^2\right)}, \tag{4.3}$$

$$T_{ss}(x) = q''\left[\frac{L-x}{k} + \frac{1}{h}\right] + T_\infty. \tag{4.4}$$

$$\lambda_m \tan(\lambda_m L) = H. \tag{4.5}$$

The second form of solution is that of an applied surface temperature. The approach is exactly the same as the case for the applied surface temperature, but with a different boundary

condition representing the thermoelectric module. That is, instead of Eqs. (4.1), the problem is defined by Eqs. (4.6), where T_c indicates the applied surface temperature.

$$\frac{\partial^2 T}{\partial x^2} = \frac{1}{\alpha}\frac{\partial T}{\partial t},$$

$$\begin{aligned} &T(x,t) = T_c, && x = 0, \quad t > 0, \\ &\frac{\partial T}{\partial x} + HT = HT_\infty, && x = L, \quad t > 0, \\ &T(x,t) = T_0, && 0 \le x \le L, \quad t = 0. \end{aligned} \tag{4.6}$$

Again, by the problem splitting method, it can be shown (**Error! Reference source not found.**) that Eqs. (4.7) to (4.9) represent the solution in the combined form given by Eq. (4.2), where U is the overall convection coefficient, given by Eq. (4.10),

$$T_h(x,t) = 2\sum_{m=1}^{\infty}\left[\frac{\lambda_m^2 + H^2}{L\left(\lambda_m^2 + H^2\right) + H}\right]\cdot\left[\frac{1-\cos(\lambda_m L)}{\lambda_m}\right]\cdot \sin(\lambda_m x)\left(T_o - T_\infty + \frac{U}{h}(T_\infty - T_c)\right)e^{\left(-\alpha t\lambda_m^2\right)}, \tag{4.7}$$

$$T_{ss}(x) = (T_\infty - T_c)\left(1 - \frac{U}{h}\right)\frac{x}{L} + T_c, \tag{4.8}$$

$$\lambda_m \cot(\lambda_m L) = -H, \tag{4.9}$$

$$U = \left[\frac{L_{sp}}{k_{sp}} + R_c'' + \frac{L_s}{k_s} + \frac{1}{h}\right]^{-1}. \tag{4.10}$$

4.4 One-dimensional transient models: Lumped

The exact solutions represent the cases of constant surface temperature and applied heat flux. In order to obtain a more realistic model of experimental results, the variation of the applied heat flux with time must be considered. The most straightforward way of modeling this change is with a lumped solution approach to the problem given by Eqs. (4.1). The major simplifying assumption for the lumped solution is that the entire system is always at the same instantaneous temperature. In other words, no there is no spatial temperature dependence and the problem can then be solved with an energy balance approach. This assumption is validated both by comparing the time dependence of temperature to that of the exact solution, and by calculating the Biot number for the system.

Consider the control volume shown in Figure 30, where the one dimensional heat flux is considered for the thermal spreader and test surface geometry. In this case the only relevant geometrical features are the areas over which the heat fluxes are distributed and the total volume of the system. An energy balance ignoring spatial temperature distribution and volume averaged properties throughout the medium yields Eqs. (4.11). The energy input is considered as the applied heat flux at the spreader, and the energy loss is due to convection within the test chamber.

$$\rho V C_v \frac{\partial T}{\partial t} = q_{in}(t) - q_{out}(t),$$

$$q_{in}(t) = q''(t) A_1, \tag{4.11}$$

$$q_{out}(t) = h A_2 (T - T_\infty).$$

Rewriting the energy balance gives one an inhomogeneous ordinary differential equation which can be solved to determine T(t) for the system. With the relationship $\psi = T - T_\infty$ and dividing by the capacitance term, Eq. (4.12) can be written as Eq. (4.13), which can be solved by the method of undetermined coefficients if the heat flux function $q''(t)$ is known.

$$\rho V C_v \frac{dT}{dt} + h A_2 (T - T_\infty) - q''(t) A_1 = 0, \tag{4.12}$$

$$\frac{d\psi}{dt} + \frac{hA_2}{\rho VC_v}\psi - \frac{q''(t)A_1}{\rho VC_v} = 0. \tag{4.13}$$

Finally, defining the quantities m and p as the coefficients gives Eq. (4.14). Equation (4.14) can be solved by the method of undetermined coefficients for p = p(t) if a constant convection coefficient is assumed. The solutions given here are constant heat flux (for validation against the exact solution), polynomial fit, and exponential fit heat flux (for validation of experimental results).

$$\frac{d\psi}{dt} + m\psi - p = 0,$$

$$m = \frac{hA_2}{\rho VC_v}, \tag{4.14}$$

$$p = \frac{A_1 q''(t)}{\rho VC_v}.$$

4.4.1 Constant applied heat flux case

If p is a constant in Eq. (4.14), that is, if $q''(t) = q''$, it can be shown (**Error! Reference source not found.**) that the solution $\psi(t)$ is given by Eq. (4.15), where $\psi_o = T_i - T_\infty$. The term $q''A_1/(hA_2)$ can be understood physically as the ratio of energy input to energy loss. As time goes on the transient (exponential) term drops to zero and the steady state is reached and is defined by this ratio. For simplicity, the quantity is redefined as $q''A_1/(hA_2) \equiv q_r$ and Eq. (4.15) can be written as Eq. (4.16). Equation (4.16) is useful because its results can be compared to those of the exact solution to validate the assumptions used in creating the lumped model.

$$\psi(t) = \frac{q''}{h}\frac{A_1}{A_2} + \left(\psi_o - \frac{q''}{h}\frac{A_1}{A_2}\right)\exp\left[-\frac{hA_2 t}{\rho VC_v}\right], \tag{4.15}$$

$$\psi(t) = q_r + (\psi_o - q_r)\exp\left[-\frac{hA_2 t}{\rho VC_v}\right]. \tag{4.16}$$

4.4.2 Time varying heat flux

While the constant heat flux model is appropriate for validation it will not accurately represent the situation present in the experimental setup, where the heat flux varies with time. The thermoelectric module is a relatively constant power device, but the heat flux depends on the temperature difference created by the applied voltage. As the test surface changes temperature, the heat flux must also change if the power is constant. Thus, the most realistic system model is the one which employs a time varying heat flux whose function can be fit to experimental data. The functions chosen to represent the heat flux here are polynomial and exponential to capture a wide variety of possible distributions.

For a polynomial fit, the function q"(t) is represented by a third order polynomial with experimentally determined coefficients e, f, g, and h. The problem is then given by Eqs. (4.17),

$$\frac{d\psi}{dt} + m\psi - p(t) = 0,$$

$$p(t) = \frac{A_1 q''(t)}{\rho V C_v} = \frac{A_1}{\rho V C_v}\left(e + ft + gt^2 + ht^3\right), \tag{4.17}$$

$$m = \frac{hA_2}{\rho V C_v}.$$

By the method of undetermined coefficients, the solution to Eq. (4.17) is given by Eq. (4.18), and the coefficients A, B, C and D are evaluated in terms of the experimental data as Eqs. (4.19). The details of the solution can be found in **Error! Reference source not found.**.

$$\psi(t) = \psi_o \exp\left[-\frac{hA_2 t}{\rho V C_v}\right] + A + Bt + Ct^2 + Dt^3. \tag{4.18}$$

$$A = \frac{A_1}{hA_2}\left(e - \frac{f}{m} + \frac{2g}{m^2} - \frac{6h}{m^3}\right), \qquad B = \frac{A_1}{hA_2}\left(f - \frac{2g}{m} + \frac{6h}{m^2}\right),$$

$$C = \frac{A_1}{hA_2}\left(g - \frac{3h}{m}\right), \qquad D = \frac{A_1}{A_2}. \tag{4.19}$$

Equations (4.18) and (4.19) provide a means of fitting experimental heat flux data to a polynomial function and determining an analytical system response based on the lumped capacitance approach. The same approach can be used to determine the analytical solution if the experimental data is fit with an exponential model. In this case, the problem is given by Eqs. (4.20) where n and r are the experimentally determined coefficients for the exponential,

$$\frac{d\psi}{dt} + m\psi - p(t) = 0,$$

$$p(t) = \frac{A_1 q''(t)}{\rho V C_v} = \frac{A_1}{\rho V C_v}\left(n e^{rt}\right), \tag{4.20}$$

$$m = \frac{hA_2}{\rho V C_v}.$$

The solution to Eqs. (4.20) in the terms of coefficients n and r is found to be Eq. (4.21). Details of the solution are in **Error! Reference source not found.**.

$$\psi(t) = \left(\psi_o - \frac{A_1 n}{\rho V C_v (r+m)}\right) e^{-mt} + \frac{A_1 n}{\rho V C_v (r+m)} e^{rt}. \tag{4.21}$$

4.4.3 Summary of lumped capacitance approach

The assumptions used in the lumped capacitance solution can be validated by comparing the solution for the constant heat flux case to that given by the exact one dimensional solution for the same circumstances. Once the validity is established the lumped solution can be extended to include time varying heat flux cases much more easily than the exact solution, and various experimental curve fits can be used to represent the actual heat flux over time. The results of section 4.4 are summarized below. Derivations are in **Error! Reference source not found.**.

$$\psi(t) = q_r + (\psi_o - q_r) e^{-mt} \qquad q'' = \text{Const} \tag{4.22}$$

$$\psi(t) = \psi_o e^{-mt} + A + Bt + Ct^2 + Dt^3 \qquad q'' = f(t) \tag{4.23}$$

$$\psi(t)=\left(\psi_o-\frac{zn}{r+m}\right)e^{-mt}+\frac{zn}{r+m}e^{rt} \qquad q''=f(t) \tag{4.24}$$

where,

$$m=\frac{hA_2}{\rho VC_v}, \tag{4.25}$$

$$q_r=\frac{q''}{h}\frac{A_1}{A_2}, \tag{4.26}$$

$$z=\frac{A_1}{\rho VC_v}, \tag{4.27}$$

and the coefficients A, B, C, and D are obtainable from Eqs. (4.19).

4.5 Comparison of analytical models

The analytical solution to the transient one dimensional problem has been discussed in terms of exact and lumped solutions, of which the latter is most easily capable of modeling the actual system. It is important to validate this statement by making a comparison between the different models. First, the exact solutions are compared in terms of homogeneous and inhomogeneous applied surface temperature and heat flux conditions. The lumped assumptions are then validated for constant heat flux. Finally predictions of the actual test surface behavior are compared with experimental results.

4.6 Validation of one dimensional inhomogeneous model

The properties used for the simulation are based on experimental measurements (for mass and density) and commonly used values for thermal conductivity and specific heat. The simulation conditions are representative of typical conditions experienced during the frosting experiments. The conditions are summarized in Table 11 and are used for all comparisons. For the exact solutions, the heat flux and temperature conditions are applied at the surface contacting the thermoelectric module (corresponding to x = 0), and the temperatures shown on the plots are those of the test surface at x = L.

Figure 32 shows the results for the applied heat flux solution, Eqs. (4.3) and (4.4) with mass and volume averaged properties. It is evident from the results that the full solution is indeed

Table 11. One dimensional simulation system properties.

Property	Spreader	Test Surface	Thermal Grease	Mass Average	Volume Average
Thickness [m]	8.89E-03	3.18E-03	1.00E-05	-	-
Area [m²]	1.81E-03	1.45E-03	1.06E-03	-	-
Volume [m³]	1.61E-05	4.61E-06	1.06E-08	-	-
Mass [kg]	0.117	0.015	-	-	-
Cp [J/kgK]	385	903	-	443.86	500.12
k [W/mK]	401	237	-	382.36	364.55
α [m²/s]	1.44E-04	8.06E-05	-	1.36E-04	1.30E-04
ρ [kg/m³]	7254.05	3254.60	-	-	-
Resistance [K/W]	1.22E-02	9.23E-03	3.00E-06	-	-
Conditions					
T_o [°C]	9.054				
T_∞ [°C]	0				
T_c [°C]	-6				
h [W/m²K]	8				
q" [W/m²K]	-50				

equal to the homogeneous solution when the conditions are made homogeneous, indicating that the full solution is correct. Furthermore switching from mass averaged to volume averaged properties causes only a slight change in the system behavior, on the order of 0.007 °C. The difference is trivial as it is well within the margin of experimental error. Thus the use of either mass or volume averaged properties makes little difference in the simulation, and the validity of lumping properties rather than analyzing a two sectioned wall may be examined by comparison with experimental results.

In the case of applied surface temperature (Figure 33) there is a larger difference between the two, although it is still below the threshold of experimental error. An average difference of 0.161 °C is observed between the mass averaged and volume averaged results. The discrepancy is a result of the very fast response of the system to a forced temperature, which occurs because the overall mass and thickness are small and thermal conductivity is large. The conditions predicted by the homogeneous solution again match exactly the full solution when homogeneous conditions are present, showing that the superposition of Eqs. (4.7) and (4.8) is the correct solution for the inhomogeneous case.

To further reinforce the validity of the full exact solutions, they are subjected to changes in conditions and compared to the original homogeneous results (see Figures 34 and 35). For the heat flux model the homogeneous condition is an adiabatic surface, and the applied heat flux compared to it is -50 W/m^2K, which is chosen arbitrarily for illustration. In the applied temperature model the homogeneous condition is an applied surface temperature of 0 °C

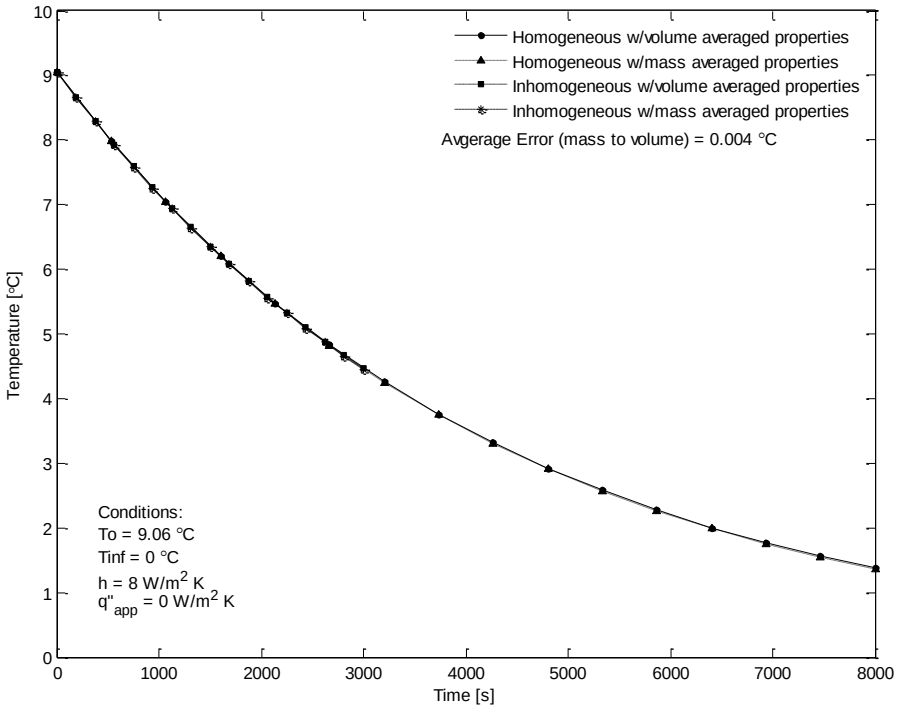

Figure 32. Comparison of homogeneous and inhomogeneous solutions for an applied heat flux on the back surface. Temperatures are on the test surface. See Figure 30 for details.

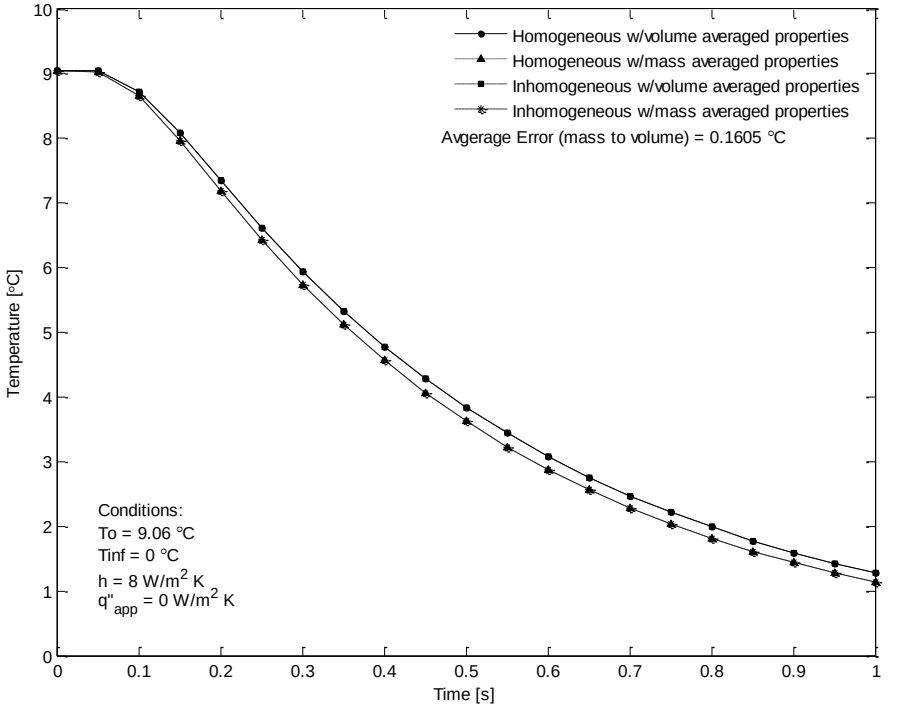

Figure 33. Comparison of homogeneous and inhomogeneous solutions for an applied temperature on the back surface. Temperatures are on the test surface. See Figure 30 for details.

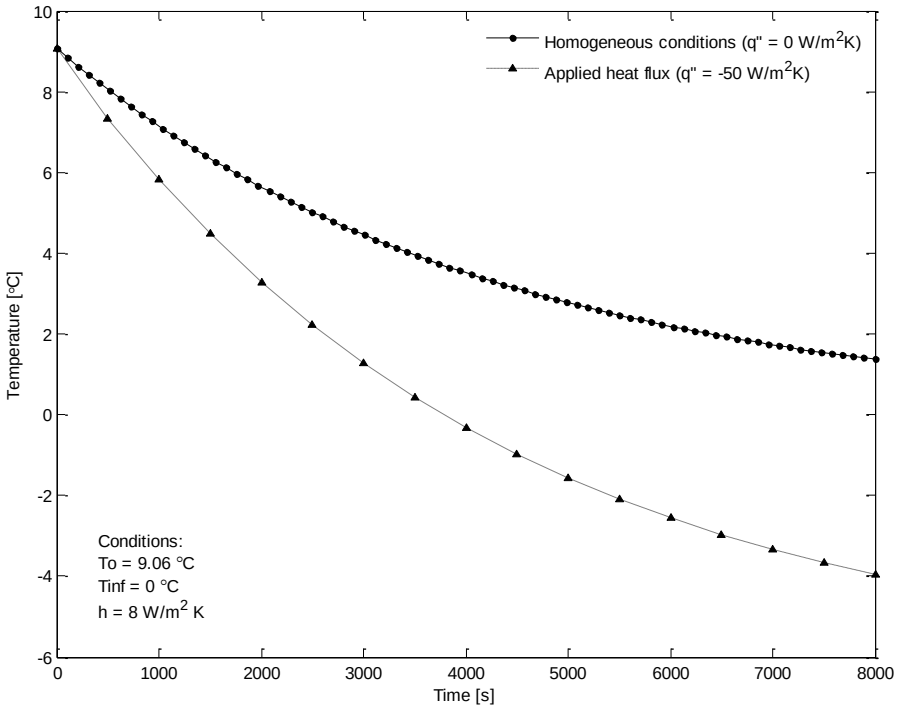

Figure 34. Changes in system response relative to homogeneous conditions if a heat flux of -50 W/m²K is applied to the surface at x = 0.

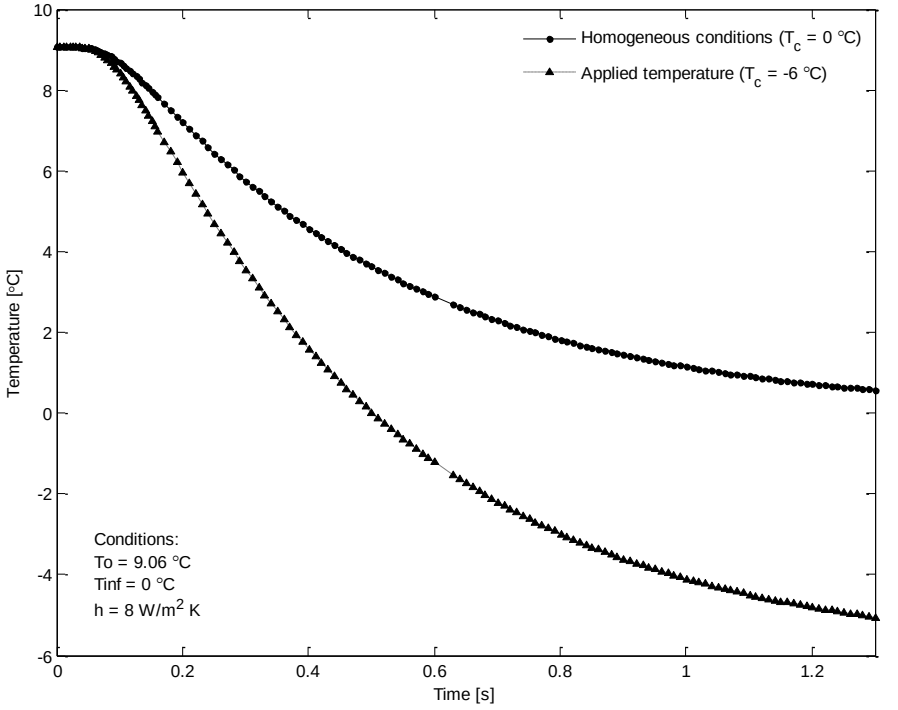

Figure 35. Changes in system response relative to homogeneous conditions if a temperature of -6 °C is applied to the surface at x = 0.

and it is compared to an applied temperature of -6 °C, which is chosen to keep the response in the same range as that for the applied heat flux, which has a steady state temperature of -6.25 °C.

In both cases, the inhomogeneous conditions imposed should cause the temperature to decay at a faster rate since more energy is removed with an outgoing heat flux and a lower surface temperature. The trends in Figures 34 and 35 show qualitatively that the system responds as it should. If the models are accurate the experimental data should fall somewhere in between the two curves of constant surface temperature and applied heat flux, which is examined further in section 4.8.

4.7 Validation of lumped capacitance model

The underlying assumption of the lumped capacitance solution to the problem given by Eqs (4.14) is that any point within the system is at the same instantaneous temperature (no spatial temperature variation). Such an assumption is often an acceptable when the rate of conduction throughout the system is high relative to the rate of heat loss or gain to the system. Typically, the conductive behavior is characterized by the Biot number. Strictly speaking, it is the ratio of heat transfer per unit surface area to conduction per unit volume. The lumped capacitance method is most appropriate when Biot number is less than 0.1.

The Biot number can be evaluated for the homogenous case (no heat flux at the thermoelectric surface), but once the heat flux term is nonzero the Biot number no longer accurately reflects the system behavior. The validity of the lumped solution can still be evaluated for this case by direct comparison with the exact solution. The Biot numbers for the case of homogenous conditions are found to be $Bi_{va} = 3.135 \cdot 10^{-4}$ and $Bi_{ma} = 2.989 \cdot 10^{-4}$,where subscripts va and ma indicate the use of volume or mass averaged thermal conductivity.

Accordingly, the system should be represented accurately in the case of homogeneous conditions. Figure 36 shows the result, where the slight difference between the results is due to the choice of where the exact solution is evaluated. The exact results are evaluated at the test surface (x = L), and the lumped solution is a mass average by nature. The exact solution is somewhat lower than the lumped solution because it is evaluated at a point in direct contact with the cold environment.

No Biot number analogue exists for the case where heat flux is applied, but the comparison to the exact solution (Figure 36) shows that the results still agree quite well. The high thermal conductivity and small system size mean that even at large values of heat loss or applied heat flux, the lumped approximation is still reasonable. In fact the convection coefficient representing total heat loss would have to approach nearly 5,000 W/m^2K before the Biot number

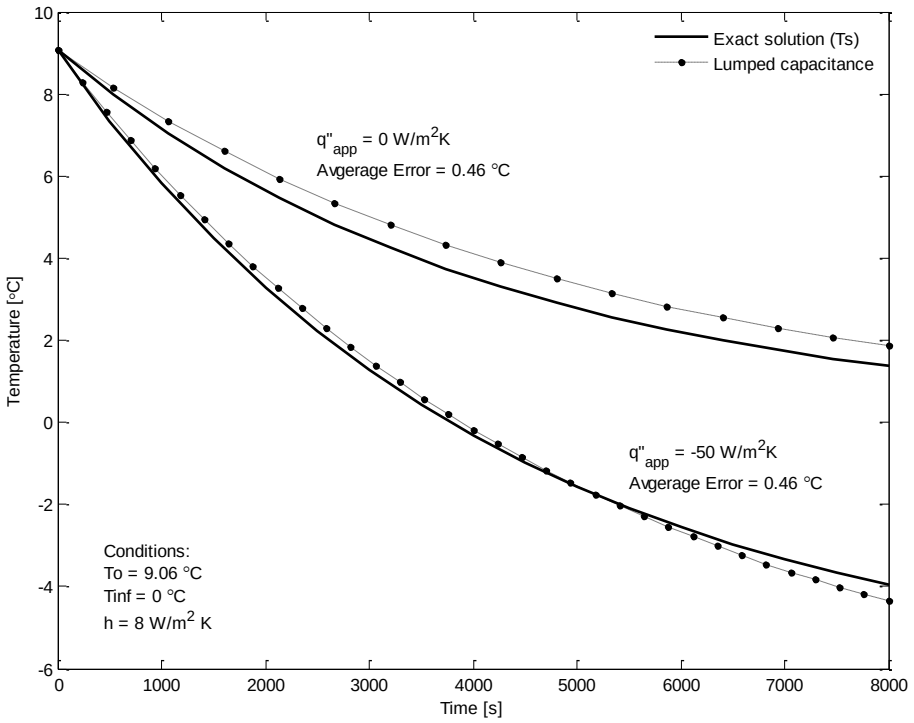

Figure 36. Comparison of exact and lumped solutions for the case of an adiabatic surface at x = 0 and an applied heat flux of -50 W\m^{2}K. Exact is evaluated at the test surface boundary at x = L.

approaches 0.1. To illustrate, for a difference of ~5 degrees on average between the test surface and environment the corresponding heat flux is ~50,000 W/m^2, which is far greater than any applied heat flux in the experiments. Therefore it is reasonable to assume that the inhomogeneous lumped capacitance model with time varying heat flux can be used to model the experimental system, and this conjecture is validated by the results in Figure 36.

4.8 Experimental validation of heat transfer models.

The analytical models are compared to experimental results for validation. The validation procedure consists of taking data during heating and cooling of the test surface with a constant interior chamber temperature and very low dew point to prevent latent thermal effects. The required experimental parameters include the interior chamber temperature, and the test surface temperature and heat flux as functions of time. The transient temperature curves are then compared to exact and approximate solutions.

Before the analytical curves can be generated, however, the applied heat flux as a function of time must be considered. For the exact case where the applied heat flux must be constant, the average heat flux is used. For the lumped solution, the experimental heat flux data

is fit with either a polynomial or exponential function whose coefficients are then used to determine the response.

Because the measured heat flux includes some loss through the chamber walls, that loss must be subtracted from the data before curve fitting takes place. The correction is achieved by adjusting the system such that the test surface and inside chamber temperatures are equal. Any heat flux measured under such conditions may be considered the loss for that particular interior temperature to ambient temperature difference since there is no heat transfer through the test surface. The loss is subtracted from heat flux during heating or cooling when the chamber is at the same temperature to find the true surface flux.

4.8.1 Results of heating and cooling tests

For the cooling tests, the system is initially brought to a steady state condition around 0 °C. Once the balance is reached, the thermoelectric module is given a large voltage increase and the system response is recorded until a new steady state is reached. During the tests the power input to the thermoelectric module remains relatively constant, as does the inside air temperature of the chamber. The losses are evaluated and subtracted from the total heat flux to obtain the heat flux for modeling.

The cooling test results are shown in Figures 37 and 38. Figure 37 shows the heat flux model used as an input for the lumped capacitance solution. A third order polynomial is the better fit for the data (as opposed to an exponential) although the shape appears to be exponential. A power law fit would likely yield a more accurate model, but the polynomial does give a reasonable representation. Erroneous locations are near the early and late times, which are considered less significant since they are typically ignored during frost growth measurements.

The comparative results for temperature curves are shown in Figure 38. As they should, the conditions of applied temperature and heat flux bound the experimental data. The lumped solution based on the time varying heat flux model very closely approximates the actual experimental data. Most of the error appears to be a result of the polynomial fit for the heat flux. The wavy nature of the lumped curve and the clear error near the later times in the heat flux curve support that conclusion. The results imply that the experimental methods and measurements used to obtain the temperatures and heat flux data during cooling are valid since they behave as expected, and that the models themselves can be used to accurately represent that behavior.

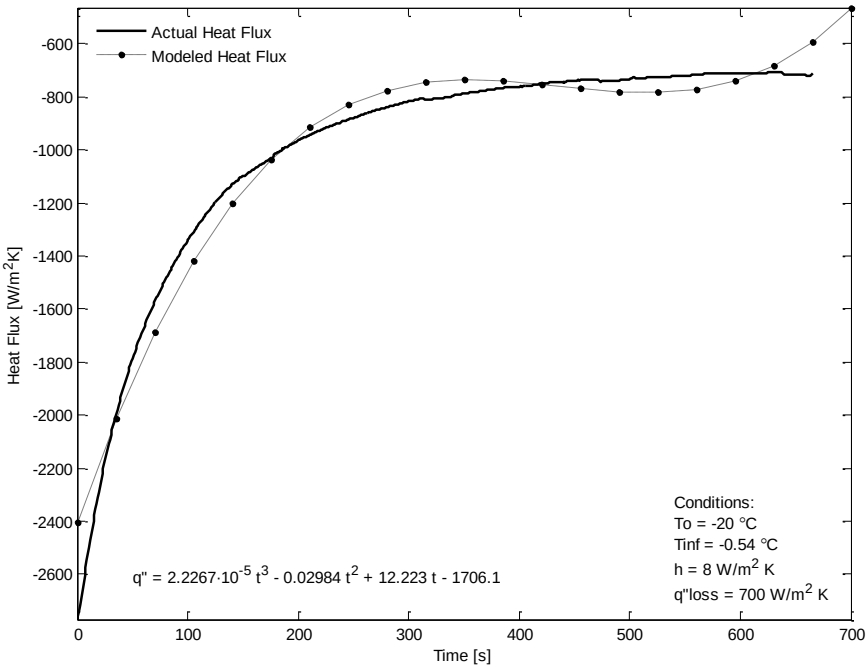

Figure 37. Heat flux model prior to subtraction of the losses as compared to the recorded heat flux during cooling.

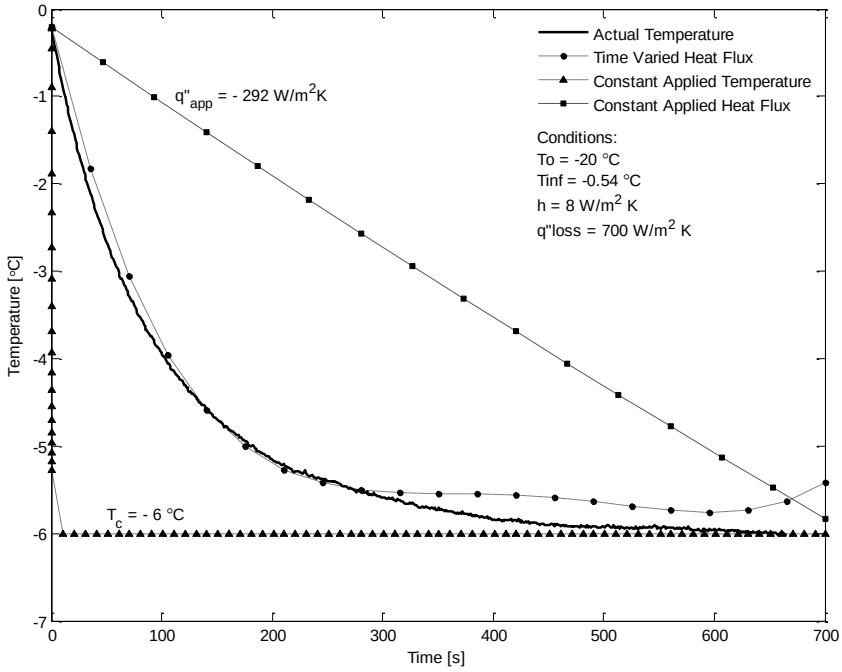

Figure 38. Comparison of experimental and analytical temperature curves during cooling. The system is bounded by the conditions of applied heat flux and surface temperature cases.

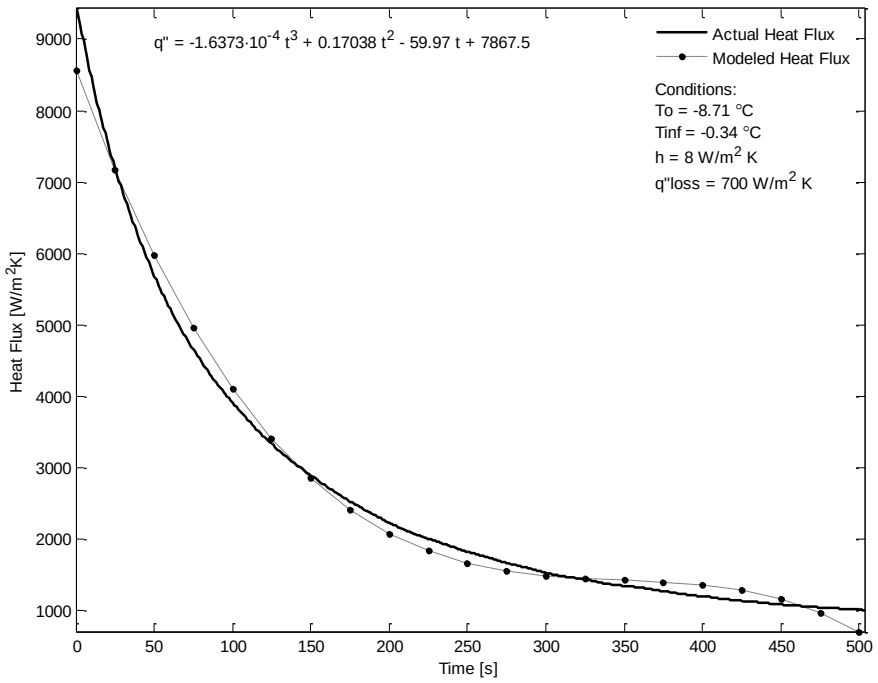

Figure 39. Heat flux model prior to subtraction of the losses as compared to the recorded heat flux during heating.

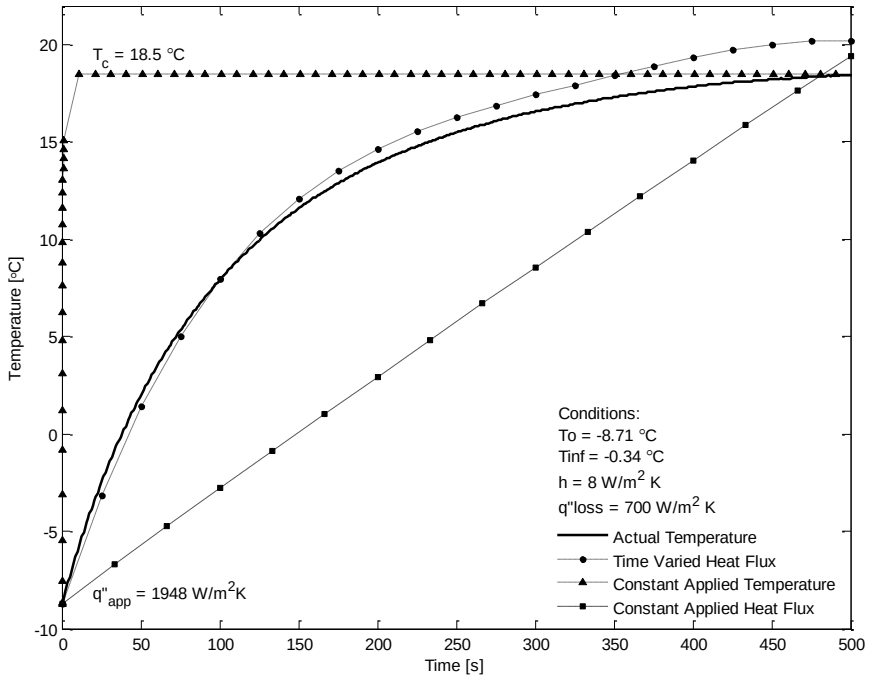

Figure 40. Comparison of experimental and analytical temperature curves during heating. The system is bounded by the conditions of applied heat flux and surface temperature cases.

Figures 39 and 40 show the same results, but during heating rather than cooling. Again, the heat flux over time is most closely approximated with a third order polynomial with the greatest error in the early times. As with the case of cooling, the actual data is bounded neatly by the extreme cases of applied heat flux and surface temperature. The close fit of the results again imply that the model is valid and the system behavior is understood.

5 Frost growth modeling

The previous chapters have described various new methods for obtaining parameters such as frost thickness, porosity, drop perimeter and area along with descriptions of the traditional methods used in their place. An error analysis was presented in section 3.5 to give an idea of the uncertainty of those parameters. In this section, experimental results are used to calculate and compare the primary parameters to those obtained in other experiments and to correlations available in current literature.

5.1 Frost thickness

5.1.1 Comparison to correlations

The frost thickness for several data sets has been calculated in the manner outlined in section 3.3.3. Each of the different thicknesses (maximum, average, and minimum) has been plotted in Figures 41 through 44 against the correlations given by Eqs. (2.1) to (2.6), which are repeated here for convenience,

Schneider (1978),

$$\delta_f = 0.465\left[\frac{k_i t}{h_{sg}\rho_i}\left(T_{fs} - T_w\right)\right]^{1/2}\left(\frac{t}{60}\right)^{-0.03}\left(T_{fs} - T_w\right)^{-0.01}\Pi^{0.25}F_t, \tag{2.1}$$

Cremers and Mehra (1980),

$$\delta_f = 0.12\left[t\left(T_{fs} - T_w\right)\right]^{0.43}, \tag{2.2}$$

Mao et al. (1992),

$$\delta_f = 0.156\left(w\right)^{1.723}\left(x^*\right)^{-0.098}\left(T^*\right)^{1.10}\left(Re_D\right)^{0.343}\left(Fo\right)^{0.655}, \tag{2.3}$$

Mao et al. (1999),

$$\delta_f = 9.183\cdot 10^{-5}\left(w\right)^{0.4}\left(x^*\right)^{-0.085}\left(T^*\right)^{-1.712}\left(Re_D\right)^{0.449}\left(Fo\right)^{0.669}, \tag{2.4}$$

Lee and Ro (2002),

$$\delta_f = 0.1083\left(w\right)^{1.704}\left(x^*\right)^{-0.1488}\left(T^*\right)^{3.177}\left(Re_D\right)^{0.1424}\left(Fo\right)^{0.6724}\left(D^*\right)^{13.36}, \tag{2.5}$$

Shin et al. (2003),

$$\delta_f = \left(0.0852 + 0.00134\cdot\gamma\right)t^{0.6954-0.00154\cdot\gamma}, \tag{2.6}$$

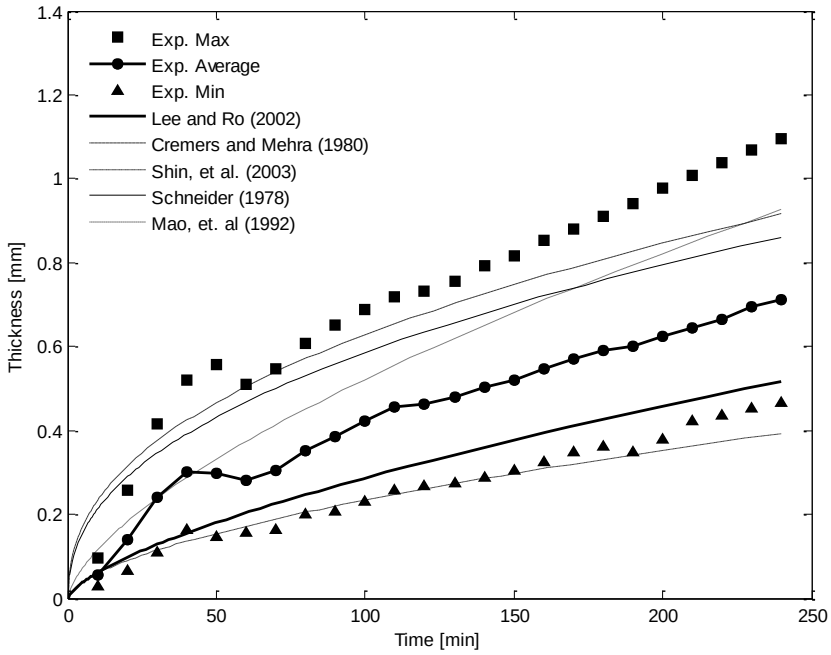

Figure 41. Comparison of thickness measurements to correlation, Run 1.

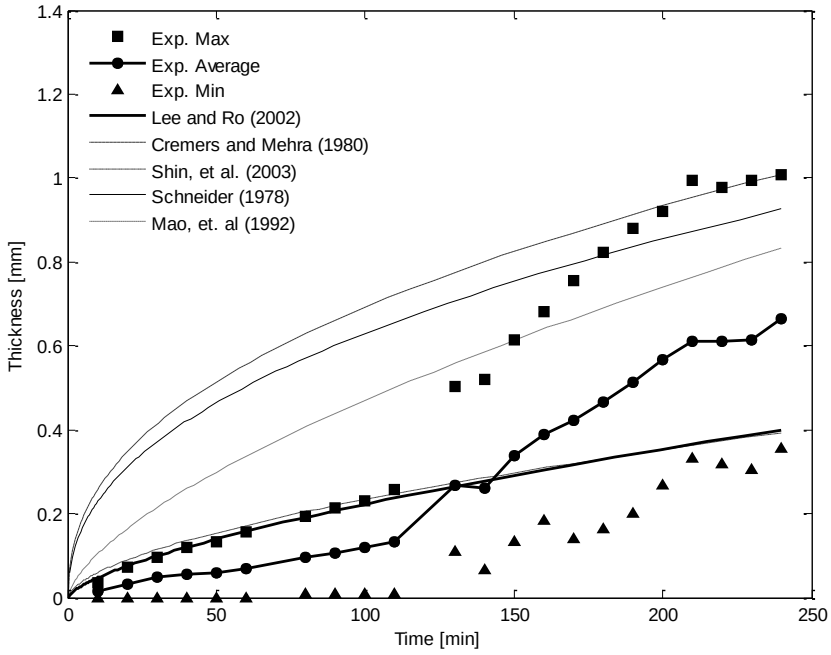

Figure 42. Comparison of thickness measurements to correlation, Run 2.

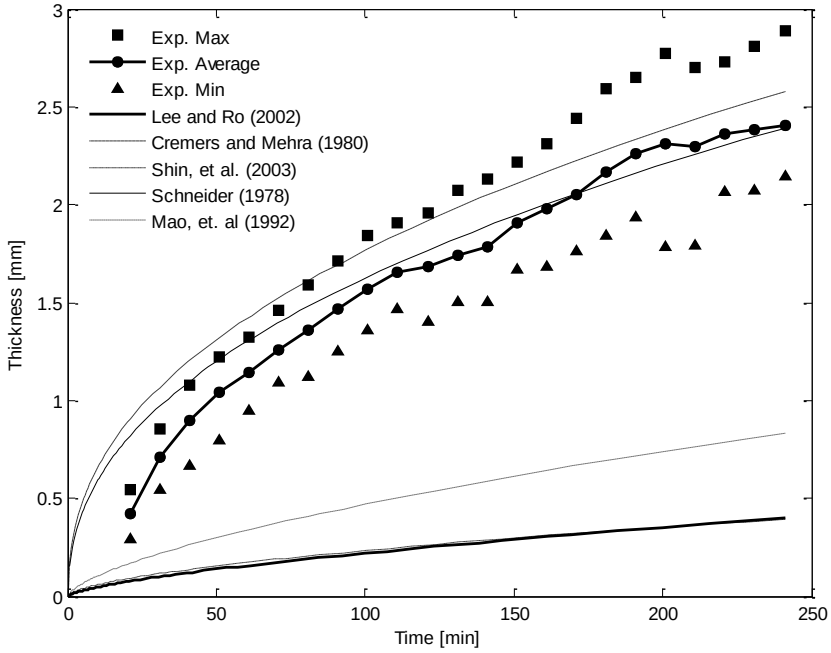

Figure 43. Comparison of thickness measurements to correlation, Run 3.

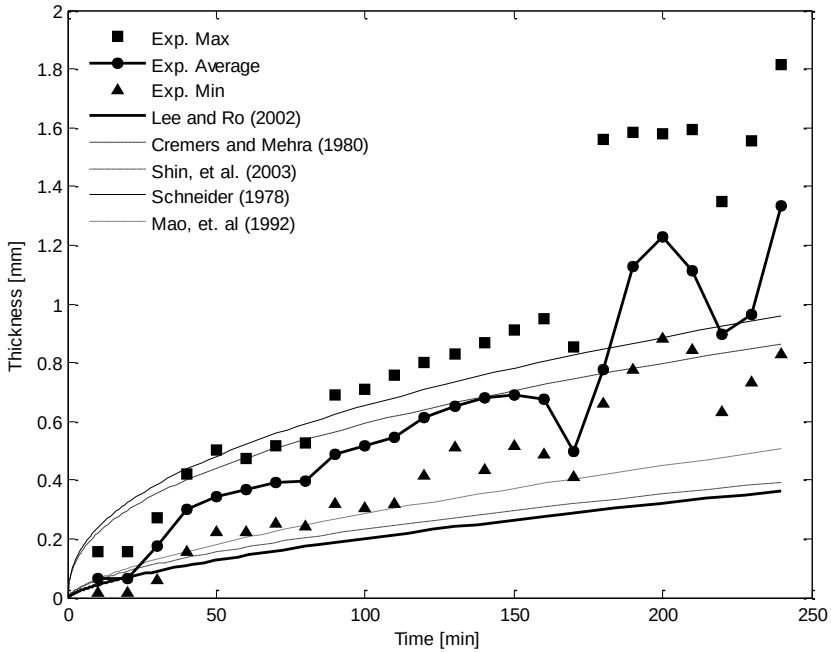

Figure 44. Comparison of thickness measurements to correlation, Run 4.

Table 12. Experimental results relating to frost thickness.

Test Number	**1**	**2**	**3**	**4**
Surface Temp [°C]	-9.97	-9.59	-19.2	-19.41
Chamber Air Temp [°C]	-1.16	-0.06	0.03	-7.72
Dew Point [°C]	-7.74	-7.78	-7.7	-18.25
Interface Temp (est.) [°C]	-9.5	-9	-14	-19
Pressure [kPa]	98.51	96.88	97.17	97.52
Spec. humidity [kgH20/kgDA]	0.00216	0.00210	0.00211	0.0009
Relative humidity %	60.80	58.10	56.00	42.50
θ Parameter	0.75	0.80	0.40	0.90

Listed in Table 12 are the experimental conditions under which the thickness data was obtained. The primary difference in the runs is in the wall and air temperatures. For runs 1 and 2, the temperatures conditions are similar with similar temperatures. In runs 3 and 4 the cold surface temperature is reduced greatly, and the air temperature and dew point are varied.

With the exception of run 3, the correlation presented by Lee and Ro [22] appears to give reasonable estimates of the frost thickness as a function of time. At first glance, the correlations of Shin et al. and Schneider [32, 33] appear to give more reliable results. The good fit is due only to the fact that the interface temperature was not measured in the present experiments. Both of those correlations rely explicitly on the interface temperature, and therefore exact comparison is not possible. To illustrate trends, the interface temperature was estimated based on present experimental data. The estimated temperatures are used to generate plots for correlations which depend on interface temperature.

An interesting point to note is that some correlations tend to predict thicknesses varying over the range of maximum to minimum. The correlations taken as a set tend to envelop the data between higher and lower estimates. It is possible that this is a result of different measurement methods, which have led to different conclusions about the constants in Eqs. (2.1) to (2.6). A more refined measurement method such as the visual method presented here, may collapse the envelope somewhat to a more exact range.

Figures 41 through 44 illustrate clearly the possibility for different thickness measurements obtained under the same conditions. A startlingly large range of variation between maximum and minimum thicknesses indicates that precise relationship of thickness over time will be difficult to determine. High accuracy visual measurement methods have the potential to reduce this difficulty, so that data obtained from multiple experiments can be analyzed with more certainty as to the thickness measurements. This will lead to more exact data fits for determining constants associated with experimental parameters, and decrease the envelope size.

5.1.2 New correlation development

To date, many experimental correlations are based only on the data from certain experimental setups. As a result of this, it has been somewhat of a trend that frost growth correlations only agree with other experimental data to a rather small degree, which is made evident in Figures 41 through 44.

The widespread use of accurate methods will make it possible to integrate data from many sources with greater accuracy and, when that is accomplished, the possibility for more general correlation development will exist. With the ability to compare full sets of parameters over a wide range of conditions outside the scope of a single experiment comes the potential for more exact relationships to be developed.

It is in that spirit that a new form of correlation is explored here based on a wider compilation of data than usual. Not all of the included data sets have used high accuracy methods. Nonetheless, they are included to broaden the range of data.

A first attempt is based only on the experimental data at hand, and a power law type of fit. The parameter θ is introduced as a dimensionless temperature ratio indicating the potential for sensible heat transfer between the chamber air and the frost surface,

$$\theta = \frac{T_a - T_{dp}}{T_a - T_c}. \tag{5.1}$$

The frost growth rate is inversely proportional to θ. As the parameter decreases, either the air temperature nears the dew point or the cold surface temperature is decreased. In both cases the growth is rate is increased. As the air temperature approaches the dew point, it is clear that condensation and deposition is more likely. In the same sense, as the cold surface temperature decreases or the air temperature increases, the difference between the cold surface temperature and dew point temperature increases raising the likelihood of deposition.

Thus it seems appropriate that this dimensionless ratio be used in a characterization of frost growth behavior. The first attempt is made here with an observation of this ratio and the trend of typical frost growth. The humidity and temperatures are the most relevant factors to growth rate, and all other parameters are ignored here (e.g., Reynolds number and position). It is proposed that the average frost thickness can be related to the temperature ratio and time by the relationship,

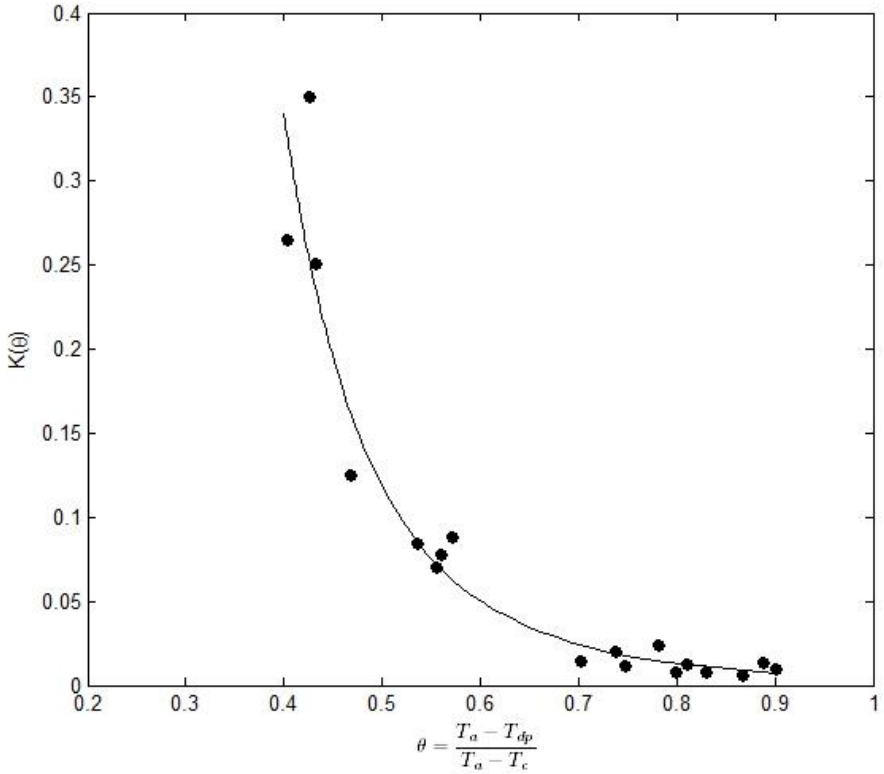

Figure 45. Variation of K parameter with experimental data.

$$\delta(t) = K(t\theta)^{\theta}. \tag{5.2}$$

Equation (5.2) is similar to the correlation proposed by Cremers and Mehra [6] and Schneider [32]. The defining difference is that its coefficients are not fixed. Rather the quantity $t\theta$ is raised to a power dependent on growth conditions, and the growth factor $K = K(\theta)$. The relationship is derived by observation of behavior rather than direct analysis of the governing equations. The parameter K can be calculated directly for an experiment for a given θ by solving Eq. (5.2) explicitly to yield Eq. (5.3),

$$K = \frac{\delta}{(t\theta)^{\theta}}. \tag{5.3}$$

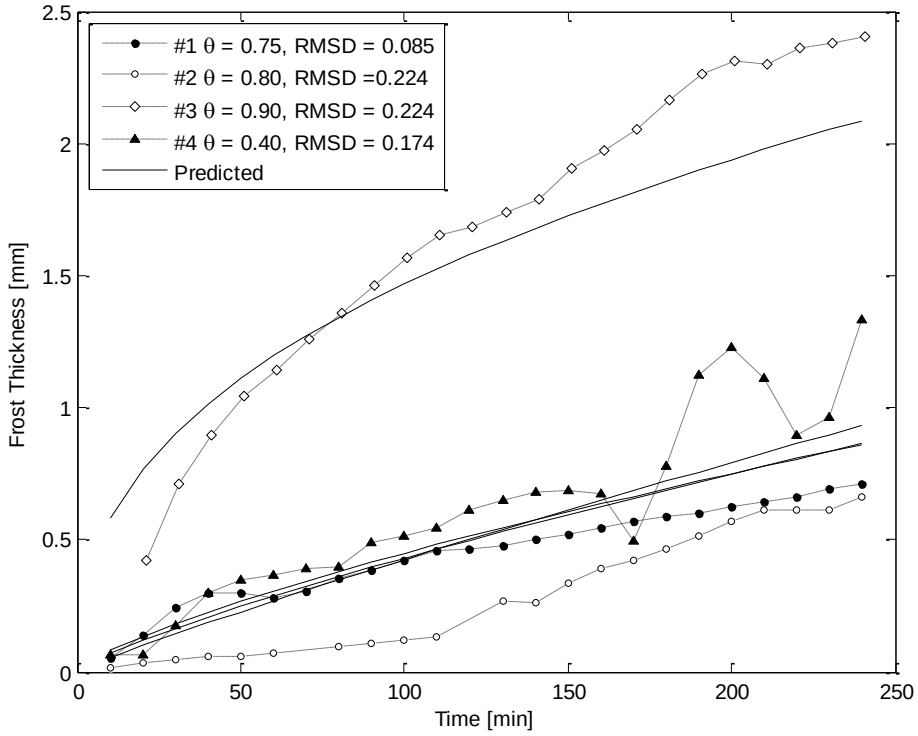

Figure 46. Comparison of correlation to experimental data.

It is observed in experimental data that K decays asymptotically over time for a given set of conditions. Therefore by calculation of K at the final data point in the data sets when K has decayed significantly and plotting it versus θ for each case, the relationship K(θ) can be obtained. This result is shown in Figure 45. The trend of the line is best fit by a power law relation, which is given by Eq. (5.4). Insertion into the correlation yields Eq. (5.5).

$$K(\theta) = 0.0045\theta^{-4.271}. \tag{5.4}$$

$$\delta(t) = 0.0045\theta^{\theta-4.721}t^{\theta}. \tag{5.5}$$

Figure 46 shows the correlation as compared to the thickness data from runs 1 through 4. The relative error is calculated for each using the root mean square deviation method (**Error! Reference source not found.**) and is listed in Figure 46. The fit is reasonably close for three of the cases, but the correlation tended to over predict for run 2.

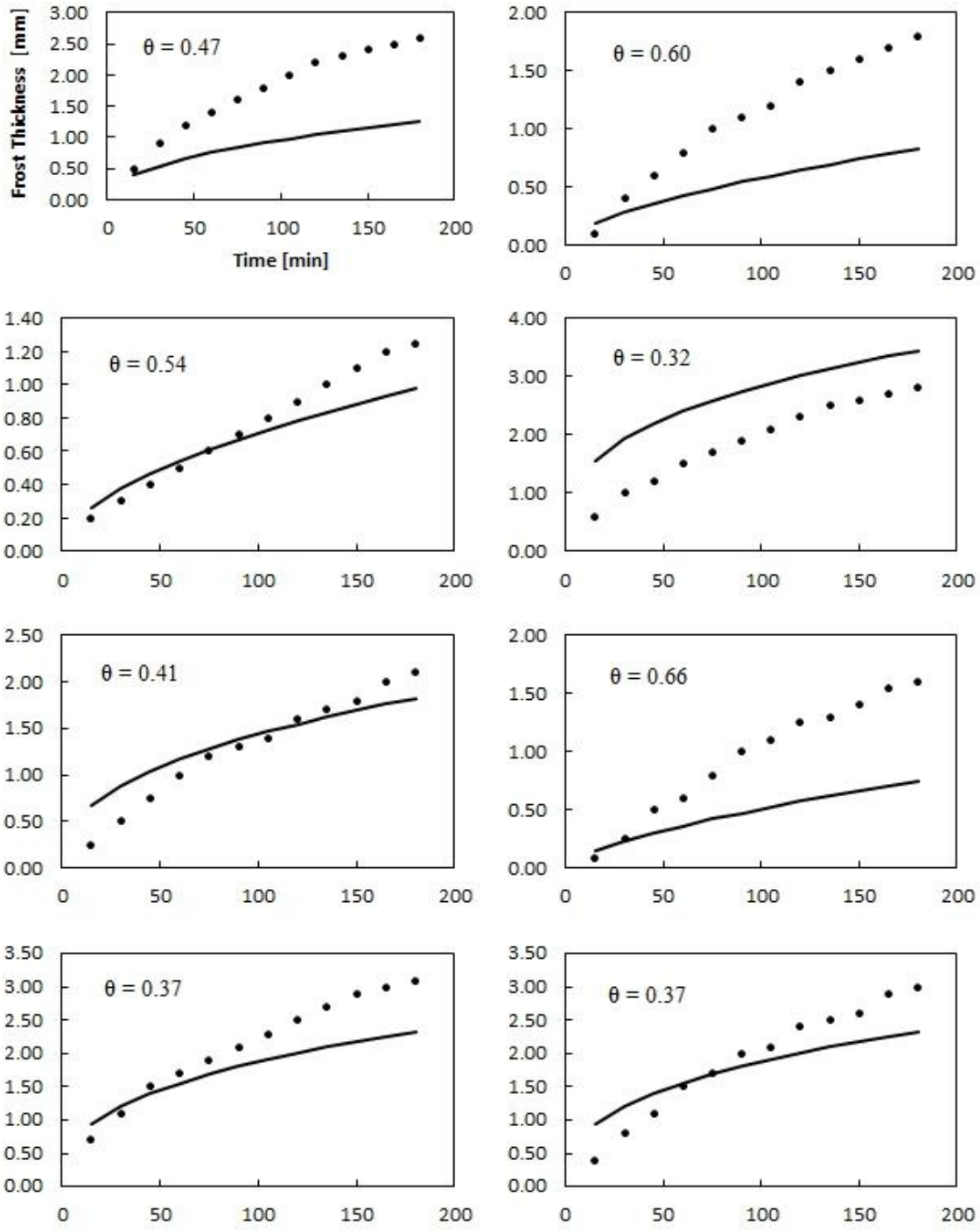

Figure 47. Comparison of proposed correlation to data from Lee and Ro [22]. Solid line indicates predicted values.

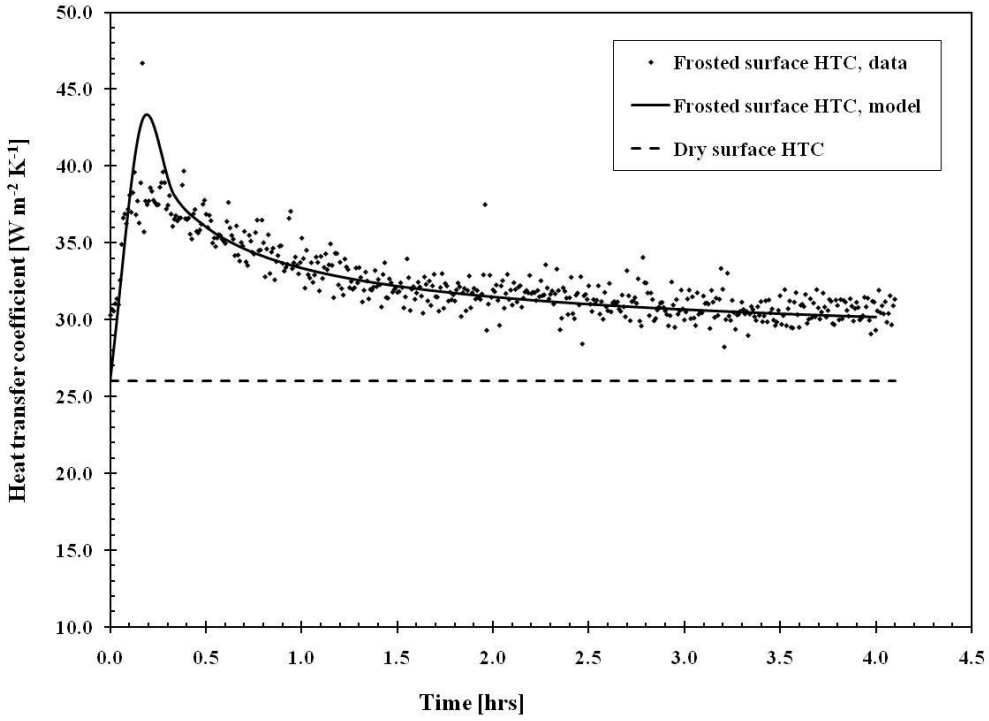

Figure 48. Heat transfer coefficient (including latent effects) based on the proposed thickness correlation as determined by Mohs [29].

The change appears the result of the change in air temperature between runs 1 and 2 without a significant change in other parameters, which has caused a change in θ even though the growth rate is not largely different. The results indicate that more information is needed to fully quantify the growth behavior. Additionally, Eq. (5.5) yields only moderate accuracy when applied to experimental data from other experiments, which is due in part to the small data set used for development and also the exclusion of other parameters.

Figure 47 shows Eq. (5.5) plotted against experimental thickness data sets obtained by Lee and Ro [22], which illustrates this observation. In some cases, reasonable agreement is shown. However, particularly when θ nears values less than 0.4, rather large errors occur. A model based on a broader data set may help to improve accuracy throughout the spectrum of θ.

Despite this uncertainty, Mohs [29] has demonstrated that the proposed thickness model (Eq. (5.5)) can be used to determine mass transfer rates and the resulting total heat transfer coefficients that agree well with experimental data. Mohs has presented Figure 48 as an illustration of this agreement. Equation (5.5) has been shown here to produce reasonable results over mid-range values of θ. However a refined model is required to capture the behavior of frost growth under more extreme conditions.

To address the poor fit of Eq. (5.5) under certain conditions, a new correlation was developed and the fitment was based on data from 5 different resources (including the data used for Eq. (5.5)). The form of the new equation is somewhat different. Several different types of equations were tested, all of which were derived from observation of the experimental data under different conditions. The most appropriate result, given the tendency of frost growth to decay over time, was found to be an exponential model as opposed to the more commonly applied power law model which is found in the majority of available correlations.

The exponential model yielded the most accurate results of any of the applied forms. To improve the accuracy of the correlation under extreme conditions, an additional weighting factor of specific humidity is introduced, so that the function depends on θ, t, and ω. Consider an equation of the form,

$$\delta(t) = A\omega^{n}\exp\left[\frac{-B}{t^{\theta}}\right]. \tag{5.6}$$

Equation (5.6) is chosen since the behavior of many physical systems has been shown to be of a similar form. In many cases the general solution to governing equations is an exponential decay over one dimension whose exact form is determined by the differential equations. In this case the governing equations are not solved. Rather by observation of the physical phenomenon and experimental data, Eq. (5.6) is presented as a possible descriptor.

It is further assumed that the coefficients A and B will be functions of θ to improve accuracy, but the exponent n is fixed for simplification. Unlike the power law model, the coefficients A and B are not solved for directly. Instead, polynomial forms are assumed, and an iterative solver is used to adjust coefficients until the root mean square deviation is minimized.

Initially data ranging from $\theta = 0.1$ up to $\theta = 0.9$ was included in a single fit. However it was found that owing to the lack of information included in Eq. (5.6), the fit was greatly improved by splitting the range of θ into two categories, and determining A, B and n separately for each category. Reasonable accuracy is obtained when one category includes $\theta \geq 0.4$, corresponding to less extreme growth rates, and $\theta < 0.4$, corresponding to accelerated growth conditions. In the first case, the exponent n is set to zero for simplification. For the accelerated case, n is included as a weighting factor to improve accuracy. The coefficients A and B are determined by eighth degree polynomials for accuracy of fit of the form,

Table 13. Coefficients for 8th degree polynomials representing A and B.

$\theta \leq 0.4$,	n = 0			$\theta < 0.4$,	n = 0.84		
A		**B**		**A**		**B**	
a	-760.57	**j**	1763	**a**	74834	**j**	317.27
b	6293	**k**	-8712	**b**	-719138	**k**	-5983
c	-16594	**l**	6676	**c**	1930329	**l**	34996
d	6725	**m**	18144	**d**	-127372	**m**	-50899
e	36834	**n**	-4089	**e**	-3502574	**n**	-27399
f	-43842	**o**	-30825	**f**	-847.21	**o**	-740768
g	-26220	**p**	-86466	**g**	-46.57	**p**	3640205
h	66019	**q**	214563	**h**	-84.62	**q**	-4207352
i	-28535	**r**	-112137	**i**	-46.20	**r**	-8512

$$A = a + b\theta + c\theta^2 + d\theta^3 + e\theta^4 + f\theta^5 + g\theta^6 + h\theta^7 + i\theta^8,$$
$$B = j + k\theta + l\theta^2 + m\theta^3 + n\theta^4 + o\theta^5 + p\theta^6 + q\theta^7 + r\theta^8. \quad (5.7)$$

Table 13 gives coefficients for Eqs. (5.7) as determined by iteration and the exponent n. This data set gives the most accurate fit, but it is inconvenient to work with as a result of the large number of defining coefficients. Using Eqs. (5.7), Eq. (5.6) is plotted against the same data set used for the first correlation, which is shown in Figure 49. The large improvements in accuracy over Figure 46 are clear. Predicted trends match up well and the root mean square deviation is greatly reduced. Additional comparisons are made to data from Lee and Ro [22], Cheng and Shiu [5], and Fossa and Tanda (2010) [7]. It is evident from Figures 50 to 52 that the exponential model is a much better fit over a wide range of conditions. This is reinforced by Figure 53, which shows the predicted versus actual frost thicknesses for the full set on both conditions. The fit is reasonably good especially given that the correlation is based only on θ and ω.

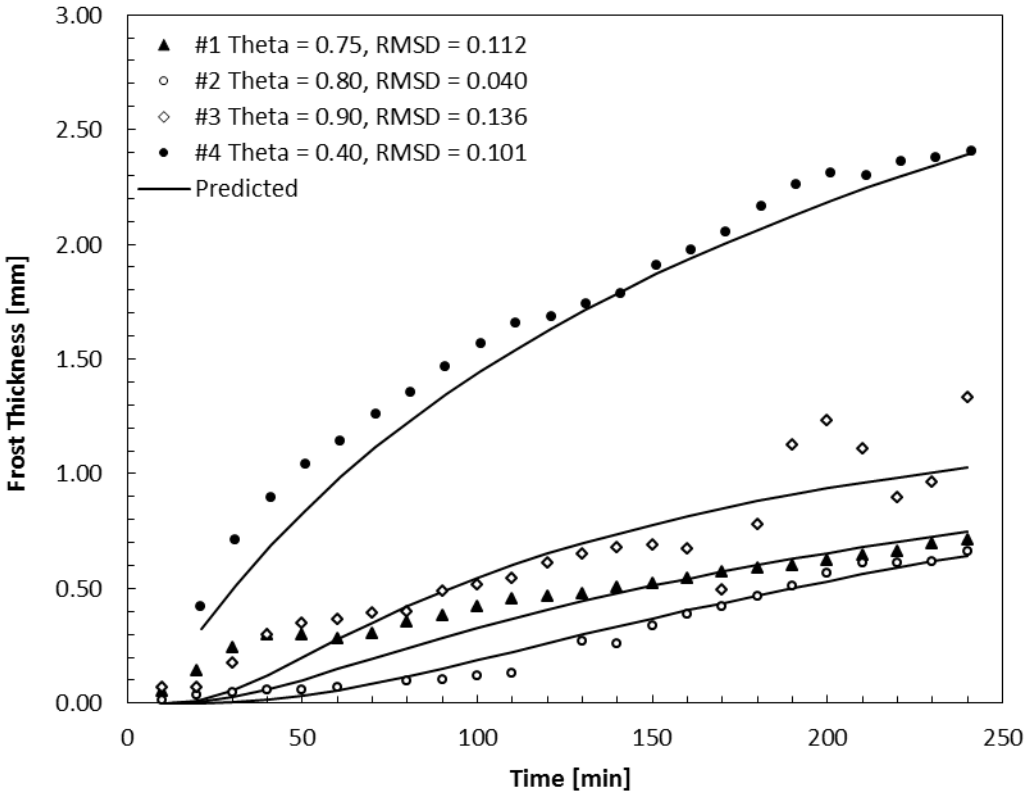

Figure 49. Comparison of exponential correlation to experimental data.

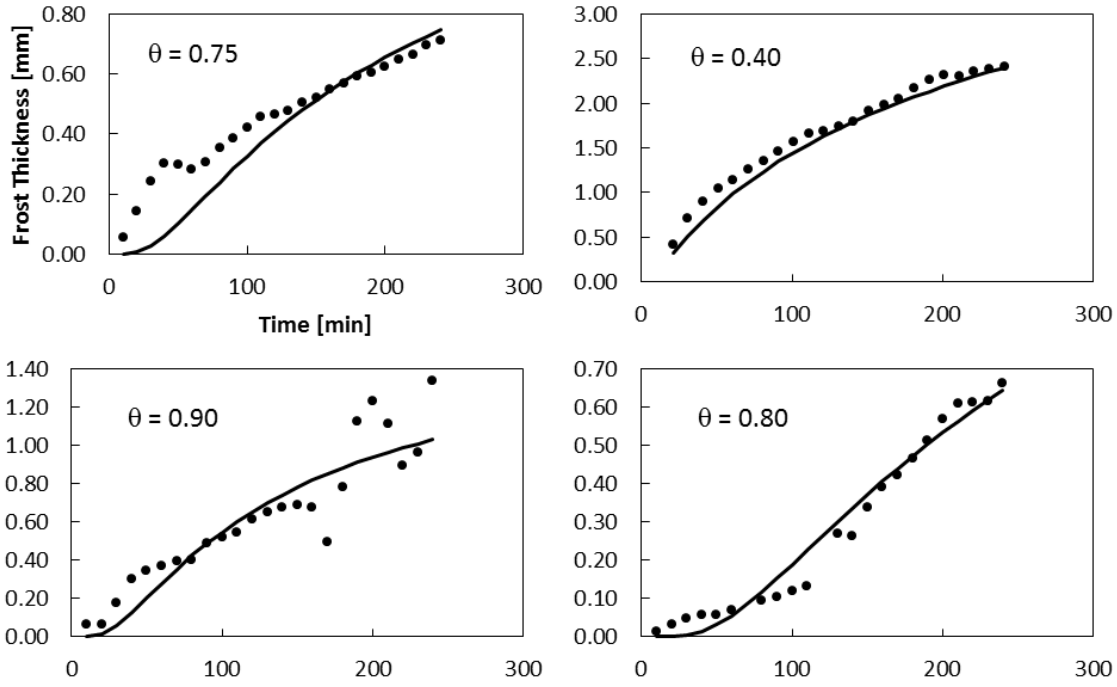

Figure 50. Exponential correlation plotted over experimental data. Solid line indicates predicted values.

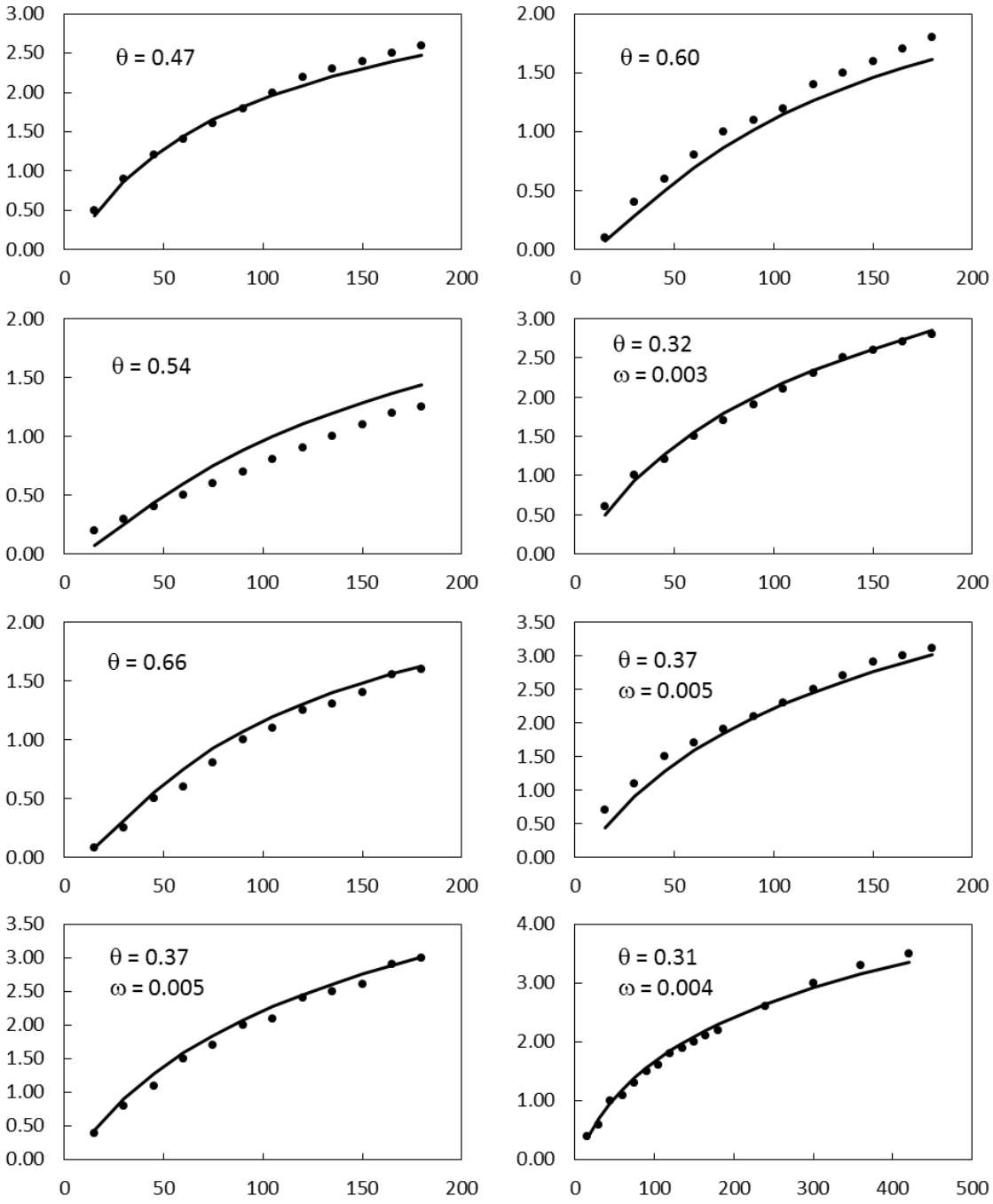

Figure 51. Exponential correlation plotted over data from Lee and Ro [22]. Solid line indicates predicted values.

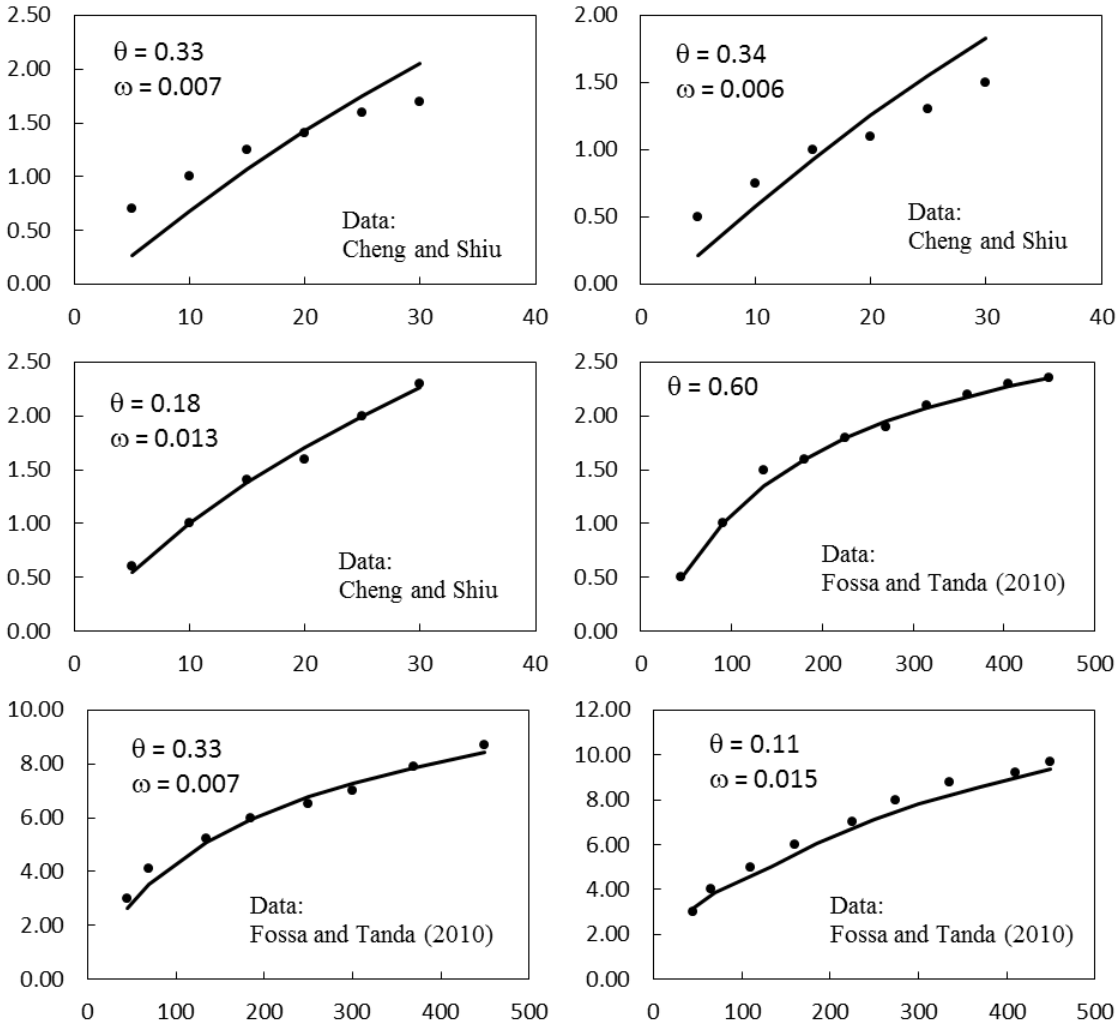

Figure 52. Exponential correlation plotted over data from Cheng and Shiu [5] and Fossa and Tanda [8]. Solid line indicates predicted values.

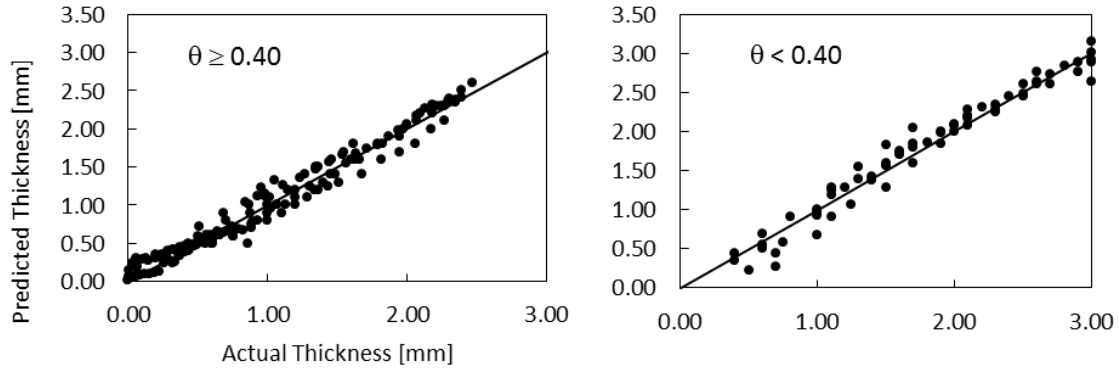

Figure 53. Data fits for full set. Lines are 1:1.

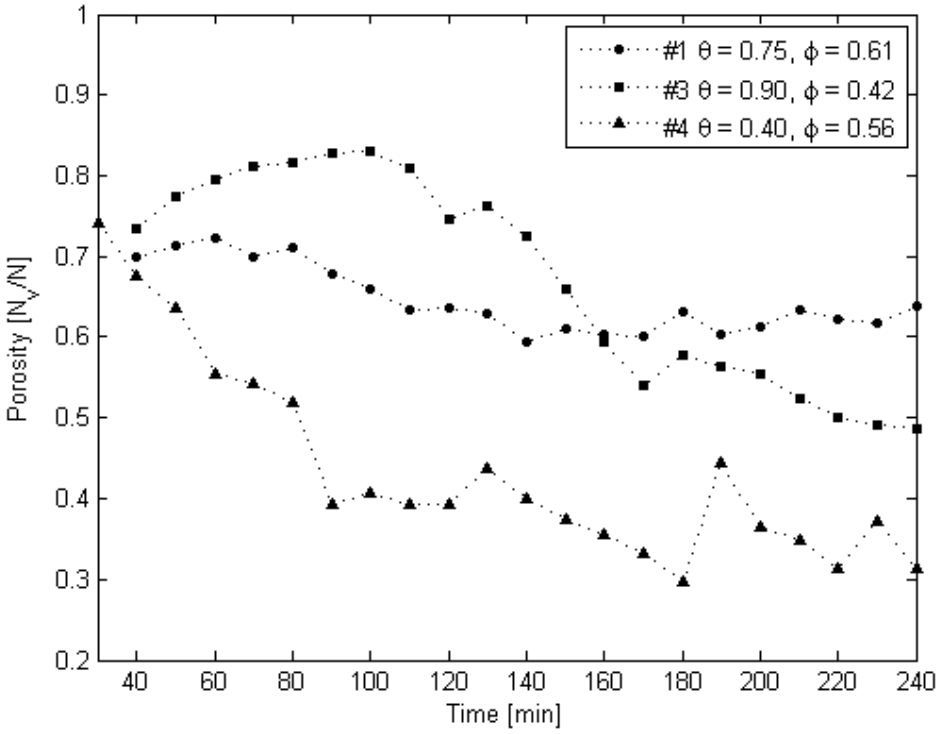

Figure 54. Calculated porosity for three testing conditions.

5.2 Porosity Measurement

Frost porosity is obtained via the image reduction procedure described in section 3.3.3. To reduce error associated with slightly different lighting conditions, the contrast of each image was enhanced so that its darkest areas were always represented by 0 and its lightest by 255 prior to the black and white conversion.

The porosity was determined as a function of time for three different cases (cases 1, 3 and 4 from above) and plotted in Figure 54. It is clear that significant data scattering exists, which is attributed to both changes in lighting and variations in crystal structure. Because the method requires that porosity be determined by discrete categorization of pixels, slight changes in either lighting or structure could cause large numbers of pixels to jump from not being counted to being counted and contributing to the data scatter. It is difficult to overcome this issue, since the discretization is a necessary step in the process.

What appear to be increases in porosity in the earlier times are due to parts of the test surface showing through the small crystals. These areas are typically counted as filled pixels, and the porosity appears to increase as frost growth continues, replacing those pixels with void space. The result is that the porosity curve is only accurate after it reaches a peak where the most

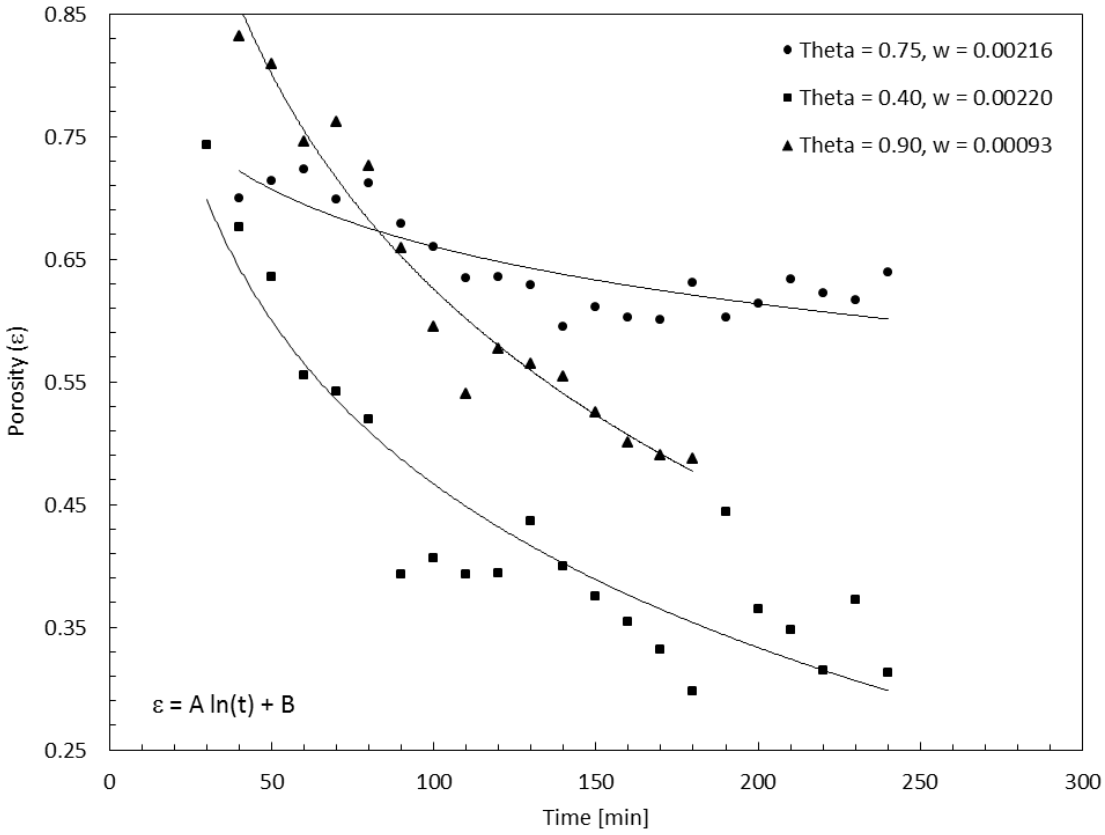

Figure 55. Trend of porosity changes over time.

is detected. Following that peak, the voids are filled in slowly and the porosity decreases.

Even with such variations in data, it is clear that the porosity tends to decay logarithmically, as illustrated in Figure 55. The data in Figure 55 has been clipped at the peak porosity, so that only the accurate regions are included. While correlations for frost porosity are not typically presented in frost growth literature, it is proposed here that the changes in porosity are most nearly approximated by a logarithmic decay of the form of given in Eq. (5.8),

$$\varepsilon_a = f_1(\theta)\ln(t) + f_2(\theta). \tag{5.8}$$

The functions f_1 and f_2 are intended to capture the dependence of porosity changes on the growth conditions. These functions must be determined based on experimental data. Because it is rare to find porosity data included in literature and because of the small data set available from the experiments described here, these functions have not yet been determined.

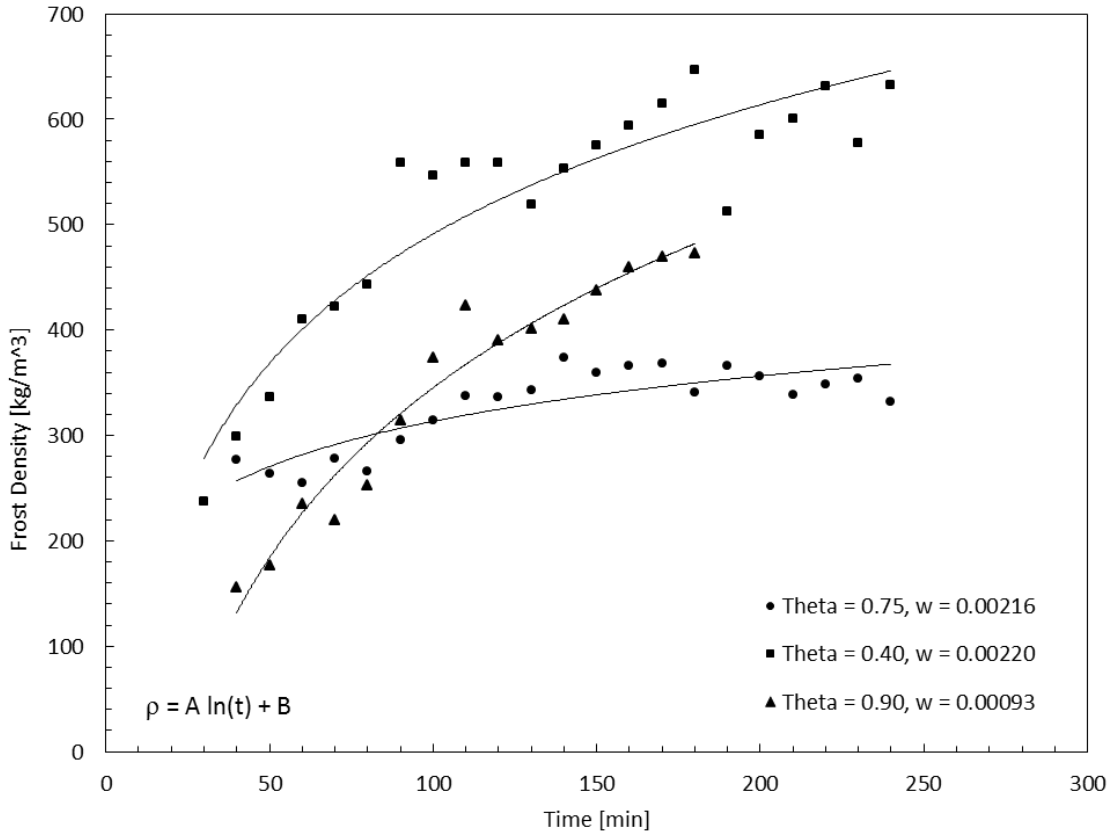

Figure 56. Frost density over time estimated by porosity.

Frost density can be obtained by the application of Eq. (3.16), and the result is shown in Figure 56, where the density is seen to grow as the inverse of porosity. Given the inverse relationship, density growth is also found to be best modeled by a logarithmic curve described by Eq. (5.9) Again, the functions f_3 and f_4 are not yet determined.

$$\rho_f = (1-\varepsilon_a)\rho_i + \varepsilon_a\rho_a. \tag{3.16}$$

$$\rho_f = f_3(\theta)\ln(t) + f_4(\theta). \tag{5.9}$$

The logarithmic model gives a good fit. However at early times it is physically unrealistic because porosity must be bounded by unity at t = 0. Therefore, it is clear that Eqs. (3.16) and (5.9) can only be applied after the early growth phase has occurred.

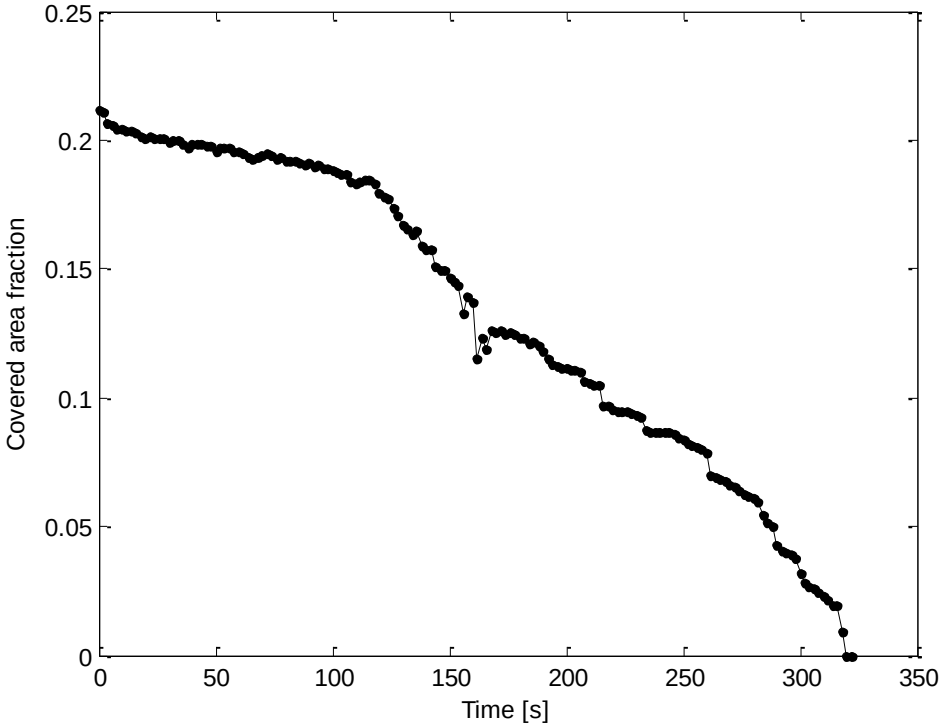

Figure 57. Area fraction of test surface covered by water during defrosting.

5.3 Droplet size analysis

The droplet analysis method was used to determine droplet area fractions and perimeters during the defrosting process. A typical result is shown in Figure 57, where the area fraction of the image area covered by water decreases with time. Small variations can be observed which are due again to the discretization process, but the analysis still clearly shows the trend. The rate of area reduction increases as the droplet becomes smaller, as a result of an increasing surface area to volume ratio.

Figure 58 shows the average droplet perimeter during defrosting. The trend contains large jumps as a result of the averaging process. The average drop perimeter is calculated as the total perimeter of all drops divided by the number of drops. Thus when a drop evaporates completely the average experiences a step change. To reduce this effect, the image size used for analysis could be increased so that more drops are included in the field of view.

An in depth analysis of the defrosting is not given here, as the primary focus is on the use of image acquisition for determining droplet area and perimeter. For an analysis of the defrosting process, refer to Mohs [29].

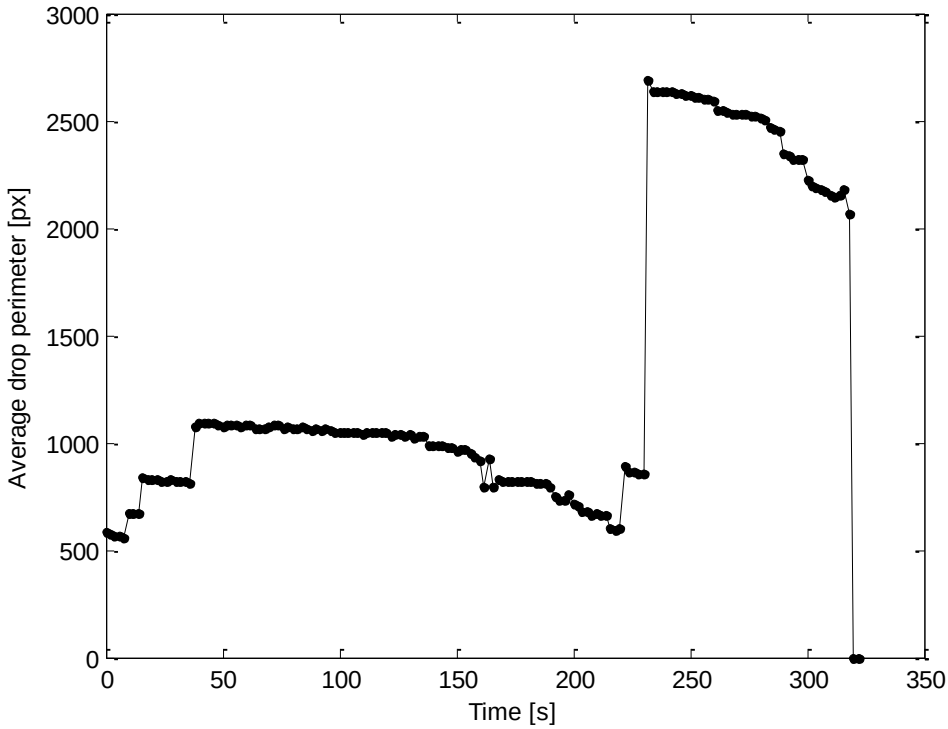

Figure 58. Average droplet perimeter during defrosting.

5.4 Analysis of image acquisition methods

As shown in the preceding section, measurements obtained via the image acquisition techniques outlined in chapter 3 have both significant advantages, as well as some disadvantages when compared to traditional measurements. The primary advantage to such techniques is accuracy and speed of computation, which allow for improved frost growth models and the ability to easily measure parameters like droplet geometry and frost layer porosity. The major downfall to the use of those methods is the need for highly accurate calibration. This is a pitfall which can be mostly avoided with proper preparation, however.

From the standpoint of experimental accuracy and data analysis, the computer based measurement methods give an improvement over more traditional methods. Continued development of the techniques would surely yield strategies for further reducing possible sources of error and obtaining even more accurate results.

6 Conclusion

6.1 Concluding Remarks

The process of frost growth has shown itself to be one of great complexity. Subtleties of the natural and inseparable relationship between the heat and mass transfer manifest themselves in the difficulty of deriving experimental relationships applicable to wide ranges of conditions, and the intricacy of governing equations themselves hint at inner workings which we have not yet found ways of analyzing.

Over the last few decades, experimental conditions and systems used to study frost growth have varied widely, from full evaporator coil testing in wind tunnels to very small and flat test surfaces exposed to ambient air. The choice of a test setup depends greatly on the desired outcomes of the experiment, but it is apparent that smaller systems are typically able to produce more controlled conditions and reliable results. Other important factors include test surface geometry and orientation, cooling method and techniques for frost property measurement.

Experimentation carried over a variety of environmental conditions has provided some insight as to primary parameters that can be used to understand and help predict frost growth in many different cases. In most cases these parameters appear to be the thermodynamic properties of the frost layer, the psychometric conditions near the frosting surface, and the temperature of the cold surface itself. Where forced convection is used, the Reynolds number is also an important factor.

Many correlations intended to predict frost growth and properties have been based on various combinations of the important parameters, but relatively few have been developed according to the apparent physics of the frosting process. A notable example is the LeGall [20] correlation for thermal conductivity, which has given consideration to the ice crystal orientation. In most cases, correlations are power law curve fits of multiplied parameters. Here, a thickness correlation is proposed which is based on the observation of experimental data as well as some consideration for the physical phenomenon.

Currently, there is some limitation on the size and accuracy of data sets used for the development of such correlations. It has been shown that the possibility exists for significantly different results to be obtained depending on which measurement methods are used, which leaves the combination of data between different experiments with large amounts of uncertainty. With improved experimental methods, this uncertainty could be largely reduced and more precise correlations spanning a wider range of conditions could be developed. In the meantime, numerical solutions have yielded good results.

In the continually expanding study of frost growth, new experimental methods have the potential to help spur progress forward by improving data accuracy and providing new opportunities. One of the largest factors that has changed research over the last twenty years is the development of both computer based data acquisition hardware and software. The possibility of using modern software combined with high resolution image acquisition to obtain highly accurate measurements of frost properties such as thickness, porosity, and droplet geometry is investigated here and compared to traditional methods.

The uncertainty associated with computer based measurement methods can be either large or very small, depending on the calibration of the system. It follows that the methods proposed here have the capability to greatly improve the accuracy of thickness measurement, and with care porosity. In addition to thickness and porosity, droplet geometry measurements can be made accurately and quickly so that the physical behavior of the system during defrosting can be analyzed. Mohs [29] has used these methods to aid in the study of the defrosting process, an area which has until now seen little research.

As the field of frost research continues to progress, further development of computer based methods will no doubt improve the accuracy of results and make it possible to combine wide ranges of data for analysis, not only in frost research but in many fields. As our technological capability evolves, so does our potential to unveil scientific principles fundamental to our development, within which we find the ability to shape the world around us and exact upon it our will to advance.

6.2 Summary of Results

1. Small scale experiments are growing in popularity owing to improved control and accuracy. Flat plate geometries are preferable over full sized evaporator coils.
2. Many experimental methods have remained somewhat undeveloped over the years. It is possible to improve the accuracy and speed of measurement greatly by the use of computer based algorithms.
3. Faster and more accurate measurements provide a wider range of data which is required for the evolution of the field from a basic understanding to more complex view.
4. By making use of large and accurate data sets, the reliability of current frost growth correlations can be greatly improved. As an example, a correlation is presented which is able to predict thickness with reasonable accuracy in a wide range of conditions.

7 Future work

There are many possibilities for future development of the computer measurement methods, particularly with regard to instrument calibration techniques. For measurements like porosity, some difficulty is encountered because of the change in crystal structure over time and slight variations in lighting. Additionally, as the frost interface moves forward towards the camera some error in resolution scaling will be introduced.

An improved experimental setup would make it possible to acquire more information. A refinement of the mass measurement system to make it suitable for continuous measurement would be advantageous. The method initially proposed here was prone to serious vibration, which invalidated the results. A possible solution is the water and desiccant measurement method which was used as an alternative, described in section 3.3.

The use of a double layered testing chamber would be a significant improvement. The reason for this is that by setting the temperature in the bounding layer equal to the interior temperature, the heat leakage to the interior chamber could be mostly eliminated (if the bounding layer cooling system was appropriately designed). This would improve the reliability of heat flux measurements and help with calibration. Some system for measurement of the air-frost interface temperature should also be included, since it is an important parameter. A built in infrared sensor, if properly calibrated, should yield accurate results.

Room for improvement also exists in the area of image analysis. As of yet, it is somewhat difficult to enable automatic calculations on multiple images for measurements of thickness because of variations in lighting and structure. To ensure that the correct boundaries are captured on each image, the measurements are made individually and the code is adjusted appropriately. An algorithm capable of an automated loop which could correct for such changes would speed up data analysis and remove some element of human judgment.

Wider ranges of conditions should be tested so that correlations can be developed from data sets of known accuracy over many different conditions. The proposed improvements in test chamber design would make this possible. The inclusion of time dependent mass and interface temperature would yield more parameters for potential analysis.

A full numerical model of the system would be highly beneficial for comparison to results and correlations. Such modeling can be achieved via a finite difference approach to the governing equations, as demonstrated by Chen et al. [3] with good accuracy. A more in depth analysis of the test chamber itself could be performed with software like ANSYS. An attempt is made here (0), but it is clear that for reasons of accuracy, more exact chamber properties are a requirement. Such an analysis could be used to improve the chamber design.

References

[1] Auracher, H., 1987, "Effective Thermal Conductivity of Frost," *Proceedings of the International Symposium on Heat and Mass Transfer,* Dubrovnik, pp. 285-301.

[2] Brian, P. L. T., R. C. Reid, and Y. T. Shah, 1970, "Frost Deposition on Cold Surface," Industrial Engineering Chemistry Fundamentals, 9, pp. 375-380.

[3] Chen, Hong, L. Thomas, and R. W. Besant, 2001, "Modeling Frost Characteristics on Heat Exchanger Fins: Parts I and II (Numerical Model and Experimental Validation)," ASHRAE Transactions: Research, 106, pp. 357-76.

[4] Chen, Ruiqiu, J. Tian, and X. Hou, 2007, "An Experiment Study of the Heat-Transfer Performance of Finned-Tube Evaporator Under Low Temperature Frosting Conditions," *Proceedings*, International Congress of Refrigeration, Beijing, ICR07-B2-552.

[5] Cheng, Chin-Hsiang, and C-C. Shiu, 2002,"Frost Formation and Frost Crystal Growth on a Cold Plate in Atmospheric Air Flow," International Journal of Heat and Mass Transfer, 45, pp. 4289-4303.

[6] Cremers, C. J., and V. K. Mehra, 1980, "Frost Formation in Vertical Cylinders in Free Convection," Paper WA/HT 80(22), American Society of Mechanical Engineers, New York.

[7] Fossa, Marco, and G. Tanda, 2010, "Frost Formation in Vertical Channels under Natural Convection," International Journal of Multiphase Flow, 36, pp. 210-220.

[8] Fossa, Marco, and G. Tanda, 2001, "Study of Free Convection Frost Formation on a Vertical Plate," Experimental Thermal and Fluid Sciences, 26, pp. 661-68.

[9] Fox, R. W., A. T. McDonald, and P. J. Pritchard, 2008, *Introduction to Fluid Mechanics*, 7th ed., Appendix A-3, pp. 721, John Wiley, Hoboken.

[10] Gathilor, T. S., and V. S. Ivanova, 1979, "Characteristics of the Frost Formed on the Surface of Finned Air Coolers, *Proceedings,* XV Congress of Refrigeration, Venice, pp. 62-71.

[11] Getu, H. M., and P. K. Bansal, 2007, "Limitations of Existing Frost Property Correlations," *International Congress of Refrigeration*, Beijing, ICR07-E1-343.

[12] Hao, Y. L., Y. X. Tao, J. Iragorry, and D. Castro, 2003, "Experimental Study and Modeling of Frost Formation on Various Surface Under Nature Convection," *Proceedings*, ASME International Mechanical Engineering Congress and R&D Exposition, Washington, IMECE2002-32797.

[13] Hayashi, Y. A., A. Aoki, S. Adachi, and K. Hori, 1977, "Study of Frost Properties Correlating with Frost Formation Types," Journal of Heat Transfer, 99(2), pp. 239-245.

[14] Incropera, F. P., and D. P. DeWitt, 2007, *Introduction to Heat Transfer*, 5th ed., J. Wiley, New York.

[15] Iragorry, J., and Y. X. Tao, 2004, "Frost Temperature Relations for Defrosting Sensing Systems," *Proceedings*, ASME Heat Transfer/Fluids Engineering Summer Conference, Charlotte, HT-FED2004-56074.

[16] Iragorry, J., Y-Xi. Tao, and S. Jia, 2004, "A Critical Review of Properties and Models for Frost Formation Analysis," HVAC&R Research, 10(4), pp. 393-420.

[17] Kolunin, V. S., 2005, "Heat and Mass Transfer in Porous Media with Ice Inclusions near the Freezing-point," International Journal of Heat and Mass Transfer, 48, pp. 1175-1185.

[18] Kondepudi, S. N., O'Neal, D.L., 1987, "The Effects on Frost Growth on Extended Surface Heat Exchanger Performance: a Review," ASHRAE Transactions, 93(2), pp. 258-274.

[19] Lazzarin, R., and D. Nardotto, 2010, "Study of Frost Growth on an Air Heat Pump Outside Coil," *Proceedings*, Sustainable Refrigeration and Heat Pump Technology Conference, Stockholm, VCH-6.

[20] Le Gall, R., J. M. Grillot, and C. Jallut, 1997, "Modeling of Frost Growth and Densification," International Journal of Heat and Mass Transfer, 403(13), pp. 4359-4365.

[21] Lee, K. S., T. H. Lee, and W. S. Kim, 1994, "Heat and Mass Transfer of Parallel Plates Heat Exchanger under Frosting Condition," SAREK Journal, 6, pp. 155-165.

[22] Lee, Y. B., and S. T. Ro, 2002, "Frost Formation on a Vertical Plate in Simultaneously Developing Flow," Experimental Thermal and Fluid Sciences, 26, pp. 939-945.
[23] Lee, Yoon Suk, Y S. Hyuk, H. Gaku, and K. Cho, 2010, "Frost Properties on the Fin and Tube Under Heat Pump Condition," *Proceedings*, Sustainable Refrigeration and Heat Pump Technology Conference, Stockholm, VCH-8.
[24] Liang, Cai, Hou Puxiu, and Yu Weiping, 2007, "Experiment Study on Initial Stages of Frost Growth on Different Character Surface," *International Congress of Refrigeration*, Beijing, ICR07-B1-317.
[25] Liu, Zhiqiang, H. Zhu, and H. Wang, 2005, "Study on Transient Distributed Model of Frost on Heat Pump Evaporator," Journal of Asian Architecture and Building Engineering, 4(1), pp. 265-270.
[26] Mao, Y., R. W. Besant, and H. Chen, 1999, "Frost Characteristics and Heat Transfer on a Flat Plate under Freezer Operating Conditions: Part I, Experimentation and Correlations," ASHRAE Transactions, 105(2), pp. 231-251.
[27] Mao, Y., R. W. Besant, and K. S. Rezkallah, 1991, "A Method of Measuring Frost Density Using Flush-mounted Removable Disks," ASHRAE Transactions, 97(1), pp. 26-30.
[28] Mao, Y., R. W. Besant, and K. S. Rezkallah, 1992, "Measurement and Correlations of Frost Properties with Airflow over a Flat Plate," ASHRAE Transactions, 98(2), pp. 65-77.
[29] Mohs, W.F., 2011, " Heat and Mass Transfer during the Melting Process of a Porous Frost Layer on a Vertical Surface" Unpublished doctoral dissertation, University of Minnesota Twin Cities, Minneapolis.
[30] Ngonda, T. N., and T. J. Sheer, 2007, "Frost Formation on a Cooling Coil in Supersaturated Supply Air," *Proceedings*, International Congress of Refrigeration, Beijing, ICR07-B2-151.
[31] Sanders, C. T., 1974, "The Influence of Frost Formation and Defrosting on the Performance of Air Coolers," Thesis, Delft Technical University, Delft.
[32] Schneider, H. W., 1978, "Equation of the Growth Rate of Frost Forming on Cooled Surfaces," International Journal of Heat and Mass Transfer, 21(8), pp. 1016-1024.
[33] Shin, J., A. V. Tikhonov, and C. Kim, 2003, "Experimental Study on Frost Structure on Surfaces with Different Hydrophilicity: Density and Thermal Conductivity," Journal of Heat Transfer, 125(1), pp. 84-94.
[34] Thomas, L., H. Chen, and R. W. Besant, 1999, "Measurement of Frost Characteristics on Heat Exchanger Fins," ASHRAE Transactions, 105(A), pp. 283-293.
[35] Xia, Yanping, and A. M. Jacobi, 2005, "Air-side Data Interpretation and Performance Analysis for Heat Exchangers with Simultaneous Heat and Mass Transfer: Wet and Frosted Surfaces," International Journal of Heat and Mass Transfer, 48, pp. 5089-5102.
[36] Yamashita, K., M. Hamada, S. Ise, and H. Ohkubo, 2007, "Study of Frost Properties in a Low Temperature Environment," Proceedings, International Congress of Refrigeration, Beijing, ICR07-B2-809.
[37] Yonko, J. D., and C. F. Sepsy, 1967, "An Investigation of the Thermal Conductivity of Frost While Forming on a Flat Horizontal Plate," ASHRAE Transactions, 73(1), pp. 1.1-1.11.
[38] Youbi-Idrissi, M., and J. Guilpart, 2007, "Refrigerating System Performances Under Frosting Conditions: Predictive Model & Experimental Validation," *Proceedings*, International Congress of Refrigeration, Beijing, ICR07-B2-268.
[39] Zhou, Xiaotang, J. E. Braun, and Q. Zeng, 2007, "An Improved Method for Determining Heat Transfer Fin Efficiencies for Dehumidifying Cooling Coils (RP-1194)," HVAC&R Research, 13(5), pp. 769-783.
[40] Özişik, M. Necati, 1993, *Heat Conduction*, 2nd ed., John Wiley & Sons, New York.

Appendix A

Derivation of equations from all sections

A.1 Derivation of Eq. (3.49)

The convection coefficient is described by Eqs. (A.1) and (A.2). Application of the error formula yields Eqs. (A.1) to (A.3) if A is treated as a constant.

$$\bar{h} = A\left(\frac{(T_a - T_c)(s + T_a)^2}{T_a^{\,6}}\right)^{1/4}, \tag{B.10}$$

$$A \equiv \left(\frac{4m(Pr)k}{3L}\right)\left(\frac{gP^2L^3}{4(bR)^2}\right)^{1/4}, \tag{B.11}$$

$$\Delta\bar{h} = \Delta T\sqrt{\left(\left|\frac{\partial\bar{h}}{\partial T_a}\right|^2 + \left|\frac{\partial\bar{h}}{\partial T_c}\right|^2\right)}. \tag{B.12}$$

The derivatives of Eq. (B.12) are,

$$\frac{\partial\bar{h}}{\partial T_a} = -\frac{A(s + T_a)\left(5sT_a + 3T_a^{\,2} - 6sT_w - 4T_aT_w\right)}{4T_a^{\,5/2}\left[(s + T_a)^2(T_a - T_w)\right]^{3/4}}, \tag{B.13}$$

$$\frac{\partial\bar{h}}{\partial T_c} = -\frac{A\left[(s + T_a)^2(T_a - T_w)\right]^{1/4}}{T_a^{\,3/2}(4T_a - 4T_w)}. \tag{B.14}$$

Square Eqs. (B.13) and (B.14) and add them to obtain Eq. (A.6),

$$\left|\frac{\partial\bar{h}}{\partial T_a}\right|^2 + \left|\frac{\partial\bar{h}}{\partial T_c}\right|^2 = \frac{A^2(s + T_a)^2\left(5sT_a + 3T_a^{\,2} - 6sT_w - 4T_aT_w\right)^2}{16T_a^{\,5}\left[(s + T_a)^2(T_a - T_w)\right]^{3/2}} + \frac{A^2\left[(s + T_a)^2(T_a - T_w)\right]^{1/2}}{T_a^{\,3}(4T_a - 4T_w)^2}. \tag{B.15}$$

Combination of the squared quantities gives Eq (A.7),

$$\left|\frac{\partial \bar{h}}{\partial T_a}\right|^2 + \left|\frac{\partial \bar{h}}{\partial T_c}\right|^2 = \frac{A^2\left[T_a{}^2\left(s+T_a\right)^2 + \left(5sT_a + 3T_a{}^2 - 6sT_w - 4T_aT_w\right)^2\right]}{16T_a{}^5(s+T_a)(T_a - T_w)^{3/2}}. \tag{B.16}$$

Finally, substation into Eq. (B.12) yields Eq. (A.8), which is identical to Eq. (3.49),

$$\Delta\bar{h} = \Delta T\sqrt{\left(\left|\frac{\partial \bar{h}}{\partial T_a}\right|^2 + \left|\frac{\partial \bar{h}}{\partial T_c}\right|^2\right)} = \Delta T\sqrt{\frac{A^2\left[T_a{}^2\left(s+T_a\right)^2 + \left(5sT_a + 3T_a{}^2 - 6sT_w - 4T_aT_w\right)^2\right]}{16T_a{}^5(s+T_a)(T_a - T_w)^{3/2}}},$$

$$\Delta\bar{h} = \frac{A\Delta T}{4}\frac{\left[T_a{}^2\left(s+T_a\right)^2 + \left(5sT_a + 3T_a{}^2 - 6sT_w - 4T_aT_w\right)^2\right]^{1/2}}{T_a{}^{5/2}(s+T_a)^{1/2}(T_a - T_w)^{3/4}}. \tag{B.17}$$

A.2 Derivation of Eqs. (4.3) to (4.5)

The constant applied heat flux problem outlined in section 4.3 is given by Eqs. (A.9). The problem splitting method is outlined in more detail in Özişik [40].

$$\frac{\partial^2 T}{\partial x^2} = \frac{1}{\alpha}\frac{\partial T}{\partial t},$$

$$\begin{aligned} -k\frac{\partial T}{\partial x} &= q'', && x = 0,\ t > 0, \\ \frac{\partial T}{\partial x} + HT &= HT_\infty, && x = L,\ t > 0, \\ T(x,t) &= T_0, && 0 \le x \le L,\ t = 0. \end{aligned} \tag{B.18}$$

The first step is to split the problem into a steady state problem which will capture the inhomogeneous boundary conditions and a homogeneous problem to be solved for transient effects. For the steady state problem, time derivatives are zero. The problem is reduced to Eq. (A.10) with the boundary conditions Eqs. (A.11), where T_c is the cold surface temperature located at x = L.

$$\frac{\partial^2 T_{ss}}{\partial x^2} = 0, \tag{B.19}$$

$$\begin{aligned} -k\frac{\partial T_{ss}}{\partial x} &= q'', & x &= 0, \\ T_{ss} &= T_c, & x &= L. \end{aligned} \tag{B.20}$$

Integration of Eq. (B.19) and solution of the constants gives Eq. (A.12),

$$T_{ss}(x) = \frac{q''}{k}[L - x] + T_c. \tag{B.21}$$

The temperature T_c can be related to the convection coefficient, heat flux and ambient temperature by application of an energy balance at the test surface. This balance gives Eq. (A.13) with the heat flux assumed to be constant throughout the assembly,

$$k\frac{\partial T}{\partial x}\bigg|_{x=L} = q'' = h(T_c - T_\infty). \tag{B.22}$$

Upon rearrangement,

$$T_c = \frac{q''}{h} + T_\infty. \tag{B.23}$$

Substitution of into Eq. (B.21) gives the steady state temperature distribution, Eq. (A.15),

$$T_{ss}(x) = q''\left[\frac{(L - x)}{k} + \frac{1}{h}\right] + T_\infty. \tag{B.24}$$

The transient problem is solved by re-writing Eq. (B.18) in its homogeneous form, Eq. (A.16), where the boundary conditions are then given by Eqs. (A.17),

$$\frac{\partial^2 T_h}{\partial x^2} = \frac{1}{\alpha}\frac{\partial T_h}{\partial t} \tag{B.25}$$

$$\frac{\partial T_h}{\partial x} = 0, \qquad x = 0,\ t > 0,$$

$$\frac{\partial T_h}{\partial x} + HT_h = 0, \qquad x = L,\ t > 0, \tag{B.26}$$

$$T_h(x,t) = T_o - T_{ss}, \qquad 0 \le x \le L,\ t = 0.$$

The problem of Eqs. (B.25) and (B.26) can be solved by the separation of variables method, which is outlined only briefly here (see Özişik [40] for details). The assumed form of the solution is Eq. (A.18),

$$T_h(x,t) = X(x)\Gamma(t). \tag{B.27}$$

Substitution into Eq. (B.25) yields two separable ordinary differential equations, given by Eqs. (A.19) and (A.20),

$$\frac{d^2X}{dx^2} + \lambda^2 X = 0, \tag{B.28}$$

$$\frac{d\Gamma}{dt} + \alpha\lambda^2\Gamma = 0. \tag{B.29}$$

The corresponding boundary conditions in the space variable are (from Eqs. (B.26)),

$$\frac{\partial X}{\partial x} = 0, \qquad x = 0,$$

$$\frac{\partial X}{\partial x} + HX = 0, \qquad x = L. \tag{B.30}$$

The solution to Eq. (B.28) is periodic, and that of Eq. (B.30) is exponential,

$$X(x) = c_1\cos(\lambda x) + c_2\sin(\lambda x), \tag{B.31}$$

$$\Gamma(t) = c_3 \exp\left[\alpha\lambda^2 t\right] + c_4 \exp\left[-\alpha\lambda^2 t\right] + c_5. \tag{B.32}$$

By application of the boundary conditions (B.30) to Eq. (B.31), the following results are obtained,

$$\begin{aligned} c_2 &= 0, \\ \lambda \tan(\lambda L) &= H. \end{aligned} \tag{B.33}$$

Thus, the space variable solution is given by Eq. (A.25) and the eigenvalue λ_m by Eq. (A.26), where the subscript m is introduced to denote multiple solutions for λ,

$$X(x) = c_1 \cos(\lambda_m x), \tag{B.34}$$

$$\lambda_m \tan(\lambda_m L) = H. \tag{B.35}$$

Equation (B.32) is reduced by the argument that the transient response of the system must decay over time as steady state conditions will eventually be reached. The implication of this is that $c_3 = c_5 = 0$, as only the c_4 term decays with time. Thus,

$$\Gamma(t) = c_4 \exp\left[-\alpha\lambda_m{}^2 t\right]. \tag{B.36}$$

Then the total solution is obtained by combination of Eqs. (B.34) and (B.36) into Eq. (A.28). For an explanation of the omission of $m < 0$, see Özişik [40].

$$T(x,t) = \sum_{m=0}^{\infty} c_m \cos(\lambda_m x) \exp\left[-\alpha\lambda_m{}^2 t\right]. \tag{B.37}$$

Application of the initial condition to Eq. (B.37) and the orthogonality property yields for the case of a split problem,

$$c_n = 2\left[\frac{\lambda_n{}^2 + H^2}{L\left(\lambda_n{}^2 + H^2\right) + H}\right]\int_0^L \left(T_o - T_{ss}\right)\cos\left(\lambda_m x'\right)dx'. \tag{B.38}$$

Combination with Eq. (B.24) for T_{ss} yields,

$$\int_0^L \left(T_o - T_{ss}\right)\cos\left(\lambda_m x'\right)dx' = \int_0^L \left(T_o - q''\left[\frac{\left(L - x\right)}{k} + \frac{1}{h}\right] - T_\infty\right)\cos\left(\lambda_m x'\right)dx', \tag{B.39}$$

which is directly integrable and yields Eq. (A.31),

$$\int_0^L \left(T_o - T_{ss}\right)\cos\left(\lambda_m x'\right)dx' = \frac{\sin\left(\lambda_m L\right)}{\lambda_m}\left(T_o - T_\infty - \frac{q''}{h}\right). \tag{B.40}$$

Finally, the total solution is obtained by combination of Eqs. (B.37), (B.38) and (B.40) which gives Eq. (A.32), which is identical to Eq. (4.3). The solution T(x,t) is reached by superposition of Eq. (A.32) with the steady state solution Eq. (A.33), as shown by Eq. (A.34).

$$T_h\left(x,t\right) = 2\sum_{m=1}^{\infty}\left[\frac{\lambda_m^2 + H^2}{L\left(\lambda_m^2 + H^2\right) + H}\right]\cdot\left[\frac{1}{\lambda_m}\right]\cos\left(\lambda_m x\right)\sin\left(\lambda_m L\right)\left(T_o - T_\infty - \frac{q''}{h}\right)e^{\left(-\alpha t\lambda_m^2\right)}, \tag{B.41}$$

$$T_{ss}\left(x\right) = q''\left[\frac{\left(L - x\right)}{k} + \frac{1}{h}\right] + T_\infty, \tag{B.42}$$

$$T\left(x,t\right) = T_h\left(x,t\right) + T_{ss}\left(x\right). \tag{B.43}$$

A.3 Derivation of Eqs. (4.7) to (4.9)

The solution method for the constant applied temperature problem is analogous to the solution for the applied heat flux problem. The same procedure is followed as for the derivation of Eqs. (4.2) to (4.5), but with the change of boundary conditions to those indicated by Eqs. (4.6). It is omitted here to avoid needless repetition. The interested reader may consult Özişik [40] for specifics of the solution not discussed above.

A.4 Derivation of Eq. (4.16)

Equation (A.35), along with the initial condition of Eq. (A.36) define the problem to be solved. Equation (A.35) is an inhomogeneous ordinary differential equation, which can be solved readily by the use of undetermined coefficients.

$$\frac{d\psi}{dt} + m\psi - p = 0, \tag{B.44}$$

$$\psi = \psi_o \quad \text{at} \quad t = 0. \tag{B.45}$$

The constants m and p are defined in physical terms as,

$$m = \frac{hA_2}{\rho V C_v}, \qquad p = \frac{A_1 q''(t)}{\rho V C_v}..$$

For the first case, the applied heat flux q″(t) is constant making the variable p is a constant. To solve the problem, it is assumed that the solution is made up of homogenous and particular parts,

$$\psi(t) = \psi_h(t) + \psi_p(t). \tag{B.46}$$

Then the homogenous problem is

$$\frac{d\psi_h}{dt} + m\psi_h = 0. \tag{B.47}$$

Equation (B.47) has an exponential solution,

$$\psi_h(t) = c_1 e^{-mt}. \tag{B.48}$$

The particular solution is obtained by assuming a functional form for ψ_p based on the type of boundary condition. In this case, the boundary condition (q″) is a constant, so ψ_p is chosen to be equal to the arbitrary constant K.

$$\psi_p(t) = K. \tag{B.49}$$

Equation (B.49) is then substituted into the ODE Eq. (B.44) so that the required form of K can be determined. Substitution gives,

$$0 + mK - p = 0,$$

which is solved for K to obtain,

$$K = \frac{p}{m}. \tag{B.50}$$

Then the particular solution is,

$$\psi_p(t) = \frac{p}{m}. \tag{B.51}$$

Combination of the homogenous and particular solution into Eq. (B.46) gives

$$\psi(t) = \frac{p}{m} + c_1 e^{-mt}. \tag{B.52}$$

The constant c_1 in Eq. (B.52) is determined by application of the initial condition, Eq. (B.45), which gives,

$$c_1 = \psi_o - \frac{p}{m}. \tag{B.53}$$

Thus, the full solution is given by Eq. (A.45). Substituting the definitions of p, m and q_r yields Eq. (A.46), which is identical to Eq. (4.16),

$$\psi(t) = \frac{p}{m} + \left(\psi_o - \frac{p}{m}\right) e^{-mt}, \tag{B.54}$$

$$\psi(t) = q_r + (\psi_o - q_r) \exp\left[-\frac{hA_2 t}{\rho V C_v}\right]. \tag{B.55}$$

A.5 Derivation of Eqs. (4.18) and (4.19)

The approach is identical to that which was used to obtain Eq. (B.55) up to the point of the particular solution. Previously, the particular solution was assumed to a constant to represent the constant applied heat flux. For heat flux that varies with time, the particular solution can be determined so that the term q″(t) may be represented by a desired curve fitted to experimental heat flux data. For the first case, a third order polynomial is used since it is versatile enough to capture much experimental behavior without being overly cumbersome in terms of manipulation. For simplicity, define the quantity Z as,

$$Z \equiv \frac{A_1}{\rho V C_v}. \tag{B.56}$$

Let the heat flux be represented by an arbitrary function q″(t) such that

$$q''(t) = e + ft + gt^2 + ht^3, \tag{B.57}$$

where e, f, g and g are experimentally determined coefficients required to model the heat flux as a function of time. Substitute Eq. (B.57) into the previously defined variable p,

$$p(t) = \frac{A_1 q''(t)}{\rho V C_v} = \frac{A_1}{\rho V C_v}\left(e + ft + gt^2 + ht^3\right) = Z\left(e + ft + gt^2 + ht^3\right). \tag{B.58}$$

which gives the functional form of p(t) and which can be inserted into the Eq. (B.44) to give Eq. (A.50).

$$\frac{d\psi}{dt} + m\psi - Z\left(e + ft + gt^2 + ht^3\right) = 0. \tag{B.59}$$

Since p(t) contains no ψ terms, the homogenous solution is obtained as before,

$$\psi_h(t) = c_1 e^{-mt}. \tag{B.60}$$

The particular solution is found by assuming a form equivalent to the form of the boundary condition. As the boundary condition is a third order polynomial for this case, the appropriate particular solution is,

$$\psi_p(t) = c_2 + c_3 t + c_4 t^2 + c_5 t^3. \tag{B.61}$$

The derivative is,

$$\frac{d\psi_p(t)}{dt} = c_3 + 2c_4 t + 3c_5 t^2. \tag{B.62}$$

The coefficients are obtained by solving the algebraic equation after substitution of Eqs. (B.61) and (B.62) into Eq. (B.59),

$$\left(c_3 + 2c_4 t + 3c_5 t^2\right) + m\left(c_2 + c_3 t + c_4 t^2 + c_5 t^3\right) - Z\left(e + ft + gt^2 + ht^3\right) = 0. \tag{B.63}$$

Equating coefficients for powers of t yields the simultaneous Eqs. (A.55),

$$\begin{aligned} &c_3 + mc_2 - Ze = 0, \\ &2c_4 + mc_3 - zf = 0, \\ &3c_5 + mc_4 - zg = 0, \\ &mc_5 - zh = 0, \end{aligned} \tag{B.64}$$

which are solved algebraically to obtain,

$$\begin{aligned} c_2 &= \frac{Z}{m}\left(e - \frac{f}{m} + \frac{2g}{m^2} - \frac{6h}{m^3}\right), \\ c_3 &= \frac{Z}{m}\left(f + \frac{2g}{m} - \frac{6h}{m^2}\right), \\ c_4 &= \frac{Z}{m}\left(g - \frac{3h}{m}\right), \\ c_5 &= \frac{Zh}{m}. \end{aligned} \tag{B.65}$$

By definition, $Z/m = A_1/hA_2$. Thus Eqs. (B.65) can be expressed,

$$
\begin{aligned}
c_2 &= \frac{A_1}{hA_2}\left(e - \frac{f}{m} + \frac{2g}{m^2} - \frac{6h}{m^3}\right),\\
c_3 &= \frac{A_1}{hA_2}\left(f + \frac{2g}{m} - \frac{6h}{m^2}\right),\\
c_4 &= \frac{A_1}{hA_2}\left(g - \frac{3h}{m}\right),\\
c_5 &= \frac{A_1}{A_2}.
\end{aligned}
\tag{B.66}
$$

The total solution is given by,

$$\psi(t) = c_1 e^{-mt} + c_2 + c_3 t + c_4 t^2 + c_5 t^3. \tag{B.67}$$

The remaining unknown constant c_1 is determined by application of the initial condition, which gives,

$$c_1 = \psi_o - c_2, \tag{B.68}$$

so that the final solution can be written as Eqs. (B.66) and (A.60). Upon substitution of m, Eq. (A.61) results. Equations (B.68) and (A.61) are identical to Eqs. (4.18) and (4.19).

$$\psi(t) = (\psi_o - c_2) e^{-mt} + c_2 + c_3 t + c_4 t^2 + c_5 t^3, \tag{B.69}$$

$$\psi(t) = (\psi_o - c_2) \exp\left[-\frac{hA_2 t}{\rho V C_v}\right] + c_2 + c_3 t + c_4 t^2 + c_5 t^3. \tag{B.70}$$

A.6 Derivation of Eq. (4.21)

For the second model of time varying heat flux, an exponential fit is used as an alternative to a polynomial. The reason for this is to give a simpler solution if the heat flux can be represented exponentially. As with the polynomial fit, the approach is identical up to the particular solution. In this case the heat flux is represented by the arbitrary exponential function,

$$q''(t) = ne^{rt}, \tag{B.71}$$

where n and r are the experimentally determined fitting constants. The quantity p(t) is found to be,

$$p(t) = \frac{A_1 q''(t)}{\rho V C_v} = \frac{A_1}{\rho V C_v}\left(ne^{rt}\right). \tag{B.72}$$

The appropriate particular solution is an exponential with the unknown constant c_2,

$$\psi_p(t) = c_2 e^{-rt}, \tag{B.73}$$

with the derivative,

$$\frac{d\psi_p(t)}{dt} = rc_2 e^{-rt}. \tag{B.74}$$

By substitution into Eq. (B.44), the algebraic equation,

$$rc_2 + mc_2 - Zn = 0, \tag{B.75}$$

is obtained, where Z is again defined by (B.56). Solving Eq. (B.75) for c_2 gives,

$$c_2 = \frac{Zn}{(r+m)}. \tag{B.76}$$

Combination with Eq. (B.73) gives the particular solution,

$$\psi_p(t) = \frac{Zn}{(r+m)} e^{-rt}. \tag{B.77}$$

The total solution is obtained by superposition of the particular and homogenous solutions, which yields,

$$\psi(t) = c_1 e^{-mt} \frac{Zn}{(r+m)} e^{-rt}. \tag{B.78}$$

Application of the initial condition gives,

$$c_1 = \psi_o - \frac{Zn}{(r+m)}. \tag{B.79}$$

The total solution for the exponential model, after substitution of Z, is Eq. (A.71), which is identical to Eq. (4.21),

$$\psi(t) = \left(\psi_o - \frac{A_1 n}{\rho V C_v (r+m)} \right) e^{-mt} + \frac{A_1 n}{\rho V C_v (r+m)} e^{rt}. \tag{B.80}$$

Appendix B

ANSYS model

The test facility was modeled using ANSYS Workbench© as a quarter sized piece as shown in Figure B1. A quarter sized model was used to take advantage of symmetry so that a refined mesh could be implemented. The simulation excludes contributions from the remaining chamber walls, as well as internal fans, but includes convective interior effects and losses to the ambient environment. Variation in thermal properties of the materials is considered, but radiation is neglected so that computing power can be focused on essential contributing factors.

The meshing scheme is shown in Figure B2. To facilitate good meshing, the model is constructed of rectangular shapes joined so that poorly shaped elements are avoided in most areas. The mesh near the test surface is highly refined to capture the important behavior. The total meshing size is approximately 510,000 nodes and 305,000 elements.

Conditions in the simulation are varied so that the steady state behavior can be observed for cases of applied heat flux and surface temperature, as well as for different types of connections between the test surface and chamber walls. The interior wall and test surface are exposed to a convective environment at 0 °C with a heat transfer coefficient of 8 W/m^2K. The rear wall surface is set to a fixed temperature of 18 °C according to experimental results where the actual temperature was monitored under similar conditions. The contact between the testing assembly and the wall is achieved both by determining where to make physical connections, and then estimating the contact resistance at those locations.

Typical results are illustrated by the contour plot in Figure B3 for an applied surface temperature of -18 °C at the rear surface of the heat spreader. Because the major source of heat flux in the simulation is due to the temperature difference between the spreader and the exterior chamber walls, the interaction between the two governs the resulting temperature and heat flux distributions. The results show that accurate modeling of the contact between the testing assembly and walls is difficult to achieve. Even slight variations in contact resistance change the results significantly, indicating that in order to use the ANSYS simulation reliably the contact model must be calibrated until results reflect experimental data accurately. Following such a calibration, changes in the chamber geometry could be made for new design analysis. That procedure is suggested as future work, since extensive comparison between the model and experimental results is required for reliability.

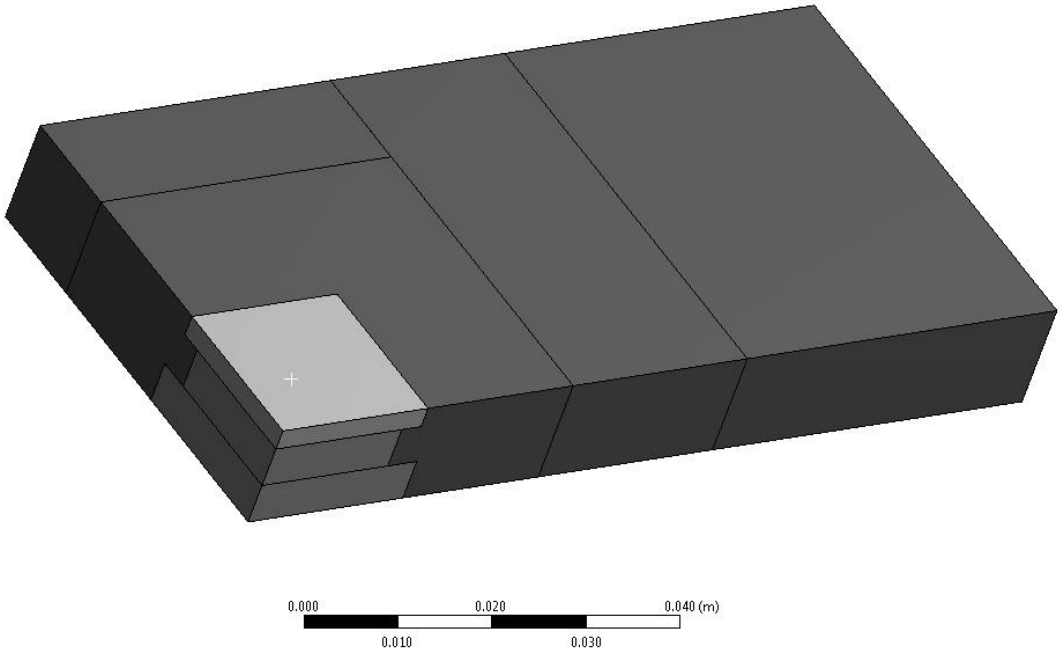

Figure B1. Geometry used for ANSYS simulation.

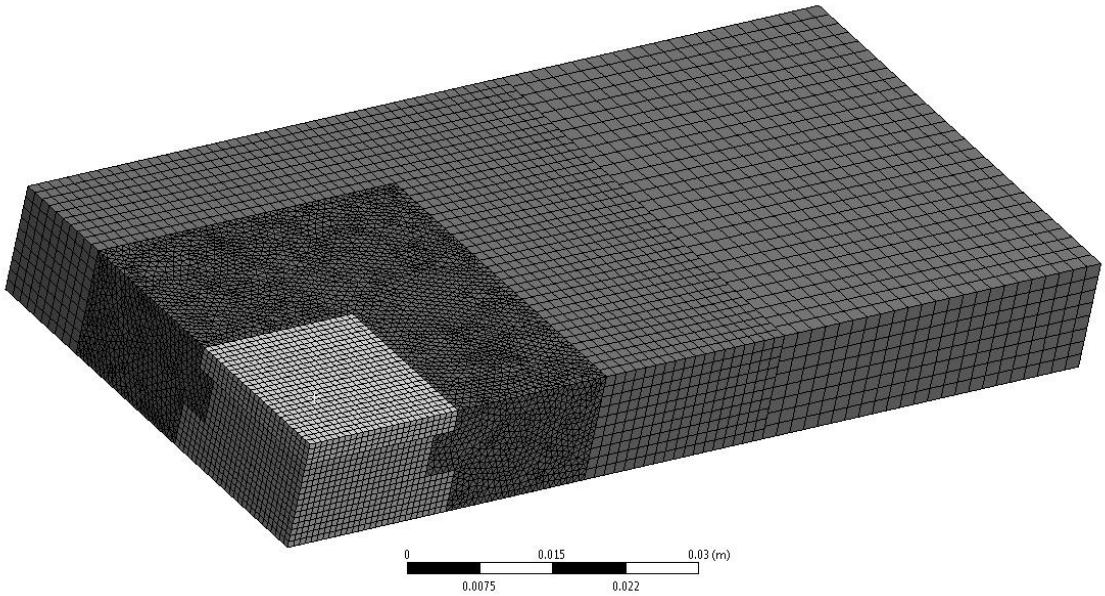

Figure B2. Meshing scheme for assembly.

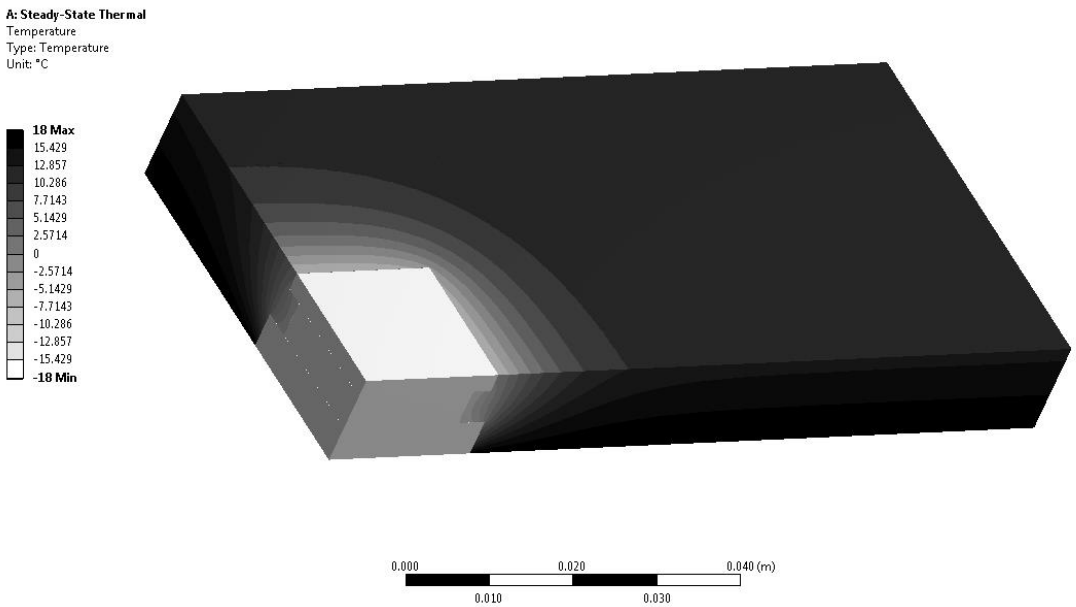

Figure B3. Results of simulation for an applied surface temperature of -18 °C.

Appendix C

Matlab Code/Simulation Information

C.1 Thickness Measurement

Part 1:

```
clear; clc;
%clf

%%% Input Properties %%%
cutoff = 865;                   % Test surface location (px)
multi = 135;                    % Multiplier for conversion to mm (135 pix/mm)
xmin = 5;                       % Lower edge cutoff location to avoid picture edges (px)
xmax = 1020;                    % Upper edge cutoff location to avoid picture edges (px)

%%% Adjustment parameters for boundary fitement %%%
cutoffdelt = 0;                         % Cutoff for picked up lower contours
thresh = 0.13;                          % Needed if graythresh(I) misses some peaks/valleys. Higher = more selective
csize = 0;                              % Closing criteria for contours [px]
usethresh = 1;                          % If 1, thresh used instead of graythresh(I)
usecut = 0;                             % If 1, specified area is clipped to help bounding

%%% Read in frost image %%%
I = imread('m1.bmp');             % Read in file


% For use on certain images
I = imadjust(I,[0.02 1],[]);
AT = graythresh(I);

if usecut == 1
FSI = zeros(1024,1280);
for i = 500 : 1280
    for k = 1 : 1024
        FSI(k,i) = I(k,i);
    end
end
FSI = uint8(FSI);
I = FSI;
end

if usethresh == 1
    BW = im2bw(I, thresh);
else
    BW = im2bw(I, AT);           % Convert to black/white
end

%%% Determine image size %%%
s = size(I);
pix = s(1)*s(2);                % Total pixel count

%%% Determine boundary location %%%
se = strel('disk',csize);
BW = imclose(BW,se);
[Ba,L] = bwboundaries(BW,'noholes');     % Locate boundaries
boundary = Ba{1};                        % Convert boundary location to matrix
[R C] = size(boundary);                 % Determine size of matrix for looping

%%% Loop to extract data points inside of specified max/min locations
%%% and cutoff line
p = 1;
cutoffdelt = cutoff - cutoffdelt;
for k = 1 : R
        if boundary(k,2) <= cutoffdelt && boundary(k,1) >= xmin && boundary(k,1) <= xmax
            f_line(p,1) = boundary(k,1);
            f_line(p,2) = boundary(k,2);
            p = p + 1;
        end
end
```

Part 2:

```
%%% Determine the layer thickness %%%
A = mean(f_line);                           % Find mean pixel height of extracted data
B = min(f_line);
C = max(f_line);
f_height = A(2);                            % Store only the heightwise average
f_hmax = B(2);
f_hmin = C(2);
deltapx = cutoff - f_height;                % Subtract from cutoff location (surface) to obtain thickness in px
dpx_max = cutoff - f_hmax;
dpx_min = cutoff - f_hmin;
delta = deltapx/multi;                      % Convert thickness from px to mm
deltamax = dpx_max/multi;
deltamin = dpx_min/multi;

fline_mm(:,1) = (xmax - f_line(:,1))/multi;     % Convert X locations from px to mm for plotting
fline_mm(:,2) = (cutoff - f_line(:,2))/multi;   % Convert Y locations from px to mm for plotting

imshow(transpose(I))
hold on
plot(f_line(:,1), f_line(:,2), 'rs', 'MarkerSize', 1,'MarkerFaceColor','k')
%axis([0 1024 1000 1280])
%%% Specify string label for plot %%%
AVT = sprintf('%s %1.2f %s','Average Thickness:', delta, 'mm');

%%% Plot the surface contour and the average pixel height %%%
%plot(fline_mm(:,1), fline_mm(:,2), 'ks', 'MarkerSize', 2,'MarkerFaceColor','k')     % In mm
%h = line([0 max(fline_mm(:,1))],[delta delta]);                                     % Average height
%text(0.2,-0.05,AVT,'BackGroundColor','w','EdgeColor','k');

%%% Styling properties for plot %%%
%set(h,'LineStyle','--','LineWidth',2);
%axis([0 max(fline_mm(:,1)) 0 max(fline_mm(:,2))+0.2]);
%xlabel('X - Location [mm]');
%ylabel('Frost Thickness [mm]');
%grid on

%%% Antia-aliasing for publishing %%%
%fh = figure(1);
%set(fh, 'color', 'white');
%myaa(8,'noshrink','publish');

%%% Display of Results %%%
fprintf('Image Size [px]: ')
fprintf('%1.0f %s %1.0f', s(2), 'x', s(1))
fprintf('\n')

fprintf('Total Size [px]: ')
fprintf('%1.0f', pix)
fprintf('\n')

fprintf('Frost Thickness [px]: ')
fprintf('%1.0f',deltapx)
fprintf('\n')

fprintf('Avg. Frost Thickness [mm]: ')
fprintf('%1.3f',delta)
fprintf('\n')

fprintf('Max Frost Thickness [mm]: ')
fprintf('%1.3f',deltamax)
fprintf('\n')

fprintf('Min Frost Thickness [mm]: ')
fprintf('%1.3f',deltamin)
fprintf('\n')

fprintf('Autothresh: ')
fprintf('%1.3f',AT)
fprintf('\n\n')
```

C.2 Frost Porosity

```
%Frost porosity analysis
%Routine to calculate frost porosity from frontal images.
%Converts image to black-white binary image, counts the number of
%ice-filled pixels, and divides by the total number of pixels.  Ice
%threshold level set up Matlab 'graythresh' routine.
%Bill Mohs and Dan Janssen, 2011

close all;
clear;
clc;

dens_ice = 920;
dens_air = 1.293;
da = 586.183;

AP = (da - dens_ice)/(dens_air - dens_ice);
%density = dens_ice*(1 - porosity) + porosity*(Rv+dens_air)

Tf = -10;
R = 461.5;

Pvap = @(T) 100*6.11*10.0^(7.5*T/(237.7+T));
Rv = Pvap(Tf)/(R*(Tf+273.15));

%%% Read in frost image %%%
frost = imread('ff.png');   %Read in
frost = rgb2gray(frost);        %Convert to grayscale
frost = imadjust(frost);
I = graythresh(frost);
%I = 0.355;
BW = im2bw(frost, I); %Convert to black and white image

%imshow(BW);

%%% Determine image size %%%
s = size(frost);
pix = s(1)*s(2); %Total pixel count

%%% Calculates porosity by summing the number of ice filled pixels
%%% and dividing by the total number of pixels.
porosity = 1- sum(sum(BW))/pix;
density = dens_ice*(1 - porosity) + porosity*(Rv+dens_air);
%end of program
```

C.3 Droplet Geometry (Single)

Part 1:

```
%close all;
clf;
clear ; clc;

% Individual drop data stored in array drop_dat

area = 0;                               % Area initialization
dc = 0;                                 % Data counter
Nbounds = 0;                            % Drop count initialization
sel = 70;                               % Selection criteria for boundary filtering [px]
csize = 90;                             % Closing criteria for contours [px]
se = strel('disk',csize);               % Closing method for contours

%%% Old code for base image generation %%%
%%% Needed for using a different photo set to configure the base
%%% calibration image

%{
Base = imread('base.png');                % Read in file
Base = rgb2gray(Base);                    % Grayscale conversion
Base = imadjust(Base);                    % Contrast correction
%}

%%% Read in frost images %%%
I = imread('image11082.png');           % Read in file
Base = imread('base_cal.png');          % Read in base calibration image

%%% Adjust image for use %%%
I = rgb2gray(I);                        % Grayscale conversion
I = imadjust(I);                        % Contrast correction
tsize = size(I,1)*size(I,2);            % Determine image size in px
I_corr = imsubtract(Base,I);            % Correct for background data
BW = im2bw(I_corr, graythresh(I));      % Conversion to black and white
BW = imclose(BW,se);                    % Attempt to close contours

%%% Determine boundary location %%%
[B,L] = bwboundaries(BW,'noholes');      % Locate boundaries
imdata = ones(size(BW));                 % Create array for image generation
pc = 0;
tp = 0;
hold on
```

Part 2:

```
for k = 1 : length(B)
           [M N] = size(B{k});
           ldrop = 0;

           if M >= sel
                dc = dc + 1;
                boundary = B{k};
                plot(boundary(:,2),boundary(:,1), 'k', 'LineWidth', 2)
                fill(boundary(:,2),boundary(:,1),'k');
                Nbounds = Nbounds + 1;
                adrop = trapz(boundary(:,1),boundary(:,2));     % Individual drop area
                area = area + adrop;                            % Moving total area

                cl = size(boundary,1);
                for z = 1 : cl - 1;
                    dx = boundary(z + 1,2) - boundary(z,2);
                    dy = boundary(z + 1,1) - boundary(z,1);
                    dl = sqrt(dx^2 + dy^2);
                    ldrop = ldrop + dl;
                    tp = tp + dl;
                end

                drop_dat(dc, 1) = dc;           % Drop Number
                drop_dat(dc, 2) = adrop;        % Drop Area [px^2]
                drop_dat(dc, 3) = adrop/tsize;  % Drop Area Frac
                drop_dat(dc, 4) = ldrop;        % Drop Perimeter
                drop_dat(dc, 5) = cl;           % Size of Matrix (N)

                % Generate image data matrix
                for i = 1 : M
                   x = boundary(i,1);
                   y = boundary(i,2);
                   imdata(x,y) = 0;
                end

           end

end
axis([0 size(I,2) 0 size(I,1)]);

area_ratio = area/tsize;            % Store total area ratio
avearea = area/Nbounds;             % Store average droplet area
averatio = avearea/tsize;           % Store average droplet area ratio (to total)
aveper = sum(drop_dat(:,4))/Nbounds;             % Store average droplet perimeter [px]

fprintf('Number of droplets: '); fprintf('%1.0f', Nbounds); fprintf('\n');
fprintf('Total area [px]: '); fprintf('%1.0f', area); fprintf('\n');
fprintf('Total Area ratio [%%]: '); fprintf('%1.3f', 100*area_ratio); fprintf('\n');
fprintf('Avg area ratio [%%]: '); fprintf('%1.3f', 100*averatio); fprintf('\n');
fprintf('Avg drop perimeter [px]: '); fprintf('%1.3f', aveper); fprintf('\n');
```

C.4 Droplet Geometry (Looped)

Part 1:

```
close all; clear ; clc;

% Individual drop data stored in array drop_dat
% Use cell array tdat to access the information for indivudal droplets on a
% specific image

imnum = 11002;                          % Numerical value of starting image filename
tims = 162;                             % Number of images
plotson = 1;                            % Show plots of averages

sel = 70;                               % Selection criteria for boundary filtering [px]
csize = 80;                             % Closing criteria for contours [px]
se = strel('disk',csize);               % Closing method for contours
tdat = cell(tims,1);                    % Initialize data storage
t = 0;                                  % Initialize time counter

%%% Old code for base image generation %%%
%%% Needed for using a different photo set to configure the base
%%% calibration image

%{
Base = imread('base.png');               % Read in file
Base = rgb2gray(Base);                   % Grayscale conversion
Base = imadjust(Base);                   % Contrast correction
%}

Base = imread('base_cal.png');          % Read in base calibration image
h = waitbar(0,'Calculating...');

for p = 1 : tims;
    clc
    area = 0;                             % Area initialization
    dc = 0;                               % Data counter
    Nbounds = 0;                          % Drop count initialization

    imtag = sprintf('%s%1.0f%s','image', imnum, '.png');
    pc = sprintf('%s%1.2f', 'Percent Complete: ', 100*p/tims);
    disp(pc)

    %%% Read in frost image %%%
    I = imread(imtag);               % Read in file

    %%% Adjust image for use %%%
    I = rgb2gray(I);                      % Grayscale conversion
    I = imadjust(I);                      % Contrast correction
    tsize = size(I,1)*size(I,2);          % Determine image size in px
    I_corr = imsubtract(Base,I);          % Correct for background data
    BW = im2bw(I_corr, graythresh(I));    % Conversion to black and white
    BW = imclose(BW,se);                  % Attempt to close contours

    %%% Determine boundary location %%%
    [B,L] = bwboundaries(BW,'noholes');     % Locate boundaries

    for k = 1:length(B)
          [M N] = size(B{k});
          ldrop = 0;
          if M >= sel
               dc = dc + 1;
               boundary = B{k};
               Nbounds = Nbounds + 1;
               adrop = trapz(boundary(:,1),boundary(:,2));      % Individual drop area
               area = area + adrop;                             % Moving total area
```

Part 2:

```
                cl = size(boundary,1);
                for z = 1 : cl - 1;
                    dx = boundary(z + 1,2) - boundary(z,2);
                    dy = boundary(z + 1,1) - boundary(z,1);
                    dl = sqrt(dx^2 + dy^2);
                    ldrop = ldrop + dl;
                end

                % Drop specific data
                drop_dat(dc, 1) = dc;           % Drop Number
                drop_dat(dc, 2) = adrop;        % Drop Area [px^2]
                drop_dat(dc, 3) = adrop/tsize;  % Drop Area Frac
                drop_dat(dc, 4) = ldrop;        % Drop Perimeter

            end
            tdat(p) = {drop_dat};
    end

    % Image specific data
    ddata(p, 1) = area;                         % Store total area [px]
    ddata(p, 2) = area/tsize;                   % Store total area ratio
    ddata(p, 6) = Nbounds;                      % Store number of droplets
    if Nbounds > 0;
        ddata(p, 3) = area/Nbounds;                 % Store average droplet area
        ddata(p, 4) = ddata(p,3)/tsize;           % Store average droplet area ratio (to total)
        ddata(p, 5) = sum(drop_dat(:,4))/Nbounds;               % Store average droplet perimeter [px]
    else
        ddata(p, 3) = 0;           % Store average droplet area
        ddata(p, 4) = 0;           % Store average droplet area ratio (to total)
        ddata(p, 5) = 0;           % Store average droplet perimeter [px]
    end

    if p >= 2
    if Nbounds > ddata(p-1,6)
        S = imtag;
    end
    end

    time(p) = t;                    % Time
    t = t + 2;
    imnum = imnum + 1;
    waitbar(p/tims,h)
end

if plotson == 1;
plot(time,ddata(:,2),'ok-','MarkerSize',2,'MarkerFaceColor','k');
xlabel('Time [s]');
ylabel('Covered area fraction');

figure;
plot(time,ddata(:,6),'ok-','MarkerSize',2,'MarkerFaceColor','k');
xlabel('Time [s]');
ylabel('Number of droplets');

figure;
plot(time,ddata(:,4),'ok-','MarkerSize',2,'MarkerFaceColor','k');
xlabel('Time [s]');
ylabel('Average drop area fraction');

figure;
plot(time,ddata(:,5),'ok-','MarkerSize',2,'MarkerFaceColor','k');
xlabel('Time [s]');
ylabel('Average drop perimeter');
end
```

Appendix D

Miscellaneous

D.1 Thermal conductivity correlation for air

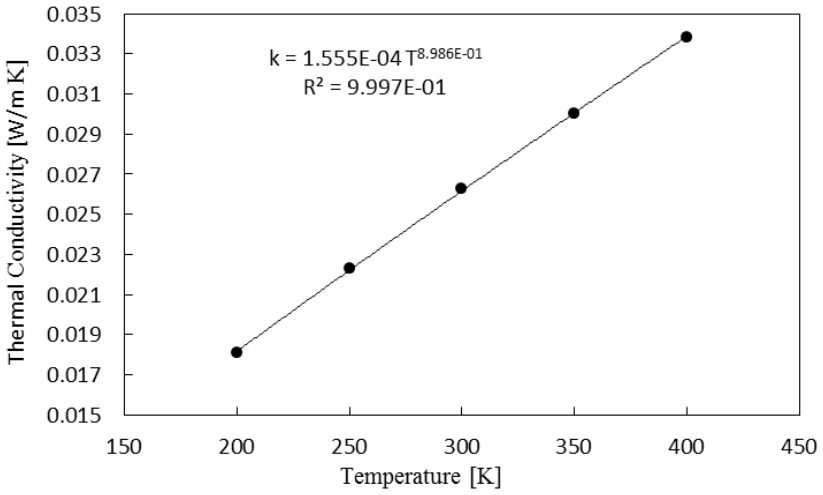

Figure 59. Data fit for thermal conductivity of air.

Data was fit for the thermal conductivity of air over the range of interest in terms of absolute temperature. A linear function can be used instead without any appreciable loss in accuracy. Figure 59 shows the accuracy of fit.

D.2 Heat flux losses from chamber

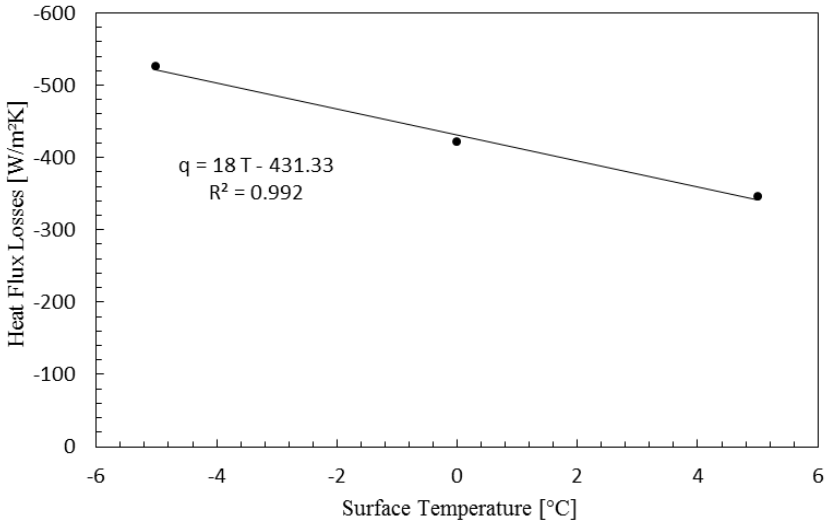

Figure 60. Heat flux losses through wall.

Figure 60 shows calibration for the heat flux losses obtained by measuring heat flux when the interior and test surface are equal. Measured heat flux in this case must equal the net change due to heat leakage.

D.3 Root mean square deviation

The root mean square deviation, or RMSD, is one form of error analysis which is commonly used for the comparison of predicted to actual values. The general form is given by Eq. (D.1), where N is the number of data points x_i. The actual and predicted values of x_i are denoted by superscripts a and p, respectively. The RMSD method is useful for computing the average error between two data sets, since it accounts for the variation at each point.

$$\mathrm{RMSD} = \sqrt{\frac{1}{N}\sum_{i=1}^{N}\left(x_i^{\,p} - x_i^{\,a}\right)}. \tag{B.81}$$